

PREDICTED AND MEASURED AERODYNAMIC CHARACTERISTICS
FOR TWO TYPES OF ATMOSPHERE-ENTRY VEHICLES

By Leland H. Jorgensen and Lawrence A. Graham

Ames Research Center
Moffett Field, Calif.

GROUP 4
Downgraded at 3 year intervals;
declassified after 12 years

CLASSIFIED DOCUMENT-TITLE UNCLASSIFIED

This material contains information affecting the national defense of the United States within the meaning of the espionage laws, Title 18, U.S.C., Secs. 793 and 794, the transmission or revelation of which in any manner to an unauthorized person is prohibited by law.

NOTICE

This document should not be returned after it has satisfied your requirements. It may be disposed of in accordance with your local security regulations or the appropriate provisions of the Industrial Security Manual for Safe-Guarding Classified Information.

NATIONAL AERONAUTICS AND SPACE ADMINISTRATION

~~CONFIDENTIAL~~

TABLE OF CONTENTS

	<u>Page</u>
SUMMARY	1
INTRODUCTION	2
NOTATION	3
Conversion from Units in This Report to SI Units (i.e., International System of Units).	6
EXPERIMENTAL APPARATUS, TEST METHODS, AND DATA REDUCTION	6
Test Facility	6
Determination of Stream Properties	7
Models, Balance, and Support	8
Tests	8
Reduction and Precision of Data	9
ANALYTICAL METHODS FOR CALCULATING AERODYNAMIC CHARACTERISTICS	10
Apollo-Type Vehicle	10
Modified Newtonian theory	10
Significance of stagnation-point pressure coefficient C_{pstag}	12
More refined methods for computing C_A for angles of attack of 0° and 180°	12
Computation of $C_{N\alpha}$ and $C_{m\alpha}$ for angles of attack of 0° and 180°	13
Polaris-Type Vehicle	14
General theoretical approach	14
Flare forces and pitching moments	14
Derivation of flare dynamic pressure	15
Estimation of body-alone contribution to $C_{N\alpha}$ and $C_{m\alpha}$	18
RESULTS AND DISCUSSION	21
Apollo-Type Vehicle	21
Modified Newtonian theory compared with experiment for angles of attack from 0° to 180°	21
Comparisons of theoretical and experimental values of C_A versus Mach number at angles of attack of 0° and 180°	22
Experimental afterbody pressures	23
Comparisons of theoretical with experimental values of $C_{N\alpha}$, $C_{m\alpha}$, and x_{cp}/d versus Mach number at $\alpha = 0^\circ$	23
Polaris-Type Vehicle	23
Theory compared with experiment for complete vehicle	24
Theory compared with experiment for flare alone and body alone	25
Theoretical stability as a function of speed and altitude	26
Effect of flow state on stability	27
CONCLUSIONS	27

	<u>Page</u>
APPENDIX - SAMPLE COMPUTATION OF DYNAMIC PRESSURE AT FLARE OF POLARIS- TYPE VEHICLE FOR EQUILIBRIUM FLOW	29
Wind Tunnel Case	29
Earth Atmosphere Flight Case	31
REFERENCES	34
FIGURES	37

~~CONFIDENTIAL~~

PREDICTED AND MEASURED AERODYNAMIC CHARACTERISTICS
FOR TWO TYPES OF ATMOSPHERE-ENTRY VEHICLES*

By Leland H. Jorgensen and Lawrence A. Graham
Ames Research Center

SUMMARY

Models representative of the Apollo and Polaris vehicles have been tested at Mach number 17 in the Ames arc-heated aerodynamic wind tunnel, and force and moment data from these tests and from previous tests in other facilities at lower Mach numbers have been compared with each other and with theoretical results. The angle-of-attack range covered for the Apollo-type vehicle was from 0° to 180° . For the Polaris-type vehicle the study was limited to angles of attack near 0° . A review is given in the report of some of the more tractable theoretical methods for computing the aerodynamic forces and moments, and, in some instances, new formulas are derived.

For the Apollo-type vehicle it is shown that the trends of the aerodynamic characteristics with angle of attack can be predicted reasonably well by modified Newtonian theory, although the magnitudes of the coefficients at angles of attack near 0° and 180° are not satisfactorily predicted. The primary trim angle of attack and lift-drag ratio are predicted closely by the theory and remain essentially fixed throughout the supersonic-hypersonic Mach number range. At 0° angle of attack (conical portion forward) the prediction of the axial-force coefficients can be noticeably improved by the combined use of modified Newtonian theory for the blunt vertex and sharp cone theory for the conical portion. At 180° angle of attack axial-force coefficients can be computed closely by the method of NASA TN D-1423. There is negligible contribution of afterbody pressure on total axial force at Mach numbers above about 5. There is, however, an effect of vehicle orientation on the measured afterbody pressures, the afterbody pressures being two to three times greater for the vehicle at 180° angle of attack than at 0° .

For the Polaris-type vehicle the present study demonstrates the inadequacy of Newtonian theory in estimating lift and static stability. Other simple theoretical methods are presented which predict the lift and stability reasonably well. It is shown, however, that the accuracy is enhanced primarily by the prediction of the flare contribution to the lift and stability. Further effort is required on the prediction of the cylindrical-body contribution. For very high flight speeds, theoretical calculations show that flare stability should increase if there is a change in the flow state near the body from equilibrium to frozen.

*Title, Unclassified.

~~CONFIDENTIAL~~

~~CONFIDENTIAL~~

INTRODUCTION

For the design and trajectory studies of blunt entry vehicles the aerodynamicist should know the aerodynamic force and moment characteristics throughout a wide range of Mach numbers. Often in the past there has been little or no experimental force and moment data upon which to draw, and theoretical estimates without experimental verification have been employed. This has been particularly true for hypersonic Mach numbers because of the scarcity of appropriate test facilities. To help provide force and moment data as well as other aerodynamic information for typical entry-type vehicles at hypersonic Mach numbers (and at desired angles of attack), the Ames arc-heated aerodynamic wind tunnel was recently brought into operation. Following initial calibration of the test stream, force and moment data were obtained at a Mach number of 17 for blunt-nosed models resembling the Apollo and Polaris vehicles. These configurations were selected primarily because the theoretical procedures which are verified for them can be readily applied to a variety of vehicle shapes. For example, Apollo-type models tested at angles of attack near 0° and 180° provide information for a slightly blunt large-angle cone with little afterbody as well as for a very blunt nose (spherical segment) with conical afterbody. Polaris-type models with and without flare provide information for a blunt nose with a short cylindrical aftersection, for a stabilizing flare in a body flow field, and, of course, for a complete nose-cylinder-flare configuration. Thus, to obtain information applicable to a variety of shapes, Apollo-type models were tested at angles of attack from 0° to 180° , and Polaris-type models, with and without afterbody flare, were tested at angles of attack from 0° to 12° .

In this report, data are presented from these tests at Mach number 17 and from previous tests in other facilities at lower hypersonic and supersonic Mach numbers. No attempt has been made to include all available data, but enough are included to demonstrate the primary effects of change in Mach number on the forces and pitching moments throughout the supersonic-hypersonic range.

In conjunction with the recent arc-tunnel tests at Mach number 17 a study has been made of some of the more tractable analytical methods for computing the forces and moments. Existing formulas have been reviewed, and, where necessary, additional formulas have been derived. As an aid in assessing the methods, computed forces and pitching moments have been compared with experimental results throughout the Mach number range from about 2 to 17.

The objectives of this report then are as follows: first, to present the recently obtained experimental results; second, to review pertinent details of the analytical study; and third, to discuss the comparisons of the computed with the experimental results. Because the experimental tests at Mach number 17 were the first to be conducted in the Ames arc-heated aerodynamic wind tunnel, the report also includes a brief description of the experimental apparatus, the results of the initial stream calibration, the test methods, and the data reduction procedures which were employed.

~~CONFIDENTIAL~~

NOTATION

A	nozzle cross-sectional area, ft ²
C _A	axial-force coefficient, $\frac{\text{axial force}}{q_{\infty}S}$
C _D	drag coefficient, $\frac{D}{q_{\infty}S}$
C _L	lift coefficient, $\frac{L}{q_{\infty}S}$
C _m	pitching-moment coefficient measured about the reference center shown in figure 6(a) or 6(b), $\frac{\text{pitching moment}}{q_{\infty}Sd}$ for Apollo-type vehicle and $\frac{\text{pitching moment}}{q_{\infty}S l}$ for Polaris-type vehicle
C _{mα}	initial slope of the curve of pitching-moment coefficient versus angle of attack, $\left(\frac{dC_m}{d\alpha}\right)_{\alpha=0}$, per radian
C _N	normal-force coefficient, $\frac{\text{normal force}}{q_{\infty}S}$
C _{Nα}	slope of the curve of normal-force coefficient versus angle of attack $\left(\frac{dC_N}{d\alpha}\right)_{\alpha=0}$, per radian
C _p	pressure coefficient, $\frac{p - p_{\infty}}{q_{\infty}}$
C _{p_{stag}}	stagnation-point pressure coefficient, $\frac{p_{t2} - p_{\infty}}{q_{\infty}}$
D	drag, lb
d	maximum face diameter of Apollo-type models and cylindrical diameter of Polaris-type models, in.
d'	maximum diameter of flared afterbody, in.
h	enthalpy, Btu/lb
L	lift, lb
l	model length, in.
l _e	distance from moment reference to transverse element measured along the body axis (see sketch (a)), in.
M	Mach number

~~CONFIDENTIAL~~

p	static pressure, atm
q	dynamic pressure, lb/ft ²
R	universal gas constant, 1545 ft-lb/mole °R
Re	Reynolds number based on d for Apollo-type models and on l for Polaris-type models
R _{eff}	effective nose radius of calorimeter, ft
r	radius, in.
S	reference area: maximum cross-sectional area of Apollo-type models and cylindrical cross-sectional area of Polaris-type models, in. ²
s	entropy, $\frac{\text{Btu}}{(\text{Initial mole of air})^{\circ\text{R}}}$
s'	distance from apex of the model to orifice, measured along body surface, in.
T	temperature, °K or °R as specified
u	speed, ft/sec
\dot{w}	weight flow, lb/sec
x _{cp}	center-of-pressure position from nose or shoulder as specified, in.
x _{Fl}	distance from moment reference to cylinder-flare juncture, in.
x _m	distance from nose-cylinder shoulder to moment reference, in.
x,y,z	distances in the Cartesian coordinate X,Y,Z direction, respectively, in.
Z	ratio of molecular weight of undissociated to dissociated gas
α	angle of attack, degrees or radians as specified
γ	isentropic exponent, $\left(\frac{\partial \ln p}{\partial \ln \rho}\right)_s$
Δ	angle between the body center line and the balance center line, deg
δ	angle between wind axis and the surface of a body element, deg
θ	angle between the body center line and the element surface, deg
ν	expansion angle, rad

~~CONFIDENTIAL~~

ρ	density, slugs/ft ³
ϕ	roll angle of surface element, referenced to Z axis, positive counterclockwise looking downstream, deg
ϕ_1	limiting value at which the surface element becomes parallel to the free-stream direction, deg
()*	sonic point

Subscripts

a	afterbody
B	body
b	base
c	cone or compression
cyl	cylinder
e	element or expansion
Fl	flare
N	nose
s	spherical segment
sh	shoulder
t	reservoir or total condition
trim	trim condition
w	wall condition
∞	free-stream condition
1	condition ahead of normal shock
2	condition behind normal shock

~~CONFIDENTIAL~~

Conversion From Units in This Report to SI Units
(i.e., International System of Units)

<u>Physical quantity</u>	<u>To convert from report units</u>	<u>Multiply by</u>	<u>To obtain SI units</u>
Altitude	ft	0.3048×10^{-3}	km
Area	ft ²	9.290×10^{-2}	m ²
Density	slugs/ft ³	5.154×10^2	kg/m ³
Dynamic pressure	lb/ft ²	47.88	N/m ²
Enthalpy	Btu/lb	2.324×10^3	J/kg
Force	lb	4.448	N
Heating rate	Btu/sec-ft ²	1.135	W/cm ²
Length	ft	.3048	m
	in.	2.540	cm
Pressure	atm	1	atm
Speed	ft/sec	.3048	m/sec
Weight-flow rate	lb/sec	.4536	kg/sec

EXPERIMENTAL APPARATUS, TEST METHODS, AND DATA REDUCTION

Test Facility

The tests at a nominal Mach number of 17 were conducted in the Ames arc-heated aerodynamic wind tunnel. This tunnel is one of several operating from a common vacuum system. Component parts of the tunnel which include the arc heater, nozzle, test chamber, and diffuser are identified in the photographs of figure 1. The arc heater (figs. 1(a) and (b)) is of the type described in reference 1, having concentric copper-ring electrodes and being water cooled. Running times of over a minute are maintained for typical tunnel reservoir conditions of 68 atmospheres pressure and 1000 Btu/lb enthalpy. A contoured throat section connects the arc heater unit to a conical nozzle of 8° half angle and 24-inch exit diameter. Various interchangeable throat sections can be used, depending upon the desired Mach number in the test section. For the present investigation a throat section of 0.218-inch diameter was employed to obtain a nominal Mach number of 17. Flow from the arc heater through the nozzle is discharged as a free jet for 24 inches in the test section and then is entrained by the diffuser (fig. 1(c)). A model support system in which the angle of pitch in the horizontal plane can be remotely controlled is used to vary the support angle of attack between the limits of $\pm 60^\circ$ (fig. 1(c)). A remotely controlled stream-survey apparatus that will move a rake (fig. 2(a)) to desired test positions is also available for use in the calibration of the test section.

In addition to the components shown in figure 1 the facility has supporting equipment consisting of a high pressure air supply, a five-stage steam ejector vacuum system, and a rectifier-type dc power supply. The air supply system provides 3000 psi air at the rate of 0.7 lb/sec. The vacuum system is capable of maintaining a pressure of about 100 microns of mercury in the plenum chamber for a flow of 0.3 pound of air per second. The power supply is rated at 15 megawatts.

Determination of Stream Properties

Properties of the test stream required for reduction and analysis of the model force and moment data included Mach number, total enthalpy, dynamic pressure, and Reynolds number. In order to determine these properties from tunnel-flow measurements the flow was assumed to be in equilibrium, and the charts of reference 2 were used. The effect of departure from equilibrium flow on the Mach number, dynamic pressure, and Reynolds number is discussed in a later section on Reduction and Precision of Data.

To determine the distribution of Mach number in the test section, pitot pressure p_{t2} was measured in the test section and total (stagnation) pressure p_{t1} and total enthalpy h_{t1} in the reservoir. Pitot pressures from a remotely controlled survey rake (fig. 2) were measured with commercially available strain-gage transducers. The total pressure p_{t1} in the reservoir was measured with a Bourdon tube gage, and the total enthalpy h_{t1} was determined by the "sonic-flow" method (see, e.g., ref. 2, 3, or 4) in which h_{t1} is given as a function of the measurable parameter $\dot{w}/p_{t1}A^*$. For this parameter the weight-flow rate \dot{w} was measured with a venturi meter, and A^* was taken as the area of the nozzle throat. Typical axial and radial distributions of measured p_{t2}/p_{t1} and the resulting values of Mach number determined from reference 2 are presented in figure 3. It can be seen (fig. 3(c)) that near the tunnel center line there was a small increase in Mach number in the axial direction from the nozzle exit to the survey-limit station 12 inches downstream. In the radial direction (fig. 3(d)) the gradients were also small near the tunnel center line where the noses of the models were positioned for all tests. As expected, the survey results showed the flow to be axially symmetric.

During the survey tests it was found that fairly large variations in total enthalpy from the desired value ($h_{t1} \approx 1000$ Btu/lb) had little or no effect on the p_{t2}/p_{t1} distributions (see fig. 4). The effect on Mach number, however, is noticeable (ref. 2), and for most of the testing the variation in total enthalpy was held to within about ± 100 Btu/lb to keep the Mach number deviation within ± 0.1 at a given stream position.

Because accurate values of total enthalpy are necessary for determining the stream properties from reference 2, the total enthalpy determined by the sonic-flow method was checked by an alternate method in which heat calorimeters are used in the test stream. For this method a simplified form of the Fay and Riddell heating-rate solution (ref. 5), as employed in references 3 and 6, was

~~CONFIDENTIAL~~

used. For conditions corresponding to a Prandtl number of 0.72 and a Lewis number of 1, the total enthalpy in Btu/lb was determined from the simple relation,

$$h_{t_1} = \frac{\dot{q}}{0.042} \sqrt{\frac{R_{eff}}{p_{t_2}}} + h_w$$

where \dot{q} is the measured heating rate from the calorimeter in Btu/sec-ft²; p_{t_2} is the pitot pressure in atmospheres; R_{eff} is the effective calorimeter nose radius of curvature in feet; and h_w is the ambient wall enthalpy in Btu/lb. For the present investigation calorimeters of the type shown in figure 2 were positioned on the survey rake at radial intervals of 2 inches, and the radial heating-rate distribution was measured at axial stations of 2 and 12 inches downstream from the nozzle exit. The value of R_{eff} (equal to 0.0788 foot for the calorimeters used) was determined from reference 7, and h_w (equal to about 130 Btu/lb) was determined from reference 8. From the surveys it was found that the radial heating-rate distributions were almost constant over a flow diameter of at least 12 inches (see fig. 5). The resulting average value of h_{t_1} (about 980 Btu/lb) was only slightly less (within about 50 Btu/lb) than the value determined by the sonic-flow method. In addition, the calorimeter surveys indicated that there was only a small loss in h_{t_1} (about 30 Btu/lb) from the station at 2 inches from the nozzle exit to the one at 12 inches.

Models, Balance, and Support

The models tested resembled the Apollo capsule and an early version of the Polaris entry stage (see figs. 6(a) and (b)). For convenience of identification, they were referred to as the Apollo-type and Polaris-type models. Apollo-type models with face diameters of 2.25 and 5 inches were tested. Polaris-type models with a cylindrical diameter of 2.5 inches were tested with and without the stabilizing flare.

All models were mounted on a six-component balance (fig. 6(c)) which was attached to the variable angle-of-attack sting support. The angle of attack of the sting support was remotely controlled and, as previously stated, could be varied within the maximum limits of $\pm 60^\circ$ during a run. However, in order to reduce the effects of sting interference, the Apollo-type models were mounted on the balance at several offset attitudes (see figs. 6(d) and (e)) so that sting angles of attack no greater than $\pm 30^\circ$ were used over most of the model α range from 0° to 180° . The Polaris-type models were mounted only from the base with the bodies aligned with the sting support (see lower half of fig. 6(b)).

Tests

Balance measurements of normal force, axial force, and pitching moment were made for all models at a free-stream Mach number of about 17.2. This Mach number was determined from the stream surveys previously discussed and

~~CONFIDENTIAL~~

existed at the forward location of the models (on the tunnel center line about 11 inches from the nozzle exit). All models were positioned on the support mechanism so that the forward portion of each model remained at about the same tunnel location for all runs and for each angle of attack. The Apollo-type models were tested at angles of attack from 0° to 180° , and the Polaris-type models were tested at angles of attack from 0° to about 12° . For all runs the free-stream total pressure p_{t_1} was about 68 atmospheres, and the total enthalpy h_{t_1} was about 1000 Btu/lb. For these conditions the free-stream Reynolds number, determined from reference 2, was about 6.3×10^3 per inch. The resulting Reynolds numbers based on face diameter for the Apollo-type models and on length for the Polaris-type model were as follows:

<u>Model type</u>	<u>Size, in.</u>	<u>$Re \times 10^{-6}$</u>
Apollo	$d = 2.25$	0.014
Apollo	$d = 5.00$.032
Polaris	$l = 7.78$.049

Afterbody pressure was measured in the region of the sting-body juncture over the complete angle-of-attack range. The location of the pressure orifice in relation to the model and support is shown in figure 6(f) for the 5-inch-diameter Apollo-type model at $\alpha = 180^\circ$. Pressure was measured with a commercially available pressure transducer. Limited pressure tests were also made with the 2.25-inch-diameter model oriented at $\alpha = 180^\circ$ and mounted upstream in the conical nozzle at a Mach number of 14.2 and at a Reynolds number of about 0.023×10^6 .

Reduction and Precision of Data

All of the force and moment data have been reduced to coefficient form and are referred to both the body and wind axes systems (see fig. 7). Pitching-moment coefficients were taken about the model reference centers shown in figures 6(a) and (b). All coefficients for the Apollo-type models are based on the maximum (face) cross-sectional area, and the corresponding diameter is taken as the reference length for the moment coefficients. Coefficients for the Polaris-type models are based on the cross-sectional area of the cylindrical section, and the model length ($l = 7.78$ in.) is taken as the reference length for the moment coefficients.

In the reduction of the data to coefficient form, it is particularly important that the correct value of free-stream dynamic pressure q_∞ be used. Since equilibrium nozzle flow was assumed in this investigation, the question arises as to whether q_∞ would be changed significantly for a tunnel flow that has departed appreciably from equilibrium. Yalamanchili in reference 9 indicates that, for conditions similar to those of this investigation, the flow will "freeze" rapidly downstream of the nozzle throat at about an area ratio of $A/A^* = 2$ (or $M_\infty \approx 2$). For the assumption of equilibrium flow to $M_\infty = 2$ and then flow with frozen chemical reactions and frozen molecular vibrations downstream, the authors of the present report calculated a test Mach number of about 18.0 as compared to the equilibrium value of 17.2, but

~~CONFIDENTIAL~~

~~CONFIDENTIAL~~

there was negligible change in the computed dynamic pressure q_∞ . In view of the insignificant effect on q_∞ it is felt that any uncertainty in Mach number as a result of nonequilibrium flow may be of minor importance. There was also negligible change in the computed Reynolds number as a result of the frozen flow assumption.

The precision of the final data is affected by uncertainties in the measurement of the forces and moments, and in the determination of the dynamic pressure used in reducing the forces and moments to coefficient form. These individual uncertainties result in estimated over-all uncertainties as follows:

$$\begin{aligned} \alpha &\pm 0.1^\circ \\ C_N &\pm 0.03 & C_L &\pm 0.02 \\ C_A &\pm 0.03 & C_D &\pm 0.04 \\ C_m &\pm 0.005 \text{ (Apollo-type model)} \\ C_m &\pm 0.003 \text{ (Polaris-type model)} \end{aligned}$$

Any effects of possible sting-support interference and base pressure on the models have been neglected in reducing the data and estimating the precision.

Several repeat runs were made for each set of test conditions, and the data presented herein represent the arithmetic average of measured coefficients from the various runs. Generally the repeatability of the measurements was well within the estimated precision.

ANALYTICAL METHODS FOR CALCULATING AERODYNAMIC CHARACTERISTICS

In this section of the report some tractable methods are reviewed for computing the aerodynamic forces and pitching moments of entry vehicles of the Apollo and Polaris types. New formulas are derived in several instances. For clarity and convenience the Apollo- and Polaris-type vehicles are considered separately.

Apollo-Type Vehicle

Modified Newtonian theory.— For a blunt capsule of the Apollo type, the aerodynamic forces and moments are most easily computed if the Newtonian, or more accurate modified Newtonian, method is assumed. In the present investigation the modified Newtonian method was adopted, with the local pressure coefficient given by

$$C_p = C_{pstag} \sin^2 \delta \quad (1)$$

where δ is the angle between a local surface element and the wind axis, and

$$C_{pstag} \equiv \frac{p_{t2} - p_\infty}{q_\infty}$$

General expressions for the force and moment coefficients (referenced to the body axis) can be written as (e.g., ref. 10)

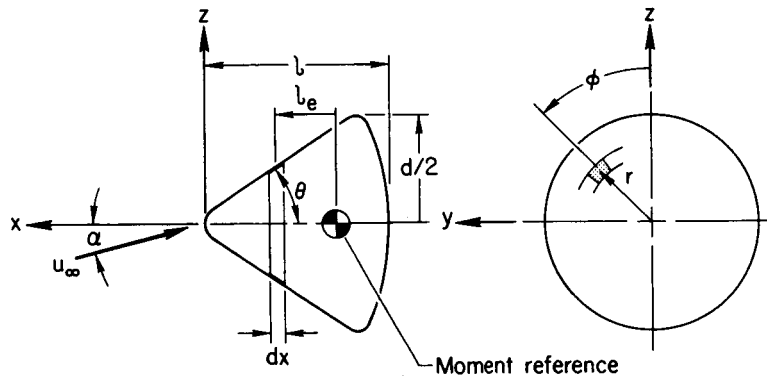
$$C_N = \frac{8l}{\pi d^2} \int_0^1 \int_{\varphi_1}^{\pi} C_p(-\cos \varphi) r \, d\varphi \, d\left(\frac{x}{l}\right) \quad (2)$$

$$C_A = \frac{8l}{\pi d^2} \int_0^1 \int_{\varphi_1}^{\pi} C_p(-\tan \theta) r \, d\varphi \, d\left(\frac{x}{l}\right) \quad (3)$$

and

$$C_m = \frac{8l^2}{\pi d^3} \int_0^1 \int_{\varphi_1}^{\pi} C_p(-\cos \varphi) r \frac{l_e}{l} \, d\varphi \, d\left(\frac{x}{l}\right) \quad (4)$$

where the diameter d is taken as the reference length in C_m . The angle φ is the roll angle of the surface element as illustrated in sketch (a), and φ_1 is the limiting value of φ at which the surface element becomes parallel to the free-stream direction.



Sketch (a)

For no angle of sideslip (as was the case for this investigation)

$$\varphi_1 = \cos^{-1} \frac{\tan \theta}{\tan \alpha} \quad (5)$$

and $\sin^2 \delta$ in equation (1) is given by

$$\sin^2 \delta = (\sin \theta \cos \alpha - \cos \theta \cos \varphi \sin \alpha)^2 \quad (6)$$

~~CONFIDENTIAL~~

For the present investigation, values of C_N , C_A , and C_m were computed for α from 0° to 180° . Then these results were used for computing values of C_L and C_D referred to the wind axis (see fig. 7).

Significance of stagnation-point pressure coefficient C_{pstag} . It is obvious from equations (2), (3), and (4) that the force and moment coefficients vary directly with vehicle geometry and with C_{pstag} which, in turn, is determined from free-stream conditions. Computed aerodynamic coefficients for a particular free-stream condition can be quickly modified to apply to another condition by merely multiplying the coefficients by the ratio of the new C_{pstag} to the old C_{pstag} .

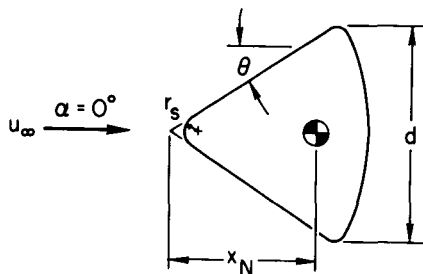
A useful approximation for C_{pstag} in terms of normal-shock density ratio is

$$C_{pstag} = 2 - \frac{\rho_\infty}{\rho_2} \quad (7)$$

This relation, which is very accurate at high Mach numbers, was derived by combining the one-dimensional mass and continuity equations with the Bernoulli equation for incompressible flow. Equation (7) is convenient to use because of the availability of charts of ρ_2/ρ_∞ as a function of free-stream velocity and altitude (e.g., refs. 11, 12, and 13) or as a function of Mach number M_∞ and total enthalpy h_t in a wind tunnel (e.g., ref. 2).

More refined methods for computing C_A for angles of attack of 0° and 180° . For shapes of the Apollo type at angles of attack of 0° and 180° , methods more accurate than the modified Newtonian method are available for use in calculating the axial-force coefficients. At $\alpha = 0^\circ$ (sketch (b)) exact inviscid sharp cone theory can be applied for the conical portion of the forebody along with modified Newtonian theory for the spherical tip. The axial-force coefficient, exclusive of base pressure drag, is expressed by (e.g., ref. 14)

$$(C_A)_{\alpha=0} = \left(\frac{2r_s}{d}\right)^2 C_{A_s} + \left[1 - \left(\frac{2r_s \cos \theta}{d}\right)^2\right] C_{A_c} \quad (8)$$



Sketch (b)

where the contribution of the blunt spherical segment is given by

$$C_{A_s} = \frac{1}{2} C_{pstag} (1 - \sin^4 \theta) \quad (9)$$

In equation (8) C_{A_c} is the axial-force coefficient for a cone of half-angle θ . Cone theory values of C_{A_c} as a function of θ and M_∞ can be obtained from chart 6 in reference 15.

~~CONFIDENTIAL~~

At $\alpha = 180^\circ$ (blunt face forward) the flow-continuity method of reference 16 can be used to compute the blunt-face pressures and hence the axial-force coefficient. This method is expected to be inherently more accurate than Newtonian theory for this shape because it accounts for the effect of the front-face sonic ring on the pressure distribution. Newtonian theory, of course, fails to account for the effect of this ring and overestimates the pressures near the outer edges of blunt bodies. Thus the axial force is overestimated, and for more precise calculations another method such as that of reference 16 is required.

Computation of $C_{N\alpha}$ and $C_{m\alpha}$ for angles of attack of 0° and 180° . For shapes of the Apollo-type at angles of attack of 0° and 180° $C_{N\alpha}$ and $C_{m\alpha}$ can be computed by the modified Newtonian theory previously discussed. At $\alpha = 0^\circ$ (conical portion forward), however, the alternate method suggested for computing C_A also can be applied. In this method exact inviscid cone theory is used for the conical portion of the body along with modified Newtonian theory for the spherical tip. From reference 14 and for the notation in sketch (b), we write

$$\left(C_{N\alpha}\right)_{\alpha=0} = \left(\frac{2r_s}{d}\right)^2 C_{N\alpha,s} + \left[1 - \left(\frac{2r_s \cos \theta}{d}\right)^2\right] C_{N\alpha,c} \quad (10)$$

$$\begin{aligned} \left(C_{m\alpha}\right)_{\alpha=0} = & -\frac{1}{2 \sin \delta_N} \left(\frac{2r_s}{d}\right)^3 C_{N\alpha,s} - \frac{2}{3 \sin 2\theta} \left[1 - \left(\frac{2r_s \cos \theta}{d}\right)^3\right] C_{N\alpha,c} \\ & + \frac{x_N}{d} \left(C_{N\alpha}\right)_{\alpha=0} \end{aligned} \quad (11)$$

where the contribution of the blunt spherical segment at $\alpha = 0^\circ$ is given by

$$C_{N\alpha,s} = \frac{1}{2} C_{pstag} \cos^4 \theta \quad (12)$$

In equations (10) and (11) $C_{N\alpha,c}$ is for a cone of half-angle θ at free-stream Mach number M_∞ . Values of $C_{N\alpha,c}$ by inviscid cone theory can be read from chart 8 in reference 15. Obviously, these equations also can be used with values of $C_{N\alpha,c}$ obtained from the modified Newtonian expression,

$$C_{N\alpha,c} = C_{pstag} \cos^2 \theta \quad (13)$$

Gary T. Chapman of Ames Research Center has observed that from modified Newtonian theory,

~~CONFIDENTIAL~~

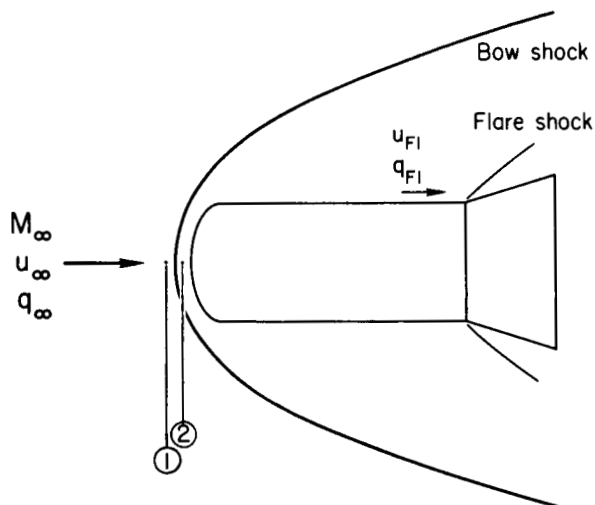
$$(C_{N\alpha})_{\alpha=0} + (C_A)_{\alpha=0} = C_{pstag} \quad (14)$$

Equation (14) is applicable for $C_{N\alpha}$ and C_A at $\alpha = 180^\circ$ as well as at $\alpha = 0^\circ$.

All of the relations given can be used for Newtonian theory by letting C_{pstag} equal 2. For sharp cones, values of $(C_{N\alpha})_{\alpha=0}$ and $(C_A)_{\alpha=0}$ from Newtonian theory agree closer with exact inviscid cone theory than do values from modified Newtonian theory.

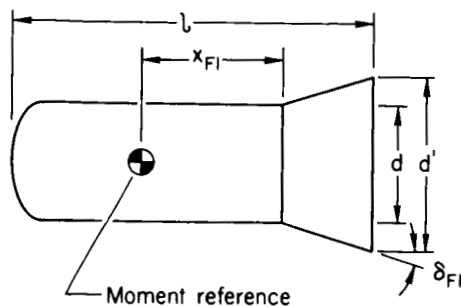
Polaris-Type Vehicle

General theoretical approach.— For a Polaris-type vehicle, such as that in sketch (c), the aerodynamic characteristics are taken as the sum of the characteristics for the composite parts - nose, flare, and connecting cylinder.



Sketch (c)

As for the Apollo-type capsule, modified Newtonian theory can be used to estimate the characteristics for the blunt nose (see previous discussion). For the flared aftersection cone theory or Newtonian theory may be applied, but, as first pointed out by Seiff (ref. 17), the coefficients must be corrected for the loss in dynamic pressure from the free-stream to the flare condition. The effectiveness of the flare in stabilizing a vehicle of this type is of prime importance, especially near the normal flight attitude of zero angle of attack. In the following paragraphs a method for calculating the flare effectiveness and flare drag near zero angle of attack is reviewed. Then at the end of this section of the report an approximate method for estimating the lift and stability contribution of the cylindrical portion of the body is reviewed. Inviscid flow is assumed throughout the study.



Sketch (d)

Flare forces and pitching moments.—

For a conical flare aftersection (sketch (d)) it was shown in reference 14 that

$$C_{N\alpha, Fl} = \frac{q_{Fl}}{q_\infty} \left[\left(\frac{d'}{d} \right)^2 - 1 \right] C_{N\alpha, c} \quad (15)$$

$$C_{D_{Fl}} = \frac{q_{Fl}}{q_{\infty}} \left[\left(\frac{d'}{d} \right)^2 - 1 \right] C_{D_c} \quad (16)$$

and

$$C_{m_{\alpha, Fl}} = \frac{\frac{q_{Fl}}{q_{\infty}}}{2 \frac{l}{d} \tan \delta_{Fl}} \left\{ \left[\left(\frac{d'}{d} \right)^2 - 1 \right] - \frac{2 \left[\left(\frac{d'}{d} \right)^3 - 1 \right]}{3 \cos^2 \delta_{Fl}} \right\} C_{N_{\alpha, c}} - \frac{x_{Fl}}{l} C_{N_{\alpha, Fl}} \quad (17)$$

where $C_{N_{\alpha, c}}$ and C_{D_c} are the coefficients for the cone of diameter d' and half-angle δ_{Fl} . Values of $C_{N_{\alpha, c}}$ and C_{D_c} from cone theory or from modified Newtonian theory can be used. It should be noted that the reference length for the moment coefficient in equation (17) is the over-all vehicle length, l . In reference 18 a second-order shock expansion method was used to obtain the flare pressure distribution and drag.

Various approaches can be employed in estimating the dynamic pressure q_{Fl} in front of the body flare for the assumption of attached flow. In one method, for example, the continuity equation is used in conjunction with the oblique shock relations (through the bow shock) and an assumed blast-wave-type pressure distribution in the flow field between the body surface and the bow shock (refs. 17 and 19). A weighted average value of dynamic pressure in front of the flare shock is used for q_{Fl} . The main difficulty with this method is that the bow shock shape and position must be known. A simpler and more direct approach is to consider only the pressure on the body surface. Ideal gas relations are used in conjunction with a blast-wave-type pressure relation on the body at the body-flare junction. (Justification for this approach is discussed later in the report.) In this method the dynamic pressure at the flare root is assumed constant over the flare. Since for a blunt body the dynamic pressure in front of the flare shock probably increases slightly from the flare-cylinder junction to the radial position in front of the flare base, this simple approach can be expected to give an average value of q_{Fl} that is lower than that which exists. The derivation of an equation for the dynamic pressure by this simple approach is presented next.

Derivation of flare dynamic pressure.— An expression for the ratio of the local to the free-stream dynamic pressure, q_{Fl}/q_{∞} , as a function of Mach number, M_{∞} , and pressure ratio, p_{Fl}/p_{∞} , is desired (see sketch (c)). We first write the thermal state and conservation of energy equations as

$$p = \rho RT \quad [\text{thermal state}] \quad (18)$$

and

$$\frac{1}{2} u_{Fl}^2 + h_{Fl} = \frac{1}{2} u_{\infty}^2 + h_{\infty} \quad [\text{energy conservation}] \quad (19)$$

For an ideal gas (constant specific heats),

$$h_{F1} = C_p T_{F1} \quad (20)$$

and

$$h_{\infty} = C_p T_{\infty}$$

By substituting equations (18) and (20) into (19), obtain

$$\frac{1}{2} u_{F1}^2 + \frac{\gamma}{\gamma - 1} \frac{p_{F1}}{\rho_{F1}} = \frac{1}{2} u_{\infty}^2 + \frac{\gamma}{\gamma - 1} \frac{p_{\infty}}{\rho_{\infty}} \quad (21)$$

By definition,

$$q_{F1} \equiv \frac{1}{2} \rho_{F1} u_{F1}^2$$

and

$$q_{\infty} \equiv \frac{1}{2} \rho_{\infty} u_{\infty}^2 = \frac{\gamma}{2} p_{\infty} M_{\infty}^2$$

(22)

Hence, equations (22) can be rewritten to give

$$\frac{q_{F1}}{q_{\infty}} = \frac{\rho_{F1}}{\rho_{\infty}} \left[1 + \frac{2}{(\gamma - 1) M_{\infty}^2} \right] - \frac{2}{(\gamma - 1) M_{\infty}^2} \left(\frac{p_{F1}}{p_{\infty}} \right) \quad (23)$$

In order to apply equation (23) there is derived an expression for ρ_{F1}/ρ_{∞} in terms of M_{∞} and p_{F1}/p_{∞} . For isentropic flow,

$$\frac{p_{F1}}{p_{t2}} = \left(\frac{\rho_{F1}}{\rho_{t2}} \right)^{\gamma} \quad (24)$$

and

$$\frac{p_{\infty}}{p_{t1}} = \left(\frac{\rho_{\infty}}{\rho_{t1}} \right)^{\gamma}$$

For constant total temperature ($T_{t2} = T_{t1}$),

$$\frac{p_{t2}}{p_{t1}} = \frac{\rho_{t2}}{\rho_{t1}} \quad (25)$$

Equations (24) and (25) are combined to give

$$\frac{\rho_{FL}}{\rho_{\infty}} = \left(\frac{p_{t2}}{p_{t1}} \right)^{\frac{\gamma-1}{\gamma}} \left(\frac{p_{FL}}{p_{\infty}} \right)^{\frac{1}{\gamma}} \quad (26)$$

For a perfect gas the total pressure ratio across a normal shock is given by (e.g., ref. 15)

$$\frac{p_{t2}}{p_{t1}} = \left[\frac{(\gamma + 1)M_{\infty}^2}{(\gamma - 1)M_{\infty}^2 + 2} \right]^{\frac{\gamma}{\gamma-1}} \left[\frac{\gamma + 1}{2\gamma M_{\infty}^2 - (\gamma - 1)} \right]^{\frac{1}{\gamma-1}} \quad (27)$$

Then the expression for ρ_{FL}/ρ_{∞} , obtained by combining equations (26) and (27), is

$$\frac{\rho_{FL}}{\rho_{\infty}} = \left[\frac{(\gamma + 1)M_{\infty}^2}{(\gamma - 1)M_{\infty}^2 + 2} \right] \left[\frac{\left(\frac{p_{FL}}{p_{\infty}} \right)}{1 + \frac{2\gamma}{\gamma + 1} (M_{\infty}^2 - 1)} \right]^{\frac{1}{\gamma}} \quad (28)$$

The desired dynamic pressure relation, obtained by substituting equation (28) into equation (23), is

$$\frac{q_{FL}}{q_{\infty}} = \left(\frac{\gamma + 1}{\gamma - 1} \right) \left[\frac{\left(\frac{p_{FL}}{p_{\infty}} \right)}{1 + \frac{2\gamma}{\gamma + 1} (M_{\infty}^2 - 1)} \right]^{\frac{1}{\gamma}} - \frac{2}{(\gamma - 1)M_{\infty}^2} \left(\frac{p_{FL}}{p_{\infty}} \right) \quad (29)$$

For use with equation (29) a convenient relation for p_{FL}/p_{∞} can be determined from consideration of blast-wave theory. From the blast-wave analogy, Kuehn (ref. 20) accurately correlated theoretical and experimental pressures on blunt-nosed cylinders and from this correlation obtained the expression,

$$\frac{p}{p_{\infty}} = 0.85 \left[\frac{f(\gamma)M_{\infty}^2 C_{DN}^{1/2}}{\frac{x}{d}} \right] + 0.55 \quad (30)$$

where x is measured from the nose, and values of $f(\gamma)$ as a function of γ are listed as follows:

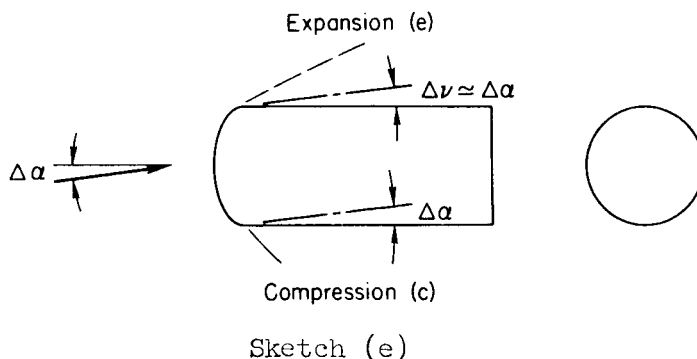
~~CONFIDENTIAL~~

γ	$f(\gamma)^1$
1.2	0.052
1.3	.061
1.4	.067
1.67	.084

With x taken at the cylinder-flare juncture, $p = p_{F1}$, and equation (30) can be used with equation (29) to compute q_{F1}/q_∞ for attached flow.

In addition to the method just given, q_{F1}/q_∞ can be readily computed for the assumption of equilibrium flow around the body to the flare. For this approach equilibrium-flow charts (e.g., refs. 2, 11, 21, and 22) instead of ideal gas relations are used with equation (30). The procedure is demonstrated with sample calculations given in the appendix for a wind-tunnel case and for a flight case in the earth's atmosphere.

Estimation of body-alone contribution to $C_{N\alpha}$ and $C_{m\alpha}$. Along with the nose and flare contribution to the lift and stability of the vehicle, there can be a significant contribution from the cylindrical portion of the body (see, e.g., refs. 14 and 23). Although $C_{N\alpha, cyl}$ at $\alpha = 0^\circ$ is zero by both slender-body theory and Newtonian theory, experiment has indicated that the normal force developed by the cylinder even near zero incidence cannot be ignored. Seiff (ref. 23) has made the suggestion that the contribution of the cylinder can be estimated by letting the pressure perturbation due to angle of attack be given by a linearized Prandtl-Meyer equation applied to the zero angle-of-attack pressure distribution. In line with this approach to the problem, the derivation of approximate expressions for estimating $C_{N\alpha, cyl}$ and $C_{m\alpha, cyl}$ is presented next.



The pressure near the shoulder on the compression side of the cylinder (sketch (e)) is assumed to be given by a linearized oblique-shock relation for weak shocks, whereas, the pressure on the expansion side is given by a linearized Prandtl-Meyer expression. From equations (151) and (174) of reference 15, we write

¹From a logarithmic plot of these values it can be shown that $f(\gamma) = 0.098(\gamma - 1)^{0.395}$.

$$\frac{p_c}{p_{sh}} = 1 + \frac{\gamma M_{sh}^2}{\sqrt{M_{sh}^2 - 1}} (\Delta\alpha) \quad (31)$$

and

$$\frac{p_e}{p_{sh}} = 1 - \frac{\gamma M_{sh}^2}{\sqrt{M_{sh}^2 - 1}} (\Delta\alpha) \quad (32)$$

where p_{sh} and M_{sh} are local pressure and Mach number at the shoulder for $\alpha = 0$, and p_c and p_e denote compression and expansion pressures at the assumed angle increment of $\Delta\alpha = \Delta v$ in radians. Equations (31) and (32) can be combined to obtain

$$\left(\frac{p_c - p_e}{p_\infty} \right)_{sh} = \frac{4M_{sh}^2}{\sqrt{M_{sh}^2 - 1}} \left(\frac{p_{sh}}{p_\infty} \right) \frac{\Delta\alpha}{M_\infty^2} \quad (33)$$

This expression represents the lifting-pressure coefficient at the shoulder position in terms of the shoulder pressure p_{sh} at $\alpha = 0^\circ$. The pressure at the shoulder can be obtained from a Prandtl-Meyer expansion from the sonic ring on the nose face. The sonic ring location, θ^* , is readily obtained from the modified Newtonian expression,

$$\sin^2 \theta^* = \frac{\frac{p^*}{p_{t2}} - \frac{p_\infty}{p_{t2}}}{1 - \frac{p_\infty}{p_{t2}}}$$

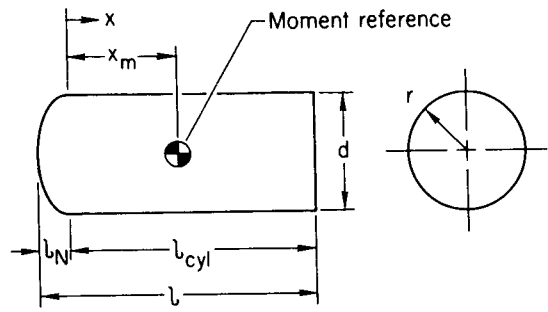
with

$$\frac{p^*}{p_{t2}} = \left(1 + \frac{\gamma - 1}{2} \right)^{-\frac{\gamma}{\gamma - 1}} \quad \text{for } M^* = 1$$

It is assumed that γ is constant from the stagnation point to the sonic ring, so that $\gamma = \gamma_{t2}$.

Now it is known (ref. 20) that at about 2 or 3 diameters rearward of the shoulder the pressure ratio (p/p_∞) is not that computed from Prandtl-Meyer theory (p_{sh}/p_∞) but is given closer by the blast-wave expression, equation (30). The determination of the pressure distribution just rearward of the shoulder requires further theoretical and experimental study. It is assumed as a first estimate, however, that the variation in pressure from the Prandtl-Meyer value at the shoulder p_{sh} to the blast-wave value at the base p_b is linear with x . Thus, for the dimensions in sketch (f),

$$\frac{p}{p_\infty} = \left(\frac{p}{p_\infty} \right)_{sh} - \frac{x}{l_{cyl}} \left[\left(\frac{p}{p_\infty} \right)_{sh} - \left(\frac{p}{p_\infty} \right)_b \right] \quad (34)$$



Sketch (f)

~~CONFIDENTIAL~~

For longer bodies than that considered, a better estimate might be obtained by using a blast-wave pressure distribution rearward of about 3 diameters from the nose. It is further assumed (following Seiff, ref. 23) that an expression of the same form as equation (33) can be used to estimate $(p_c - p_e)/q_\infty$ rearward of the shoulder; that is,

$$\frac{p_c - p_e}{q_\infty} \approx \frac{4M_{sh}^2}{\sqrt{M_{sh}^2 - 1}} \left(\frac{p}{p_\infty} \right) \frac{\Delta\alpha}{M_\infty^2} \quad (35)$$

with local $M \approx M_{sh}$ for short bodies.

For a cosine variation in pressure from the compression to the expansion side of the cylinder, the resulting changes in C_N and C_m are

$$\Delta C_{N,cyl} = \frac{1}{2r} \int_{l_N}^l \left(\frac{p_c - p_e}{q_\infty} \right) dx \quad (36)$$

and

$$\Delta C_{m,cyl} = - \frac{1}{2rl} \int_{l_N}^l \left(\frac{p_c - p_e}{q_\infty} \right) (x - x_m) dx \quad (37)$$

With equations (34) and (35) substituted into equations (36) and (37), there are obtained

$$C_{N\alpha,cyl} = \frac{4M_{sh}^2}{M_\infty^2 \sqrt{M_{sh}^2 - 1}} \left\{ \left(\frac{l_{cyl}}{d} \right) \left(\frac{p}{p_\infty} \right)_{sh} - \frac{1}{2} \left(\frac{l}{d} + \frac{l_N}{d} \right) \left[\left(\frac{p}{p_\infty} \right)_{sh} - \left(\frac{p}{p_\infty} \right)_b \right] \right\} \quad (38)$$

and

$$C_{m\alpha,cyl} = \frac{-4M_{sh}^2}{M_\infty^2 \sqrt{M_{sh}^2 - 1}} \left\{ \frac{1}{2} \left(\frac{p}{p_\infty} \right)_{sh} \left(\frac{l_{cyl}}{d} \right) \left(1 + \frac{l_N}{l} - \frac{2x_m}{l} \right) - \left[\left(\frac{p}{p_\infty} \right)_{sh} - \left(\frac{p}{p_\infty} \right)_b \right] \left[\frac{1}{3} \left(\frac{l}{d} \right) + \frac{1}{3} \left(\frac{l_N}{d} \right) \left(1 + \frac{l_N}{d} \right) - \frac{1}{2} \left(\frac{x_m}{d} \right) \left(1 + \frac{l_N}{d} \right) \right] \right\} \quad (39)$$

Although the estimative procedure followed herein is similar to that used by Seiff (ref. 23), the $C_{N\alpha,cyl}$ and $C_{m\alpha,cyl}$ expressions are considerably different because of the use of different axial-pressure relations. Seiff assumes a blast-wave distribution from the body base to the nose shoulder that

~~CONFIDENTIAL~~

predicts shoulder pressures of the order of about five to ten times higher than those obtained by Prandtl-Meyer theory. Hence, his expression for $C_{N\alpha, cyl}$ gives much higher values of normal force. In the notation of the present report, the blast-wave equation used by Seiff for p/p_∞ and the derived expressions for $C_{N\alpha, cyl}$ and x_{cp} (measured from the shoulder) are as follows:

$$\frac{p}{p_\infty} = \frac{f(\gamma) M_\infty^2 C_{DN}^{1/2}}{\frac{x}{d}} \quad (40)$$

$$C_{N\alpha, cyl} = \frac{4M^2}{\sqrt{M^2 - 1}} f(\gamma) C_{DN}^{1/2} \ln\left(\frac{l}{l_N}\right) \quad (41)$$

$$x_{cp} = \frac{l_{cyl}}{\ln(l/l_N)} \quad (42)$$

Because of the assumptions involved in the derivation of equations (38), (39), (41), and (42), they should be applied with extreme caution pending further study of pressure distributions just downstream of the nose shoulder.

RESULTS AND DISCUSSION

Results from the force and moment tests at $M_\infty = 17.2$ are presented in figures 8 and 9 for the Apollo-type and Polaris-type models, respectively. For the Apollo configuration there is very little difference between the data for the 2.25-inch and 5-inch models ($Re = 0.014 \times 10^6$ and 0.038×10^6), and in the remainder of the report only data from the 5-inch models are used. For the Polaris configuration (with and without flare) the C_N and C_m data versus α were used to determine values of $C_{N\alpha}$ and $C_{m\alpha}$ (at $\alpha = 0^\circ$) which are used in a latter discussion.

In this section of the report aerodynamic characteristics computed by the analytical methods outlined in the previous section are compared with the experimental results for $M_\infty = 17.2$ and with other available data for lower Mach numbers. All available experimental data are not included, but enough data are used to demonstrate the primary changes in the forces and pitching moments throughout the Mach number range from about 2 to 17. For convenience and clarity the Apollo and Polaris results are discussed separately.

Apollo-Type Vehicle

Modified Newtonian theory compared with experiment for angles of attack from 0° to 180° .— The degree of usefulness of modified Newtonian theory for

estimating the force and moment characteristics of Apollo-type vehicles at hypersonic Mach numbers is demonstrated in figure 8. Here aerodynamic coefficients computed by modified Newtonian theory are compared with experimental data obtained at $M_\infty = 17.2$ with models (of diameter $d = 2.5$ and 5 in.) in the Ames arc-heated aerodynamic wind tunnel. It is readily seen that the general trends in the variations of the coefficients with angle of attack are predicted reasonably well by the theory, although the absolute magnitudes at some α 's are not satisfactorily predicted.

Certain general disparities observed between modified Newtonian theory and experiment at $M_\infty = 17.2$ also can be observed at lower Mach numbers. They can be seen from a study of figure 10 where theory is compared not only with data for $M_\infty = 17.2$ but also with data for $M_\infty = 3.3$ and 5.4 (ref. 24) obtained in the Ames 1- by 3-Foot Supersonic Wind Tunnel. Over this Mach number range there are no significant changes in the computed aerodynamic characteristics because $C_{p\text{stag}}$ changes only from about 1.78 (the perfect-gas value for $M_\infty = 3.3$ in a cold tunnel) to 1.85 (the value for $M_\infty = 17.2$ and $h_{t1} = 1000$ Btu/lb with equilibrium flow in a hot tunnel and in the gas cap ahead of a model). However, there are some changes in the experimental data. It is very evident that the C_N results (fig. 10(a)) at all Mach numbers are underestimated by theory at α greater than about 80° . It may be somewhat fortuitous, then, that the C_m data (fig. 10(c)) are predicted closely over this α range. At any rate, it is encouraging to note that the primary trim angle of attack at $\alpha = 147^\circ$ is given both by theory and experiment throughout the Mach number range (fig. 10(c)). The secondary trim point predicted by theory at an angle of attack of about 50° does not agree as well with the data. In fact, at $M_\infty = 17.2$ there is not a secondary trim point indicated from these experimental results. The disparities between the calculated and experimental coefficients of C_L , C_D , L/D , and x_{cp}/d can be observed in figures 10(d) through 10(g).

Because lift-drag ratio at the primary trim condition ($\alpha = 147^\circ$) is of particular importance for entry trajectory and corridor analyses, the variation of trim L/D as a function of M_∞ is presented in figure 11. In this figure, results from figure 10 are supplemented with data from reference 25 (for $M_\infty = 1.5$ to 10) and with data (for $M_\infty = 14.2$) from a preliminary test in the Ames pilot arc tunnel (ref. 26). It is seen that the experimental results are near the predicted constant value of 0.51 at all Mach numbers, although there is a slight decrease in experimental trim L/D at the highest Mach numbers in accord with the decrease in C_L with increase in M_∞ (fig. 10(d)).

Comparisons of theoretical and experimental values of C_A versus Mach number at angles of attack of 0° and 180° . In figure 12 theoretical and experimental variations of C_A with Mach number are compared for the Apollo-type configuration at angles of attack of 0° and 180° . At $\alpha = 0^\circ$ (conical portion of vehicle forward) the experimental variation of C_A with M_∞ is given closely by cone theory with equations (8) and (9), whereas the modified Newtonian method underestimates experiment at all Mach numbers (fig. 12(a)). For this comparison, data from reference 25 are used with the data from the present investigation to cover a Mach number range from about 1.5 to 17.2 . At $\alpha = 180^\circ$ (blunt face forward) the experimental variation of C_A with M_∞

~~CONFIDENTIAL~~

is predicted much closer by the flow continuity method of reference 16 than by modified Newtonian theory (fig. 12(b)).² Newtonian theory, which is known to overpredict the pressures near the outer edges of blunt bodies, obviously overestimates the axial-force coefficients. It is noted in figure 12 that the data from reference 25 are for both total and forebody axial force. However, as shown, there is negligible contribution of afterbody pressure on total axial force at Mach numbers above about 5, and if further refinement to the calculative process were made to account for afterbody pressure, it would be of importance only at the lower Mach numbers.

Experimental afterbody pressures.- Although the afterbody pressures have little effect on the axial forces throughout the hypersonic Mach number range they should be studied because of possible interest from other considerations (e.g., afterbody design for heating). In figure 13 experimental data of afterbody pressure divided by stagnation pressure are presented as a function of Mach number for models oriented at $\alpha = 0^\circ$ and 180° . These data, obtained from reference 25 and from the present tests for Reynolds numbers from 0.03×10^6 to 2.4×10^6 , show that there is considerable decrease in p_a/p_{t_2} with increase in M_∞ up to values of M_∞ of about 5, after which the pressures level off. At the lower Mach numbers (below about 3) model orientation has little or no effect on the afterbody pressures. Throughout the hypersonic range, however, the afterbody pressures are consistently lower for the models at $\alpha = 0^\circ$ (conical portion forward). It is not certain whether this effect of model orientation results from a natural change in the afterbody flow-separation pattern or from a change attributable to support interference. It is believed, however, that any effect of the support may be small, since the data of reference 25 are consistent with the data of the present tests and yet were obtained with a side support that was much different from the sting support of the present tests. It also should be noted that unpublished data indicate an effect of Reynolds number on afterbody pressure.

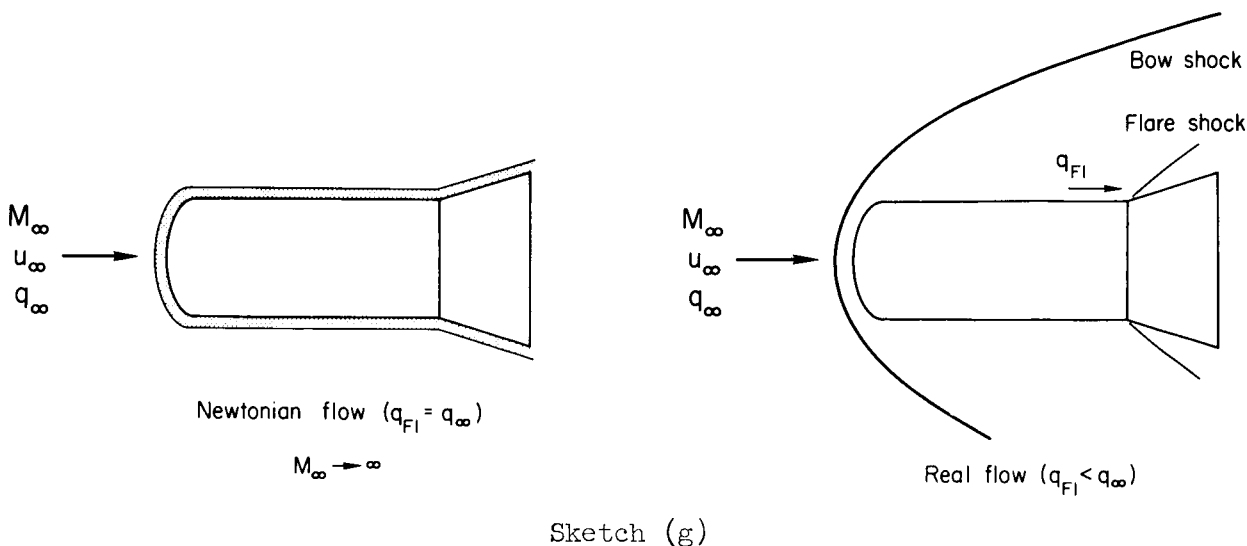
Comparisons of theoretical with experimental values of $C_{N\alpha}$, $C_{m\alpha}$, and x_{cp}/d versus Mach number at $\alpha = 0^\circ$.- As shown in figure 14 there is close agreement between theoretical and experimental values of $C_{N\alpha}$, $C_{m\alpha}$, and x_{cp}/d throughout the Mach number range for the Apollo configuration at $\alpha = 0^\circ$. As expected, there are only small differences between the results computed with modified Newtonian theory and with cone theory used in equations (10) and (11). The comparisons of theory with experiment are of interest because it has been suggested that conical bodies of about the same cone angle be used to minimize the sum of convective and radiative heat transfer for ballistic entry at superorbital speeds (i.e., ref. 27).

Polaris-Type Vehicle

Whereas the Apollo-type vehicle represents a configuration class for which modified Newtonian theory gives some useful estimates of the force and

²In the computation of $(CA)_{\alpha=180^\circ}$ by modified Newtonian theory, values of C_{pstag} were taken to correspond to the wind-tunnel conditions of M_∞ and h_t . Higher values would be computed for hypervelocity flight cases. Also, values of C_D by the method of reference 16 would approach those by modified Newtonian theory.

moment coefficients, the Polaris-type vehicle represents a class in which the Newtonian concept is inadequate except for obtaining the nose contribution near zero angle of attack. This inadequacy results primarily because the shock layer does not remain thin and closely wrapped around the body rearward of the nose but moves out from the body and flare (see sketch (g)), and a two-shock system results. There is a loss in dynamic pressure from the free-stream to the flare position which becomes large at hypersonic speeds.



Theory compared with experiment for complete vehicle.— In figure 15 theoretical curves of C_D , $C_{N_{\alpha}}$, and $C_{m_{\alpha}}$ calculated by modified Newtonian theory and by more refined methods which account for the dynamic-pressure loss are compared with experimental results from the present tests and from references 28 and 29. The comparisons clearly demonstrate the inadequacy of Newtonian theory and the merit of other methods (previously outlined in this report) for use in estimating the aerodynamic characteristics. A few comments concerning each part of figure 15 are next made for clarity.

In figure 15(a) the drag coefficients at Mach numbers above about 4 are predicted reasonably well by the method outlined previously in this report in which modified Newtonian theory is used only for the nose contribution, and cone theory with a reduced dynamic pressure is applied for the flare. Below a Mach number of about 4, however, the experimental results are underestimated because base pressure, which contributes significantly to the drag only at lower supersonic Mach numbers, has been neglected in the calculation. For $M_{\infty} = 17.2$ the drag is estimated closely either with the flare dynamic pressure q_{Fl} computed by equation (29) or by the equilibrium-flow method outlined in the appendix. As previously discussed, equation (29) was derived from ideal gas relations. In either method, however, the local pressure at the flare p_{Fl} is given from a blast-wave expression (eq. (30)), and the value of γ at the nose stagnation point is used. For the experimental tests in the arc-heated stream at $M_{\infty} = 17.2$ an equilibrium γ value of 1.26 was computed (see

appendix). It is seen in figures 15(b) and (c), however, that results computed with $\gamma = 1.26$ (the stagnation value) and $\gamma = 1.4$ (the free-stream value) are not too different.

In figure 15(b) the experimental $C_{N\alpha}$ data are generally overestimated by modified Newtonian theory (as expected) and underestimated by the other methods used. The curves computed by the other methods are generally low, probably because any theoretical lift contribution from the cylindrical portion of the body is omitted. Newtonian theory predicts zero $C_{N\alpha}$ for a cylinder. It is shown, however, that if experimental $C_{N\alpha}$ data for the body alone are added to the computed flare results there is very close agreement with the measured results for the complete vehicle. In this regard, note the comparisons shown at Mach numbers from about 3 to 6 and at 17 where experimental body-alone data were available.

The $C_{m\alpha}$ variation with M_∞ (fig. 15(c)), which is completely erroneous by Newtonian theory, is predicted reasonably well by the other methods. Here again though, as for $C_{N\alpha}$, it appears that a contribution for the cylindrical body should be included in the prediction to obtain the best agreement. Note that there is very close agreement between the measured results for the complete vehicle and those computed by adding experimental body-alone values to computed flare values. Apparently the flare contribution can be predicted reasonably well.

At this point it may be well to note that for some of the experimental tests there was visual (shadowgraph) evidence of moderate flow separation ahead of the flare. This was the case for the tests in the Ames 1- by 3-Foot Supersonic Wind Tunnel at Mach numbers below about 6 and Reynolds numbers below about 1.2×10^6 . Typical shadowgraph pictures from these tests are shown in figure 16. It can be noted that the flow separated well in front of the flare at $\alpha = 0^\circ$, but at small angles of attack separation decreased considerably on the windward lifting side and increased on the leeward side. The force and moment data from these tests, however, agree well with those of reference 29 which were obtained from free-flight wind-tunnel tests ($Re \geq 2.5 \times 10^6$) in which the separation region near the flare-cylinder junction was very small. Hence, it is believed that any effects of flow separation on the measured $C_{m\alpha}$ data which are presented are small, and comparison of "attached-flow" predicted results with these data is justified.

Theory compared with experiment for flare alone and body alone.— To further support the conclusion that the flare contribution to $C_{N\alpha}$ and $C_{m\alpha}$ can be predicted reasonably well by the method of this report, results computed for the flare alone are compared with experimental results in figure 17(a). It is seen that there is close agreement of theory with experiment. The experimental data were taken as the difference between measured results for the body with flare and the body alone.

To predict the body-alone contribution to $C_{N\alpha}$ and $C_{m\alpha}$, various analytical procedures (discussed in the analytical portion of the report) have been tried, and the computed results are compared with experiment in figure 17(b). The Newtonian concept predicts only a nose contribution to $C_{N\alpha}$ and $C_{m\alpha}$, and it is

seen that this contribution underestimates $C_{N_{\alpha,B}}$ for the body (nose plus cylinder) throughout the Mach number range. It is probably fortuitous then that $C_{m_{\alpha,B}}$ is given fairly well at the lower Mach numbers. With the addition of estimated cylinder contributions of $C_{N_{\alpha,cyl}}$ and $C_{m_{\alpha,cyl}}$ by equations (38) and (39) to the appropriate Newtonian nose contributions, the $C_{N_{\alpha,B}}$ prediction is improved, but the $C_{m_{\alpha,B}}$ prediction becomes worse. The equations of Seiff (eqs. (41) and (42)) also fail to predict correctly both the $C_{N_{\alpha,B}}$ and $C_{m_{\alpha,B}}$ results. In light of the large overprediction of $C_{N_{\alpha,B}}$ by the method of Seiff (ref. 23), it is probably fortuitous that $C_{m_{\alpha,B}}$ is given reasonably well.

The overprediction of $C_{N_{\alpha,B}}$ by the method of Seiff can be traced to the use in his derivation of $C_{N_{\alpha,cyl}}$ (eq. (41)) of a blast-wave expression (eq. (40)) which gives pressures near the nose-cylinder shoulder that are too high (see fig. 18). (As noted in the analytical portion of the present report, Seiff in ref. 23 ties the zero-angle-of-attack, blast-wave expression to a lifting-pressure relation.) Comparisons in figure 18 of theoretical with experimental pressures (from ref. 30) over a Polaris-type configuration confirm that the pressures at and near the shoulder are given considerably closer by Prandtl-Meyer theory than by blast-wave theory. Hence, it is not surprising that the prediction of $C_{N_{\alpha,B}}$ in figure 17(b) is given closer by the use of equation (38) in which the shoulder pressure is obtained from Prandtl-Meyer theory than by equation (41) in which blast-wave theory is used.

To analyze the difficulty in the prediction of $C_{m_{\alpha,B}}$ with equation (39) of the present report, it is well to look closely at the prediction of the pressure distribution over the entire body length. It is recalled that in the derivation of equations (38) and (39) the pressure distribution was assumed to vary linearly from the Prandtl-Meyer value at the shoulder to a blast-wave value at the base. Unfortunately, it is difficult to assess this assumption accurately from the pressure-distribution data of reference 30 (fig. 18(b)), because of the apparent effects of flow separation on the measured pressures rearward of about $x/d = 1.7$ (the approximate separation point based on the criteria of ref. 31). It appears, though, that without separation the pressure in front of the flare would be close to the predicted value of equation (30). At any rate, the assumption of a linear pressure distribution from the Prandtl-Meyer value at the shoulder to the blast-wave value at the flare appears to be fairly good. It is likely then that the failure of equation (39) for the cylinder moment stems from the use in its derivation of an approximate expression for the cylinder lifting-pressure coefficient (eq. (35)). This approximate expression (eq. (35)) is probably applicable only near the nose-cylinder shoulder but is applied over the entire cylinder length. Equations (38) and (39) of this report and those of Seiff (eqs. (41) and (42)) were all derived with this approximate relation and, hence, should be applied with caution.

Theoretical stability as a function of speed and altitude.— Since the static stability of a Polaris-type vehicle entering and flying within the atmosphere is maintained by the flare, the variation of flare pitching-moment coefficient with speed and altitude is of interest. In order to compute $C_{m_{\alpha}}$ however, the dynamic-pressure ratio q_F/q_{∞} must be determined (see eq. (17)). For the assumption of attached equilibrium flow from the free-stream condition

across the bow shock and to the flare, the variation of q_{F1}/q_{∞} with u_{∞} was computed for speeds from 8×10^3 ft/sec to 26×10^3 ft/sec at altitudes of 0, 105,000, and 250,000 feet. The calculation procedure is demonstrated in the appendix. For the same speeds and altitudes, values of q_{F1}/q_{∞} were also computed from the ideal gas relation, equation (29). Since the values of γ_{t_2} at the nose stagnation point were close to 1.2 for equilibrium flow at all conditions, a constant value of $\gamma = \gamma_{t_2} = 1.2$ was used in the calculations with equation (29). The results computed by these two procedures are in reasonably close agreement, as shown in figure 19, and confidence in the use of equation (29) for q_{F1}/q_{∞} is demonstrated. Large losses are predicted in dynamic pressure from the free stream to the flare position. However, over the speed and altitude ranges considered, q_{F1}/q_{∞} decreases only a small amount with increasing speed, and there is little effect of altitude on the dynamic-pressure ratio.

Effect of flow state on stability.— If the flow deviates considerably from equilibrium or becomes frozen between the nose stagnation point and the flare position, the q_{F1}/q_{∞} ratio can be expected to change. Just how much, of course, is important in the computation of the flare stability. To estimate the maximum limits of uncertainty in q_{F1}/q_{∞} , additional calculations have been made for the assumption of equilibrium flow to the nose stagnation point and then an instantaneous change to frozen flow from this point to the flare. Not only the chemical composition but the vibrational energy was assumed frozen, and frozen values of $\gamma = \gamma_{t_2}$ (as a function of Z_{t_2} , e.g., ref. 4) were used in equation (29) to compute values of q_{F1}/q_{∞} . The pressure relation (eq. (30)) from blast-wave analogy was assumed to be valid for both equilibrium and frozen flows. The results for the equilibrium and frozen-flow cases are compared in figure 20. It is very apparent that stability is improved with frozen flow because of the larger values of q_{F1}/q_{∞} obtained with the higher values of γ . In figure 21 the corresponding values of $C_{m_{\alpha}}$ for the flare alone are presented. These results, of course, reflect the q_{F1}/q_{∞} results. They are not, however, exactly proportional, since the local Mach numbers at the flare are slightly different for the frozen and equilibrium cases; hence slightly different values of cone normal-force coefficient $C_{N_{\alpha,c}}$ are used in equation (17) to compute $C_{m_{\alpha}}$. One can obtain estimates of $C_{m_{\alpha}}$ for the complete vehicle by merely adding the approximate experimental body-alone contribution ($C_{m_{\alpha,B}} \approx 0.1$) to the flare values in figure 21. Further research should be directed to the problem of predicting nonequilibrium and frozen-flow conditions from the nose to the flare of vehicles and the precise effect of these conditions on stability.

CONCLUSIONS

Models representative of the Apollo and Polaris vehicles have been tested at Mach number 17 in the Ames arc-heated aerodynamic wind tunnel. The Apollo-type models were tested at angles of attack from 0° (cone forward) to 180° (blunt face forward), and the Polaris-type models (all with a blunt nose but

with and without flare) were tested at angles of attack from about 0° to 12° . Data from these tests have been used with data from other tests at lower Mach numbers (above about 2) in a summary assessment of analytical methods for computing the static aerodynamic coefficients of entry-type vehicles.

For the Apollo-type vehicle the following conclusions have been reached:

1. The trends of the aerodynamic coefficients throughout the angle-of-attack range can be estimated reasonably well by modified Newtonian theory, although the absolute magnitudes of the coefficients at some angles of attack are not satisfactorily predicted.
2. The primary trim angle of attack remains fixed throughout the Mach number range at the value ($\alpha = 147^\circ$) predicted by modified Newtonian theory.
3. Trim lift-drag ratio remains close to that given by modified Newtonian theory ($L/D \approx 0.5$) which is constant throughout the Mach number range. A slight decrease in measured L/D , however, is noted at the higher Mach numbers.
4. With the conical portion of the vehicle facing forward ($\alpha = 0^\circ$), the experimental curve of axial-force coefficient versus Mach number is predicted somewhat closer by the use of Newtonian theory for the blunt apex plus cone theory for the conical surface than by modified Newtonian theory. Likewise, with the blunt face forward ($\alpha = 180^\circ$), closer agreement of theory with experiment is obtained by use of the method of NASA TN D-1423 than by modified Newtonian theory.
5. At Mach numbers above about 3 the measured afterbody pressures for the vehicle oriented with the blunt face forward ($\alpha = 180^\circ$) are two to three times greater than those for the vehicle oriented with the conical portion forward ($\alpha = 0^\circ$); however, at lower supersonic Mach numbers there is little or no effect of orientation on the afterbody pressures.

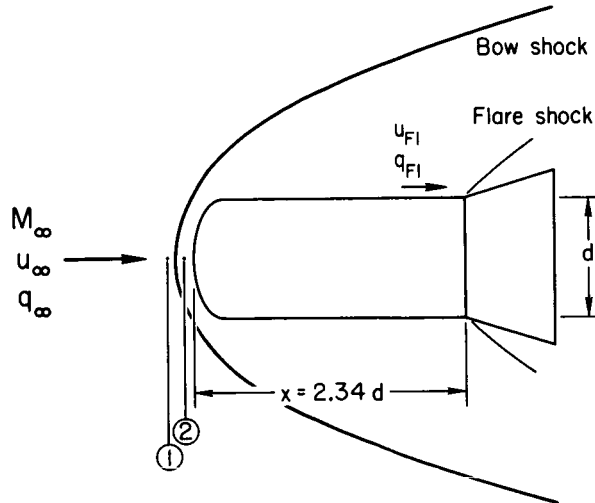
For the Polaris-type vehicle (with a blunt nose) the following conclusions have been reached:

1. The present study confirms previous research (e.g., NASA TM X-584) in demonstrating the inadequacy of modified Newtonian theory for estimating lift and static stability. Other methods (reviewed in this report) are available which agree closer with experiment.
2. The flare contribution to the vehicle lift and stability can be predicted reasonably well, but further research appears to be needed on the accurate determination of the cylindrical-body contribution.
3. For high speeds at various altitudes in the earth's atmosphere, calculated results indicate that a significant increase in stability can result from a change in the body-flow state from equilibrium to frozen.

Ames Research Center
National Aeronautics and Space Administration
Moffett Field, Calif., March 5, 1965

APPENDIX

SAMPLE COMPUTATION OF DYNAMIC PRESSURE AT FLARE OF POLARIS-TYPE VEHICLE FOR EQUILIBRIUM FLOW



Wind Tunnel Case

The following steps demonstrate the procedure for calculating q_{F1}/q_∞ with the use of available charts for equilibrium air flow in a wind tunnel. The calculation is based on the following set of test conditions:

$$M_\infty = 17.2$$

$$h_{t1} = 1000 \text{ Btu/lb}$$

$$p_{t1} = 68 \text{ atm} = 1000 \text{ lb/in.}^2$$

$$x = 2.34 d$$

Step 1.— For specified M_∞ , h_{t1} , and p_{t1} obtain p_∞/p_t , p_{t2}/p_{t1} , and q_∞/p_{t1} from reference 2 and compute

$$p_\infty = \left(\frac{p_\infty}{p_{t1}} \right) p_{t1} = (4.20 \times 10^{-6}) 68 = 2.856 \times 10^{-5} \text{ atm}$$

$$p_{t_2} = \left(\frac{p_{t_2}}{p_{t_1}} \right) p_{t_1} = (1.65 \times 10^{-4}) 68 = 1.122 \times 10^{-2} \text{ atm}$$

and

$$q_{\infty} = \left(\frac{q_{\infty}}{p_{t_1}} \right) p_{t_1} = (9.0 \times 10^{-5}) 1000 = 9.0 \times 10^{-2} \text{ lb/in.}^2$$

Step 2.— For known p_{t_2} (step 1) and $h_{t_2} = h_{t_1}$ obtain (from ref. 21)

$$\frac{s_{t_2}}{R} = 35.9$$

$$T_{t_2} = 2000^{\circ} \text{ K} = 3600^{\circ} \text{ R}$$

and $\gamma_{t_2} = 1.26$ from reference 22 for known p_{t_2} and T_{t_2} .

Step 3.— From equation (30) in the text,

$$\frac{p_{F1}}{p_{\infty}} = 0.85 \frac{f(\gamma) M_{\infty}^2 C_{DN}^{1/2}}{\frac{x}{d}} + 0.55$$

From modified Newtonian theory $C_{DN} = 1.37$, and for $\gamma = \gamma_{t_2} = 1.26$, $f(\gamma) = 0.057$ (interpolated from table in text). Then compute

$$\frac{p_{F1}}{p_{\infty}} = \frac{0.85 \times 0.057 \times (17.2)^2 \times (1.37)^{1/2}}{2.34} + 0.55 = 7.71$$

Then

$$p_{F1} = \left(\frac{p_{F1}}{p_{\infty}} \right) p_{\infty} = (7.71) (2.856 \times 10^{-5}) = 2.20 \times 10^{-4} \text{ atm}$$

Step 4.— For known p_{F1} (step 3) and $s_{F1}/R = s_{t_2}/R$ (step 2) obtain (from ref. 21)

$$h_{F1} = 355 \text{ Btu/lb}$$

$$T_{F1} = 810^{\circ} \text{ K} = 1458^{\circ} \text{ R}$$

and

$$Z_{F1} = 1$$

Step 5. - Then compute u_{F1} , ρ_{F1} , q_{F1} , and q_{F1}/q_{∞} as follows:

$$u_{F1} = 223.6 \sqrt{h_{t2} - h_{F1}} = 223.6 \sqrt{1000 - 355} = 5680 \text{ ft/sec}$$

$$\rho_{F1} = 1.234 \frac{p_{F1}}{Z_{F1} T_{F1}} = \frac{1.234 \times 2.20 \times 10^{-4}}{1 \times 1458} = 1.862 \times 10^{-7} \text{ slugs/ft}^3$$

$$q_{F1} = \frac{1}{2} \rho_{F1} u_{F1}^2 = \frac{1}{2} \times 1.862 \times 10^{-7} \times (5.68 \times 10^3)^2$$

$$= 3.00 \text{ lb/ft}^2 \text{ or } 2.08 \times 10^{-2} \text{ lb/in.}^2$$

therefore

$$\frac{q_{F1}}{q_{\infty}} = \frac{2.08 \times 10^{-2}}{9.0 \times 10^{-2}} = 0.231$$

Earth Atmosphere Flight Case

The following steps demonstrate the procedure for calculating q_{F1}/q_{∞} with the use of available charts for equilibrium air flow in flight in the earth's atmosphere. The calculation is based on the following specified conditions:

$$u_{\infty} = 18,000 \text{ ft/sec at } 105,000 \text{ ft altitude}$$

$$x = 2.34 \text{ d}$$

Step 1. - For specified altitude obtain (from ref. 11)

$$p_{\infty} = 8.781 \times 10^{-3} \text{ atm}$$

$$p_{\infty} = 2.747 \times 10^{-5} \text{ slugs/ft}^3$$

~~CONFIDENTIAL~~

$$h_{\infty} = 94.2 \text{ Btu/lb}$$

$$a_{\infty} = 9.751 \times 10^2 \text{ ft/sec}$$

and compute

$$M_{\infty} = \frac{u_{\infty}}{a_{\infty}} = \frac{18 \times 10^3}{9.751 \times 10^2} = 18.46$$

$$q_{\infty} = \frac{1}{2} \rho_{\infty} u_{\infty}^2 = \frac{1}{2} (2.747 \times 10^{-5}) (18 \times 10^3)^2 = 4.450 \times 10^3 \text{ lb/ft}^2$$

Step 2.- For specified altitude and u_{∞} obtain (from ref. 11)

$$\frac{p_{t_2}}{p_{\infty}} = 463$$

$$\frac{h_{t_2}}{h_{\infty}} = 70.0$$

and compute

$$p_{t_2} = p_{\infty} \left(\frac{p_{t_2}}{p_{\infty}} \right) = 8.781 \times 10^{-3} (463) = 4.065 \text{ atm}$$

$$h_{t_2} = h_{\infty} \left(\frac{h_{t_2}}{h_{\infty}} \right) = 94.2 (70.0) = 6594 \text{ Btu/lb}$$

Step 3.- For known p_{t_2} and h_{t_2} obtain (from ref. 21)

$$\frac{s_{t_2}}{R} = 40.7$$

$$T_{t_2} = 6405^{\circ} \text{ K}$$

and $\gamma_{t_2} = 1.16$ from reference 22 for known p_{t_2} and T_{t_2} .

Step 4.- From equation (30),

$$\frac{p_{F1}}{p_{\infty}} = 0.85 \frac{f(\gamma) M_{\infty}^2 C_{DN}^{1/2}}{\frac{x}{d}} + 0.55$$

From modified Newtonian theory $C_{DN} = 1.37$, and for $\gamma = \gamma_{t_2} = 1.16$, $f(\gamma) = 0.048$ (interpolated from table in text). Then compute

$$\frac{p_{F1}}{p_{\infty}} = \frac{0.85 \times 0.048 \times (18.46)^2 (1.37)^{1/2}}{2.34} + 0.55 = 7.51$$

then

$$p_{F1} = \left(\frac{p_{F1}}{p_{\infty}} \right) p_{\infty} = 7.51 (8.781 \times 10^{-3}) = 6.59 \times 10^{-2} \text{ atm}$$

Step 5.— For known p_{F1} (step 4) and $s_{F1}/R = s_{t_2}/R$ (step 3) obtain (from ref. 21)

$$h_{F1} = 3380 \text{ Btu/lb}$$

$$T_{F1} = 3680^{\circ} \text{ K} = 6620^{\circ} \text{ R}$$

and

$$Z_{F1} = 1.19$$

Step 6.— Then compute u_{F1} , ρ_{F1} , q_{F1} , and q_{F1}/q_{∞} as follows:

$$u_{F1} = 223.6 \sqrt{h_{t_2} - h_{F1}} = 223.6 \sqrt{6594 - 3380} = 12,670 \text{ ft/sec}$$

$$\rho_{F1} = 1.234 \frac{p_{F1}}{Z_{F1} T_{F1}} = \frac{1.234 \times 6.59 \times 10^{-2}}{1.19 \times 6620} = 1.032 \times 10^{-5} \text{ slugs/ft}^3$$

$$q_{F1} = \frac{1}{2} \rho_{F1} u_{F1}^2 = \frac{1}{2} \times 1.032 \times 10^{-5} \times (12.67 \times 10^3)^2 = 828 \text{ lb/ft}^2$$

therefore

$$\frac{q_{F1}}{q_{\infty}} = \frac{828}{4450} = 0.186$$

~~CONFIDENTIAL~~

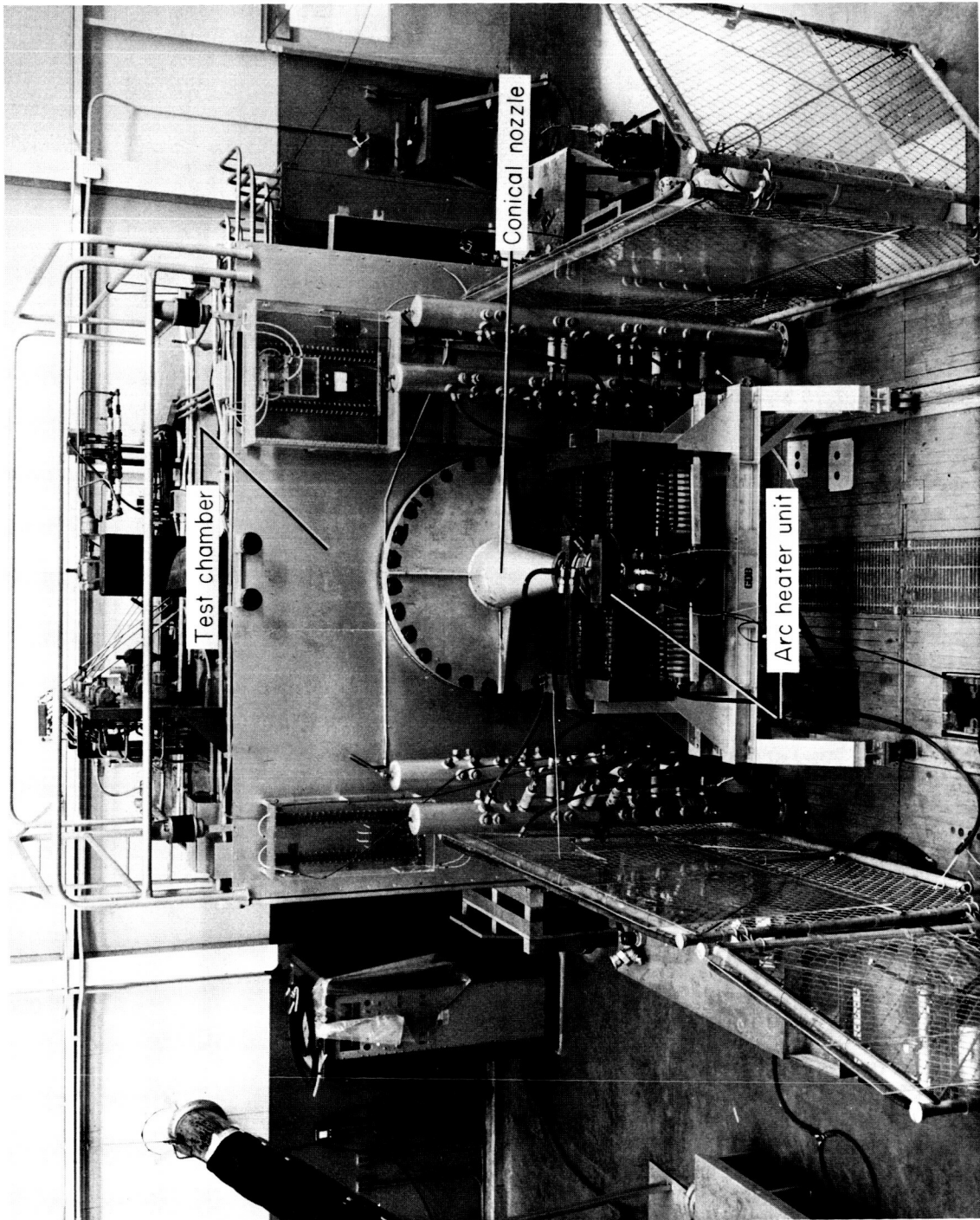
REFERENCES

1. Shepard, C. E.; and Winovich, Warren: Electric-Arc Jets for Producing Gas Streams With Negligible Contamination. ASME Plasma Jet Symposium paper 61-WA-247, Dec. 1961.
2. Jorgensen, Leland H.; and Baum, Gayle M.: Charts for Equilibrium Flow Properties of Air in Hypervelocity Nozzles. NASA TN D-133, 1962.
3. Winovich, Warren: On the Equilibrium Sonic-Flow Method for Evaluating Electric-Arc Air-Heater Performance. NASA TN D-2132, 1964.
4. Jorgensen, Leland H.: The Total Enthalpy of a One-Dimensional Nozzle Flow With Various Gases. NASA TN D-2233, 1964.
5. Fay, J. A.; and Riddell, F. R.: Theory of Stagnation Point Heat Transfer in Dissociated Air. J. Aero. Sci., vol. 25, no. 2, Feb. 1958, pp. 73-85, 121.
6. Compton, Dale L.; Winovich, Warren; and Wakefield, Roy M.: Measurements of the Effective Heats of Ablation of Teflon and Polyethylene at Convective Heating Rates From 25 to 420 Btu/ft² sec. NASA TN D-1332, 1962.
7. Boison, J. Christopher; and Curtiss, Howard A.: An Experimental Investigation of Blunt Body Stagnation Point Velocity Gradient. J. Aero. Sci., Feb. 1959.
8. Hilsenrath, Joseph; Beckett, Charles W.; Benedict, William S; Fano, Lilla; Hoge, Harold J.; Masi, Joseph F.; Nuttal, Ralph L.; Touloukian, Yerman S.; and Woolley, Harold W.: Tables of Thermal Properties of Gases. NBS Cir. 564, U.S. Department of Commerce, 1955.
9. Yalamanchili, Janardanarao: Non-Equilibrium Hypersonic Flow of Air in Hypersonic Nozzles and Around Blunt Bodies. Ph.D Thesis, Univ. of Minnesota, 1963.
10. Rainey, Robert W.: Working Charts for Rapid Prediction of Force and Pressure Coefficients on Arbitrary Bodies of Revolution By Use of Newtonian Concepts. NASA TN D-176, 1959.
11. Feldman, Saul: Hypersonic Gas Dynamic Charts for Equilibrium Air. Avco Res. Lab., Jan. 1957.
12. Hochstim, Adolph R.: Gas Properties Behind Shocks at Hypersonic Velocities. I. Normal Shocks in Air. Convair Rep. Z Ph (GP)-002, Jan. 30, 1957.
13. Cook, C. A.; Gilbert, L. M.; and Scala, S. M.: Normal Shock Wave Calculations in Air at Flight Speeds Up to 25,000 ft/sec. Document No. R 62SD 76, MSD, General Electric Co., Nov. 1962.

- ~~CONFIDENTIAL~~
14. Jorgensen, Leland H.; Spahr, J. Richard; and Hill, William A., Jr.: Comparison of the Effectiveness of Flares With That of Fins for Stabilizing Low-Fineness-Ratio Bodies at Mach Numbers From 0.6 to 5.8. NASA TM X-653, 1962.
 15. Ames Research Staff: Equations, Tables, and Charts for Compressible Flow. NACA Rep. 1135, 1953.
 16. Kaattari, George E.: Predicted Gas Properties in the Shock Layer Ahead of Capsule-Type Vehicles at Angles of Attack. NASA TN D-1423, 1962.
 17. Seiff, Alvin; and Whiting, Ellis: The Effect of the Bow Shock Wave on the Stability of Blunt-Nosed Slender Bodies. NASA TM X-377, 1960.
 18. Palermo, D. A.: Equations for the Hypersonic Flow Field of the Polaris Re-Entry Body. LMSD-480954, Lockheed Missiles and Space Division, Oct. 1960.
 19. Seiff, Alvin; and Whiting, Ellis E.: Calculation of Flow Fields From Bow-Wave Profiles for the Downstream Region of Blunt-Nosed Circular Cylinders in Axial Hypersonic Flight. NASA TN D-1147, 1961.
 20. Kuehn, Donald M.: Experimental and Theoretical Pressures on Blunt Cylinders for Equilibrium and Nonequilibrium Air at Hypersonic Speeds. NASA TN D-1979, 1963.
 21. Moeckel, W. E.; and Weston, Kenneth C.: Composition and Thermodynamic Properties of Air in Chemical Equilibrium. NACA TN 4265, 1958.
 22. Hansen, C. Frederick: Approximations for the Thermodynamic and Transport Properties of High-Temperature Air. NASA TR R-50, 1959.
 23. Seiff, Alvin: Atmosphere Entry Problems of Manned Interplanetary Flight. From "Engineering Problems of Manned Interplanetary Exploration," a volume of technical papers presented Sept. 30-Oct. 1, 1963 at AIAA meeting in Palo Alto, Calif.
 24. Stivers, Louis S., Jr.: Effects of Inclination of a Sting Support on the Supersonic Force and Moment Characteristics of an Apollo Model at Angles From -30° to $+185^{\circ}$. NASA TM X-1081, 1965.
 25. Gray, J. Don; and Jones, J. H.: Force and Pressure Tests on Apollo Configurations at Mach 1.5 Through 10. AEDC-TDR-63-17, Feb. 1963.
 26. Gowen, Forrest, E.; and Hopkins, Vaughn D.: A Wind Tunnel Using Arc-Heated Air for Mach Numbers From 10 to 20. Paper presented at Second National Symposium on Hypervelocity Techniques, Denver, Colorado, March 19 and 20, 1962.

- ~~CONFIDENTIAL~~
27. Allen, H. J.; Seiff, A.; and Winovich, W.: Aerodynamic Heating of Conical Entry Vehicles at Speeds in Excess of Earth Parabolic Speed. NASA TR R-185, 1963.
 28. Meijer, A. W.: Compilation of Data of Aerodynamic Scale Model Tests of the Polaris Re-entry Body. LMSD-4530, Lockheed Aircraft Corp., 1958.
 29. Kirk, Donn B.: Free-Flight Investigation of the Static Stability of Blunt-Nosed Flare-Stabilized Entry Bodies at Mach Numbers From 5 to 16. NASA TM X-584, 1962.
 30. Thickstun, W. R.; and Schermerhorn, V. L.: Polaris Ablation Study. Aerodynamics Research Report 161, NOLTR 61-90, Jan. 6, 1964.
 31. Kuehn, Donald M.: Laminar Boundary-Layer Separation Induced by Flares on Cylinders at Zero Angle of Attack. NASA TR R-146, 1962.

CONFIDENTIAL

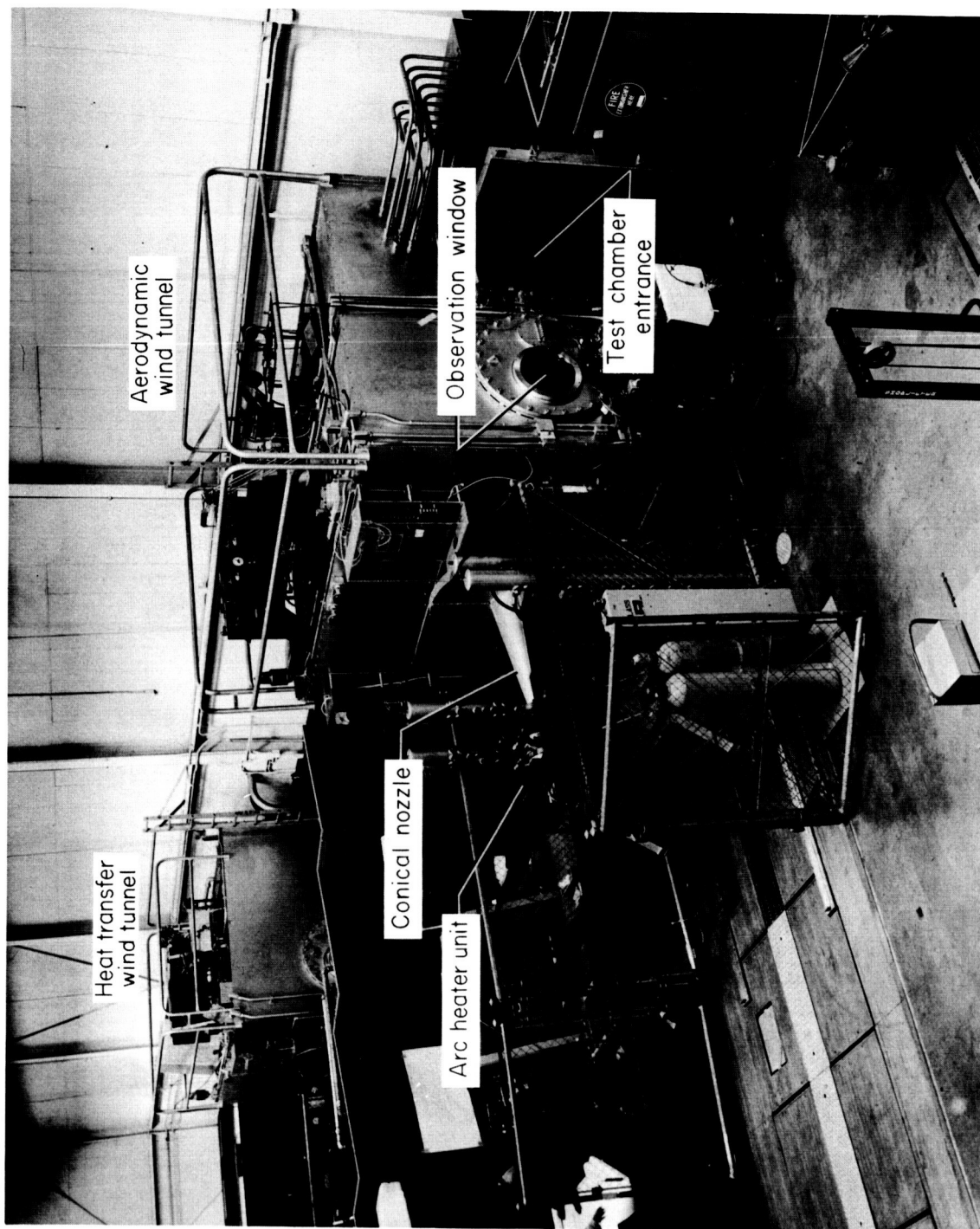


A-32168.1

(a) Front external view.

Figure 1.- Ames Arc-Heated Aerodynamic Wind Tunnel.

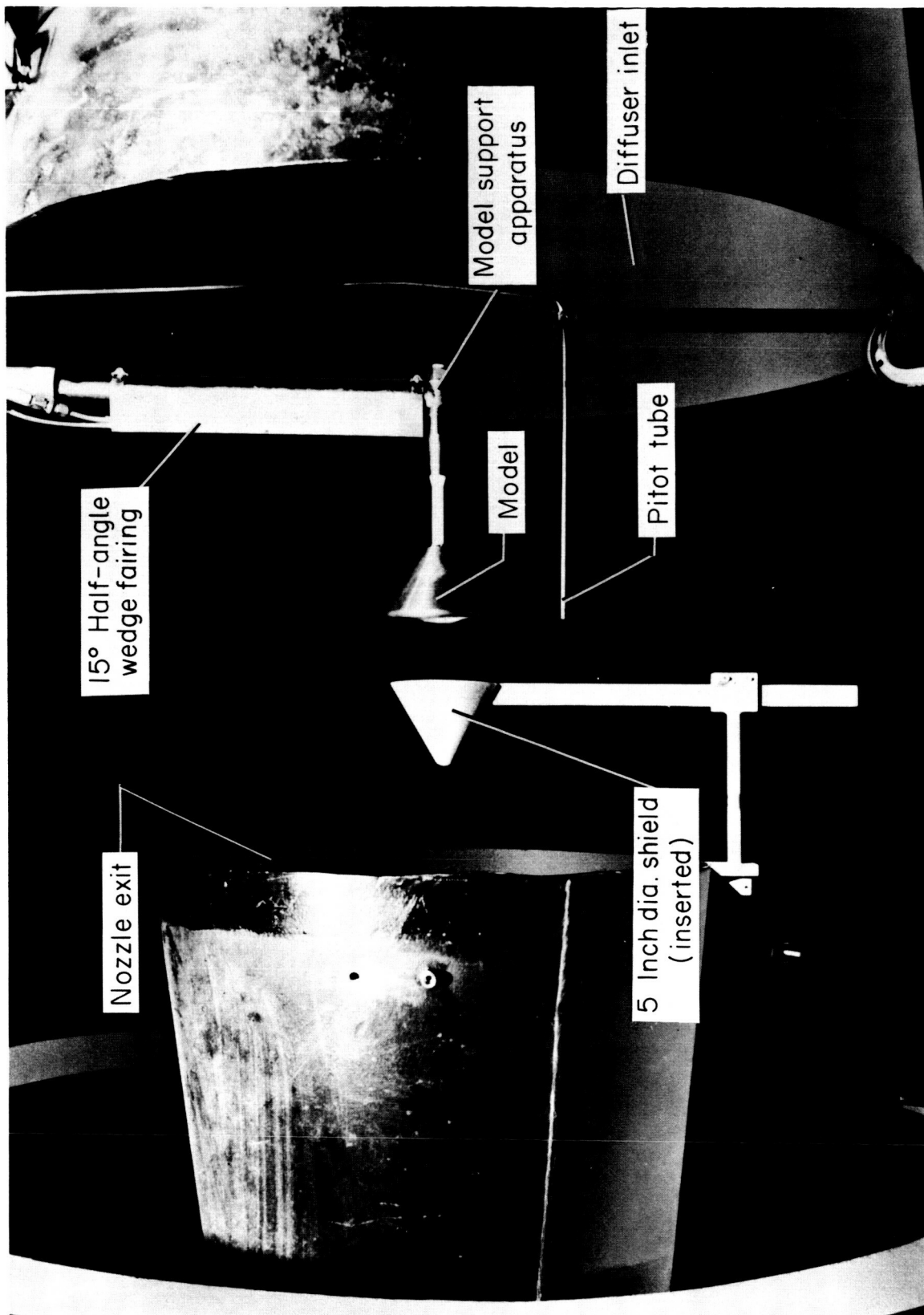
CONFIDENTIAL



A-32170.1

(b) Three-quarter external view.

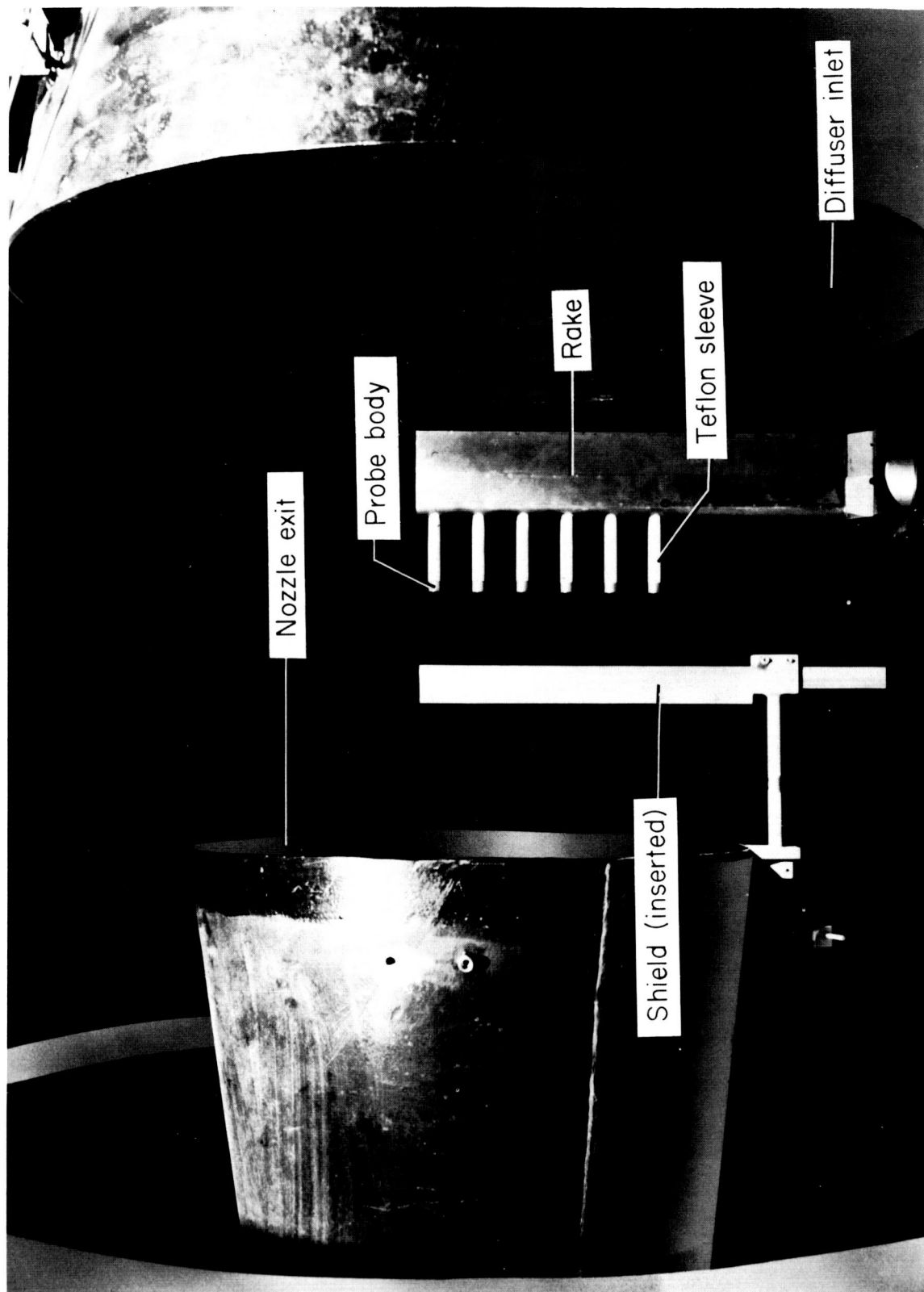
Figure 1.- Continued.



A-32035.1

(c) Typical elevation view of test chamber as seen through observation window.

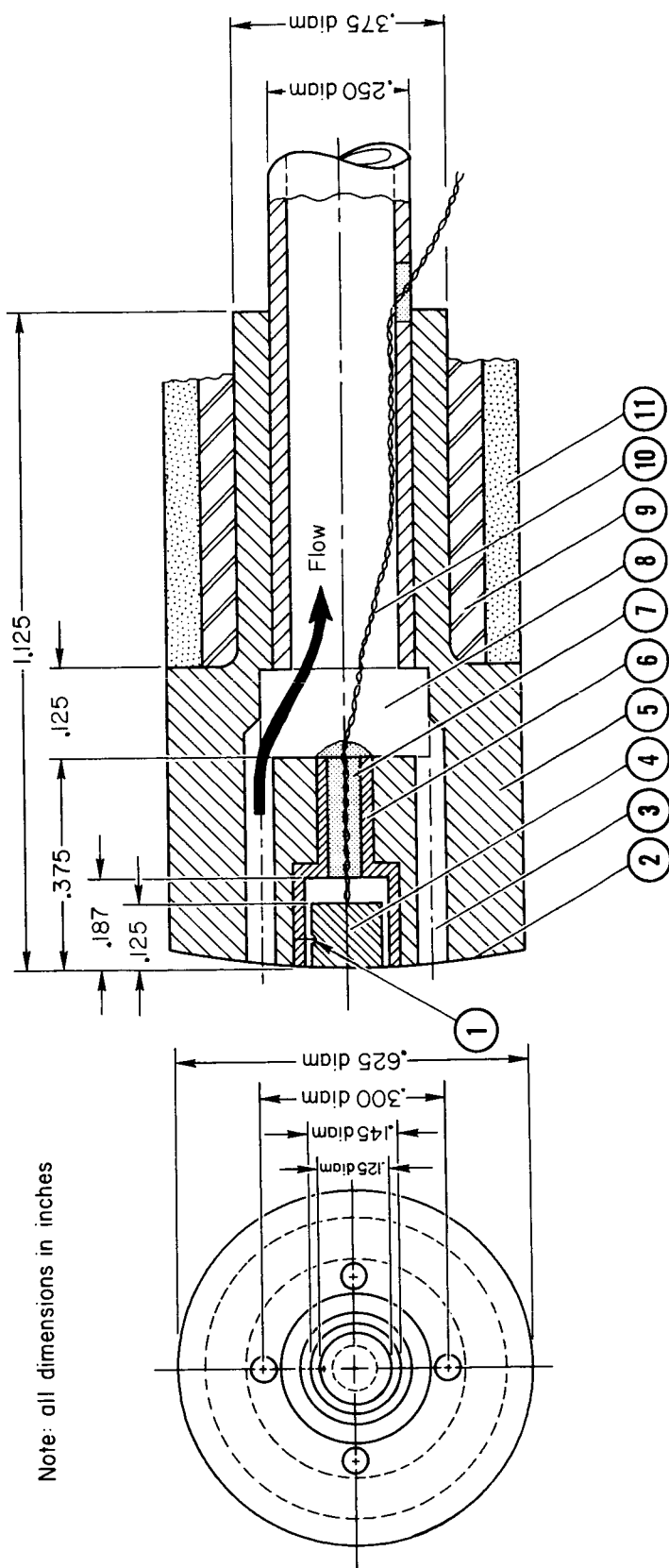
Figure 1.- Concluded.



A-32031.1

(a) Pitot pressure and calorimeter rake mounted in test chamber.

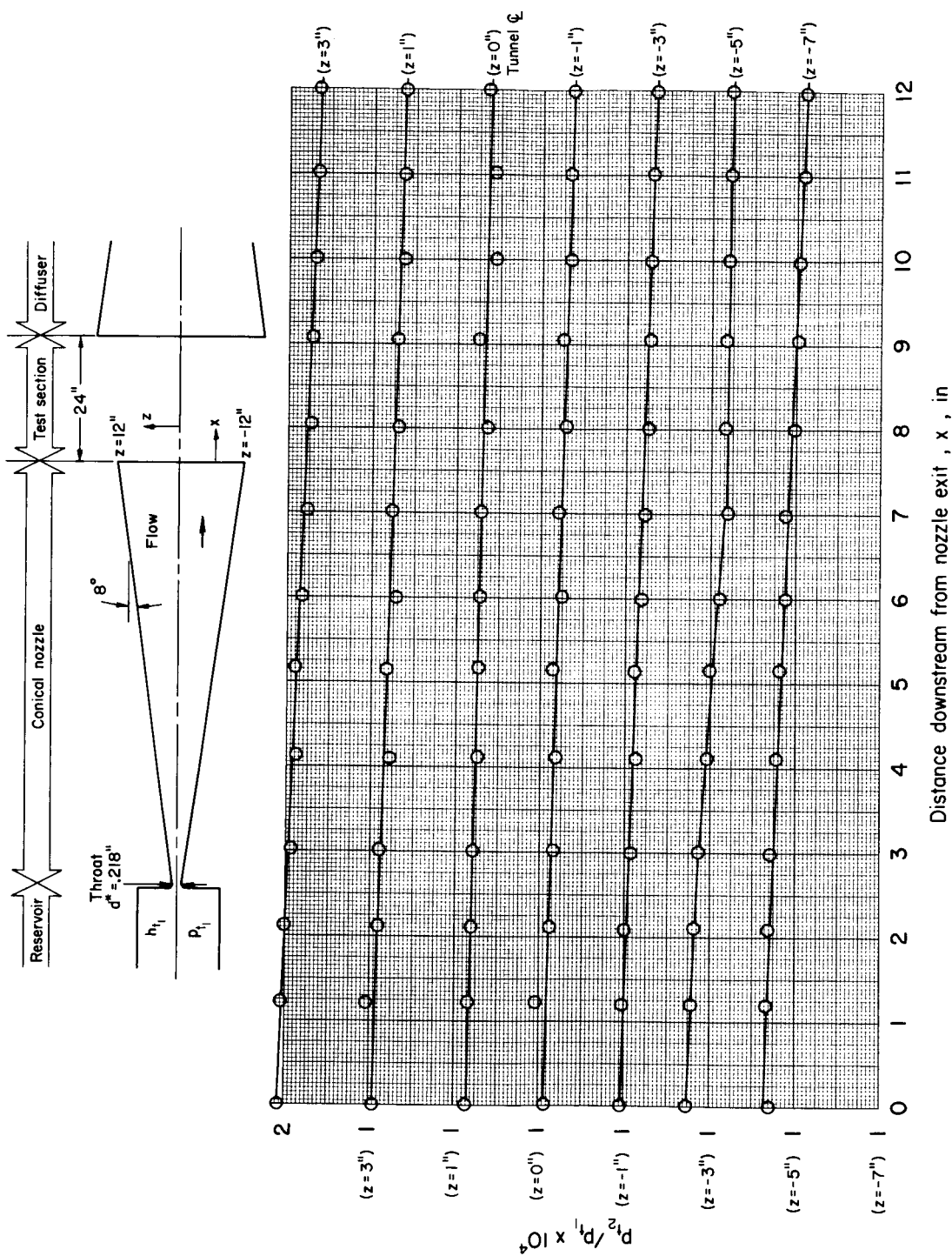
Figure 2.- Stream survey equipment.



- | | | | |
|---|---|----|---|
| 1 | Magnetic stainless steel wire, .005 diam, 3 at 120° | 7 | Epoxy seal |
| 2 | Radius of curvature = 2.000 | 8 | Pressure manifold from pitot tubes to pressure cell |
| 3 | Pitot tubes, .060 diam | 9 | Copper tube connecting probe body to rake |
| 4 | Heat plug (oxygen-free copper) | 10 | Copper-constantan thermocouple wire |
| 5 | Probe body (stainless steel) | 11 | Teflon sleeve |
| 6 | Heat plug support ring (stainless steel) | | |

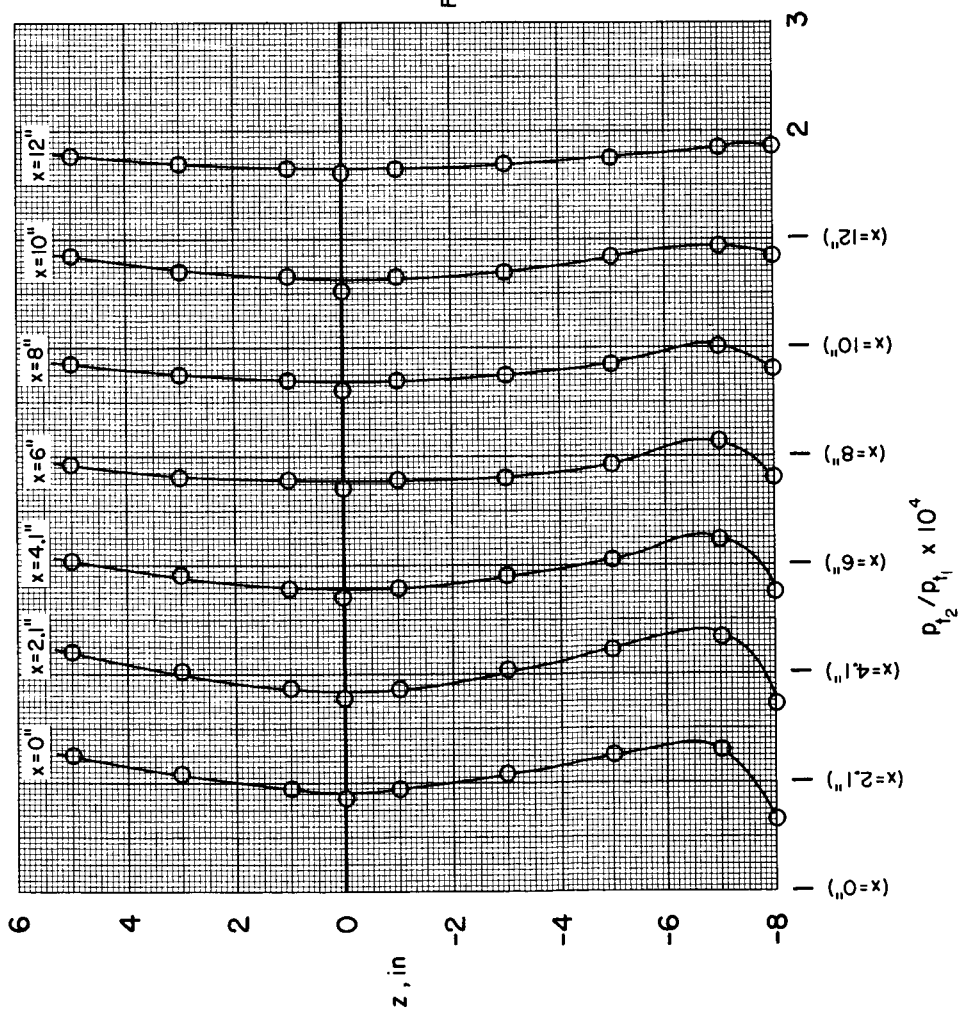
(b) Pitot-pressure and calorimeter-probe details.

Figure 2.- Concluded.



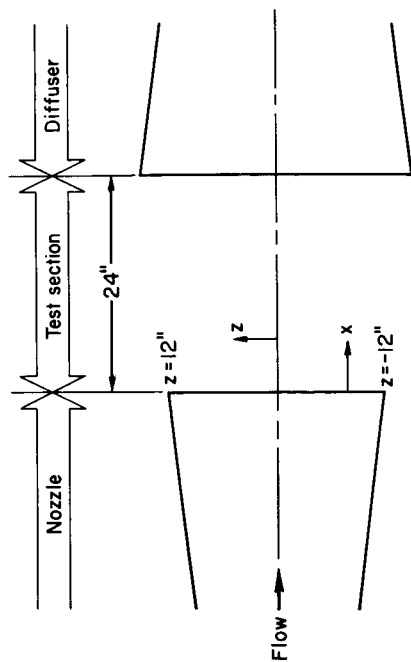
(a) Axial distributions of p_{t2}/p_{t1} .

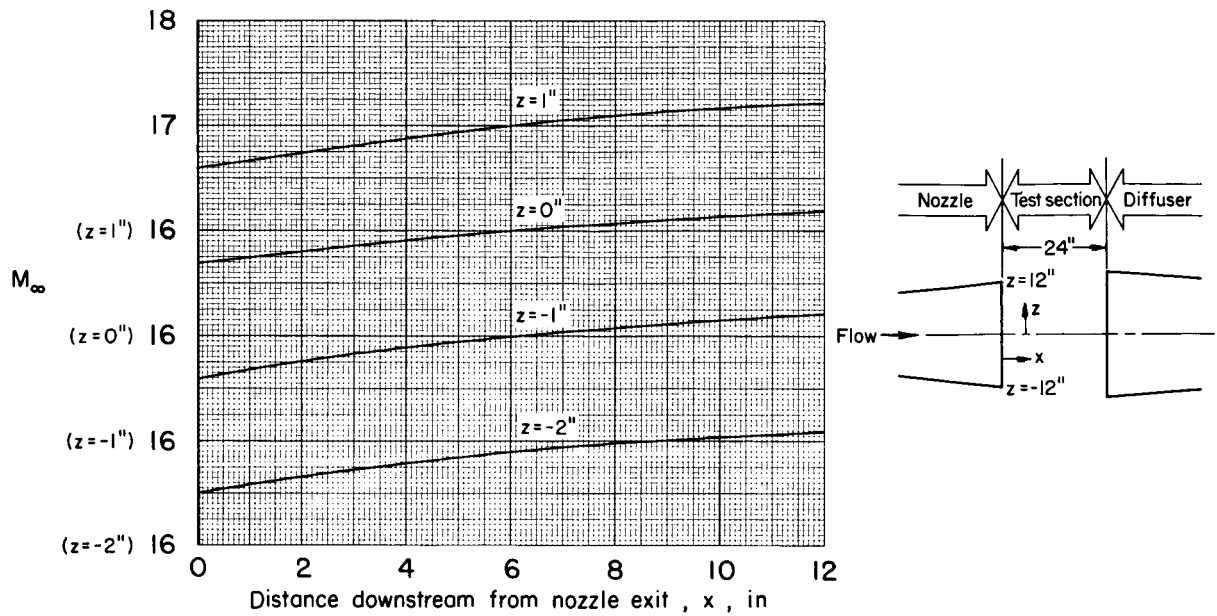
Figure 3.- Test-section survey distributions of pitot pressure and Mach number for $p_{t1} \approx 68$ atm and $h_{t1} \approx 1000$ Btu/lb.



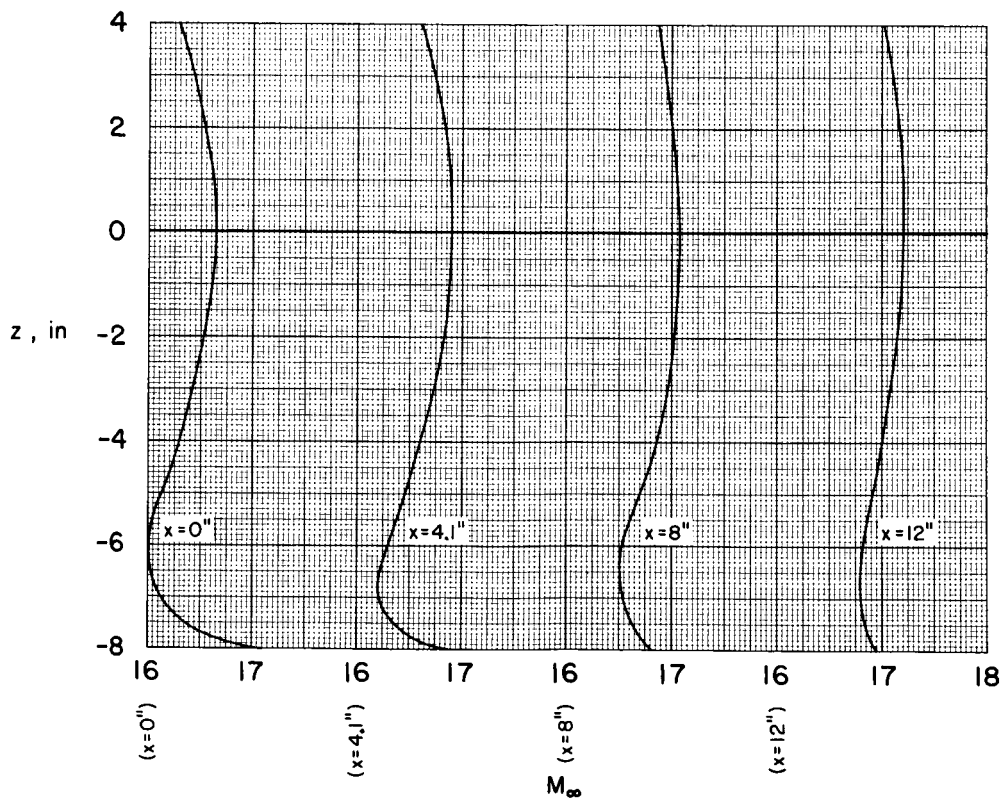
(b) Radial distributions of p_{t2}/p_{t1} .

Figure 3.- Continued.





(c) Axial distributions of M_∞ .



(d) Radial distributions of M_∞ .

Figure 3.- Concluded.

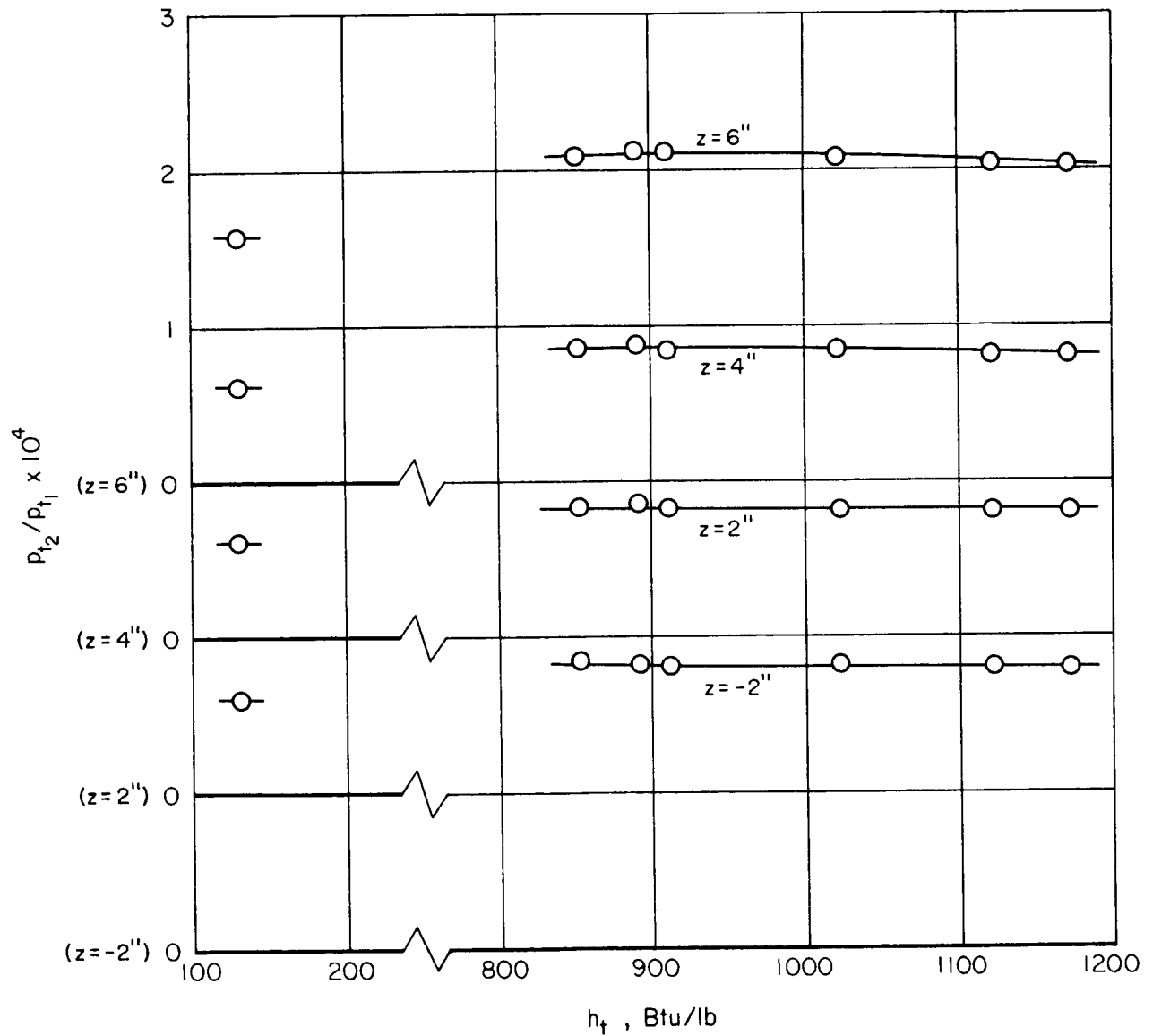
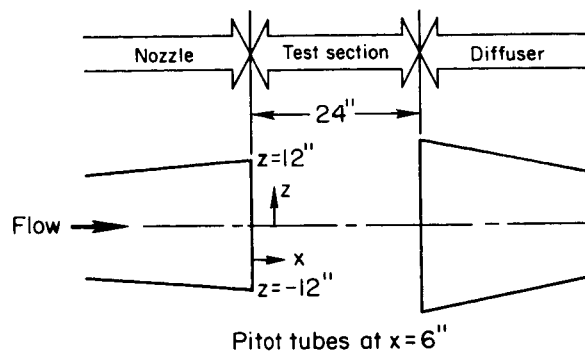


Figure 4.- Effect of total-enthalpy variation on pitot-pressure distributions in tunnel test section.

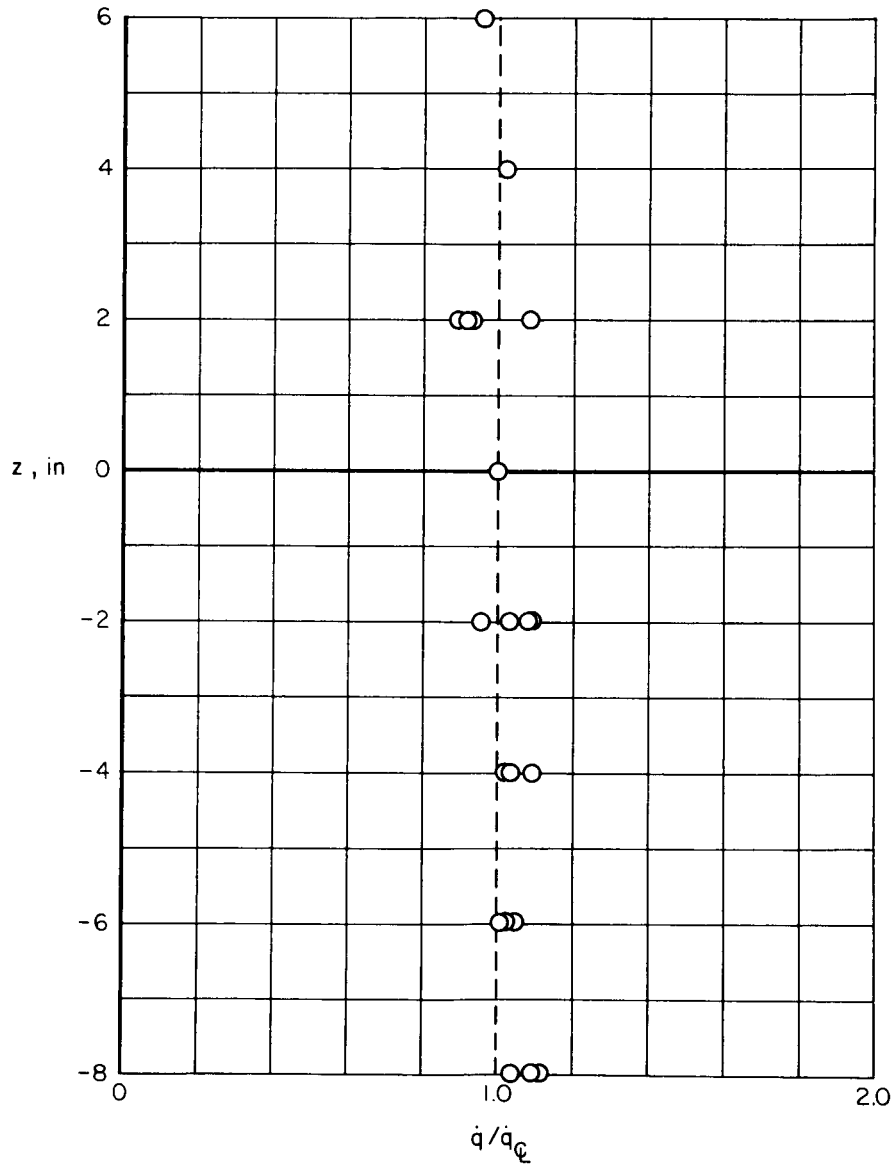
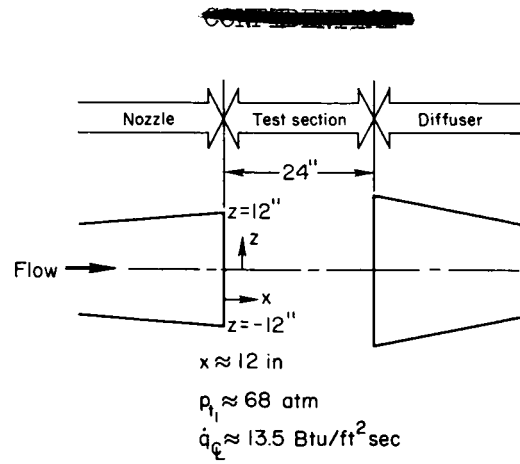
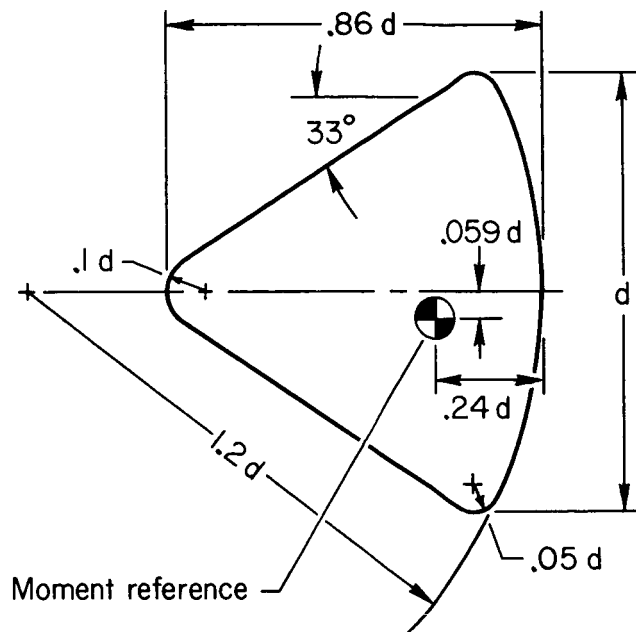


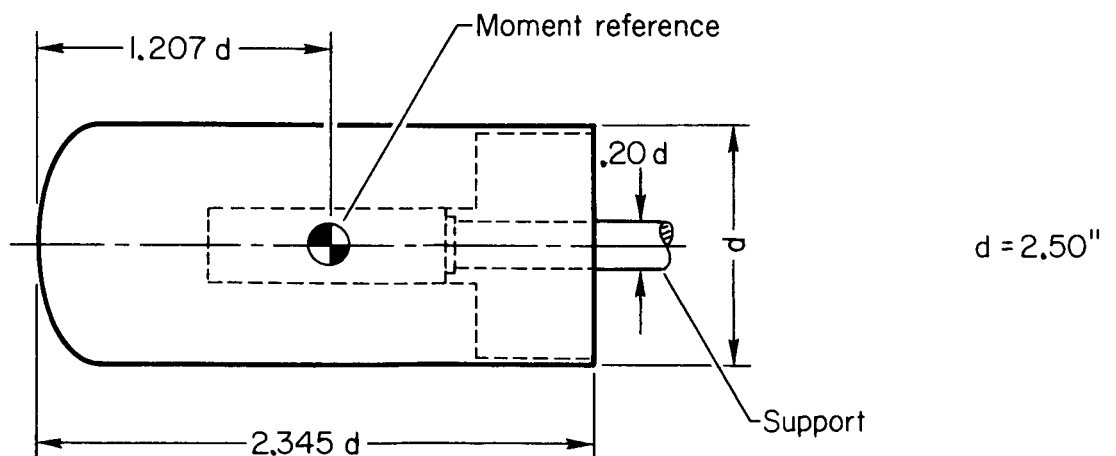
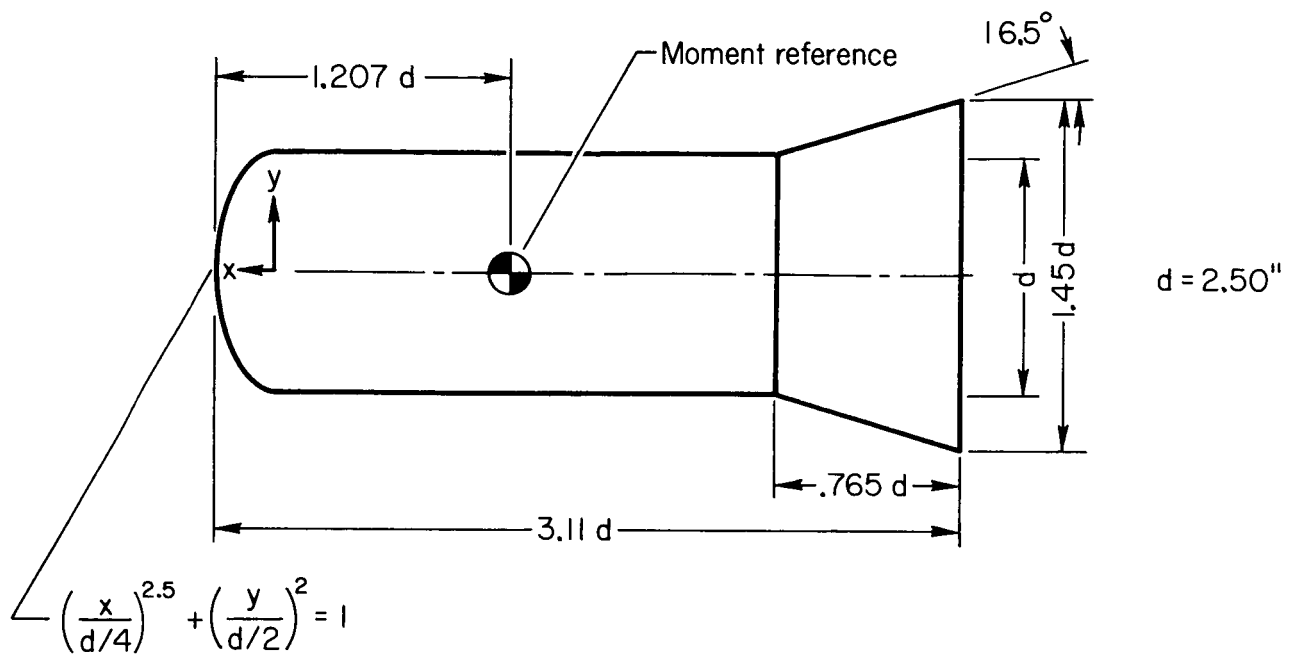
Figure 5.- Typical heating-rate distribution in tunnel test section.



See figs. 6(d) and 6(e) for mounting orientation of three models of $d=5.00''$ and five models of $d=2.25''$

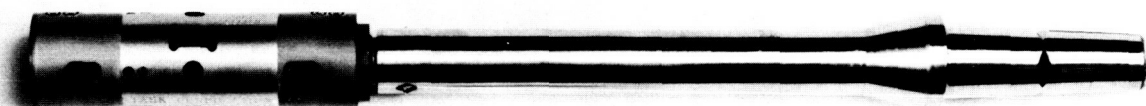
(a) Geometry of Apollo-type models.

Figure 6.- Models, balance, and mounting orientation.



(b) Geometry of Polaris-type models.

Figure 6.- Continued.

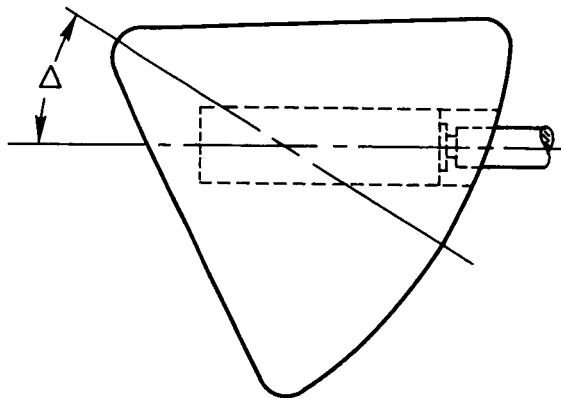


A-32307

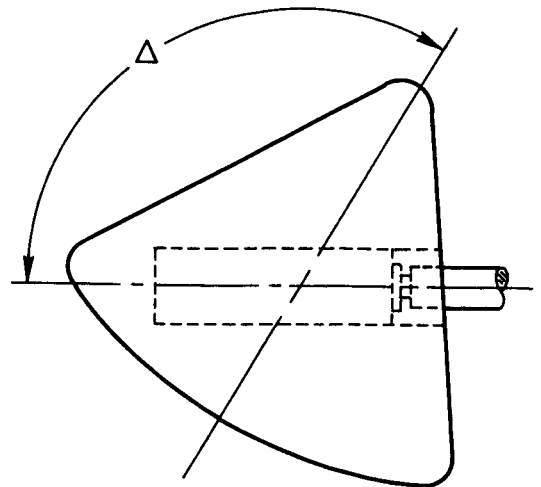
<u>Components Used</u>	<u>Rated Load, lb.</u>
Front Normal Force	± 2.5
Rear Normal Force	± 2.5
Axial Force	± 10.0

(c) Photograph of six-component balance.

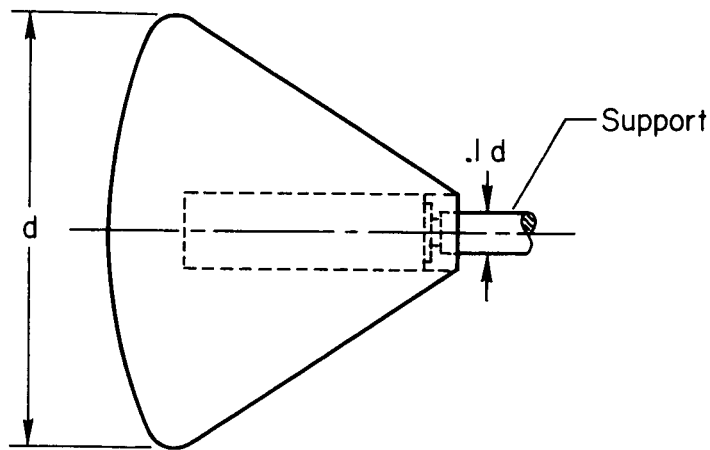
Figure 6.- Continued.



Mounting A



Mounting B

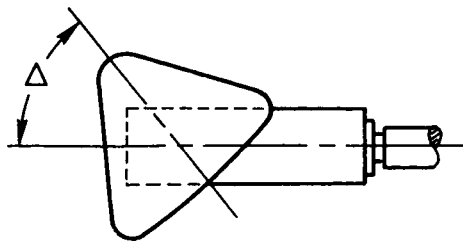


Mounting C

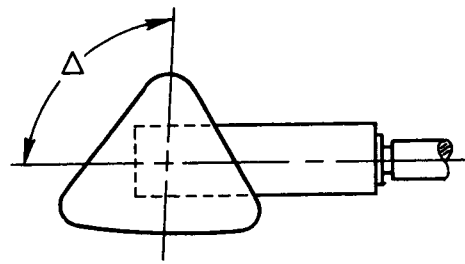
Mounting	Approx. α range	Δ , deg
A	0°-60°	30.1
B	60°-150°	119.6
C	145°-180°	180.0

(d) Mounting orientation of Apollo-type models on support; $d = 5.00$ in.

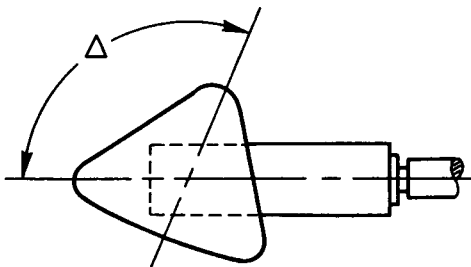
Figure 6.- Continued.



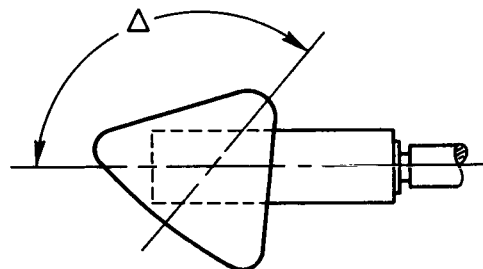
Mounting D



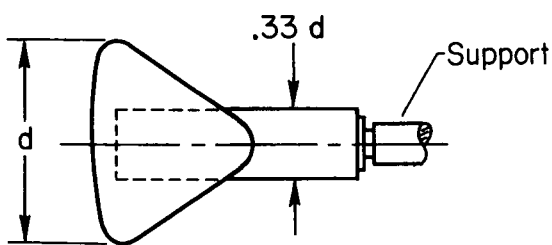
Mounting E



Mounting F



Mounting G

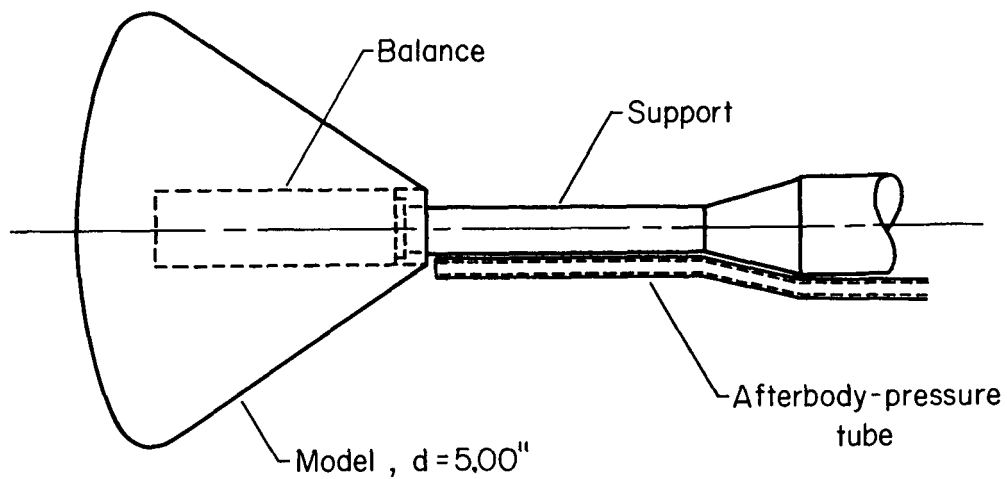


Mounting H

Mounting	Approx. α range	Δ , deg
D	37° - 60°	57.9
E	60° - 100°	80.8
F	90° - 110°	100.4
G	120° - 160°	139.3
H	180°	180.0

(e) Mounting orientation of Apollo-type models on support; $d = 2.25$ in.

Figure 6.- Continued.



(f) Afterbody-pressure measuring setup for Apollo-type model at $\alpha = 180^\circ$.

Figure 6.- Concluded.

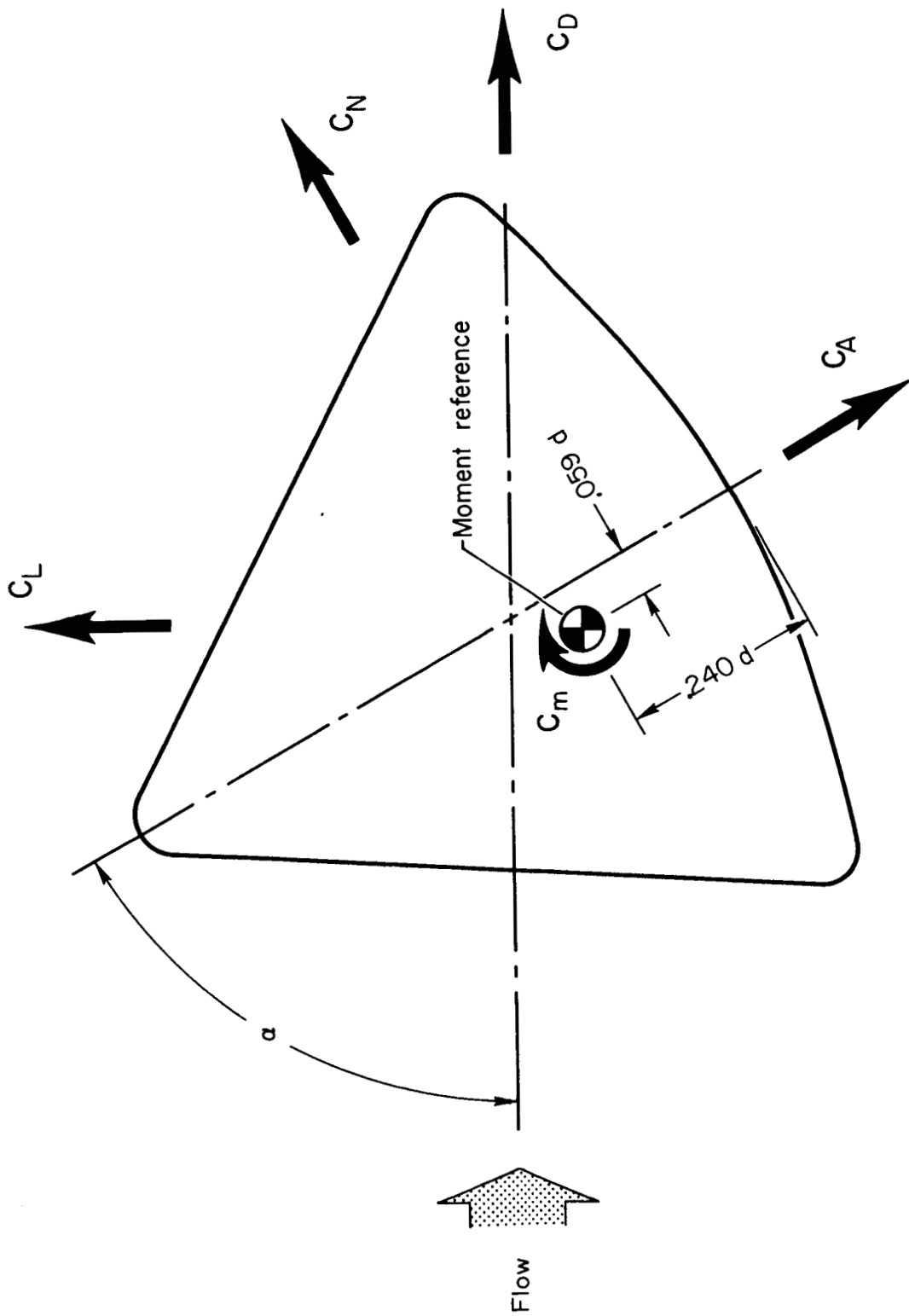
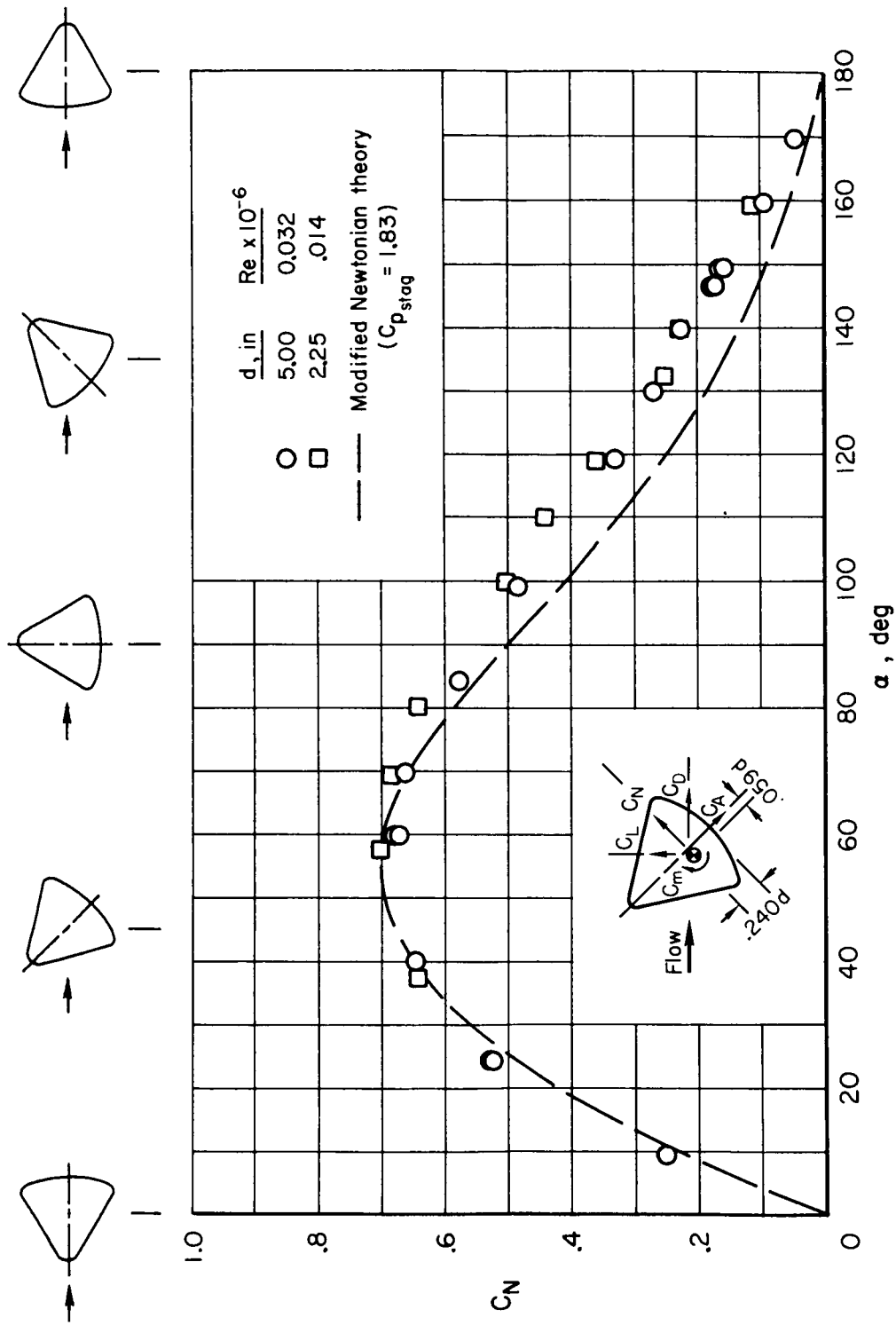
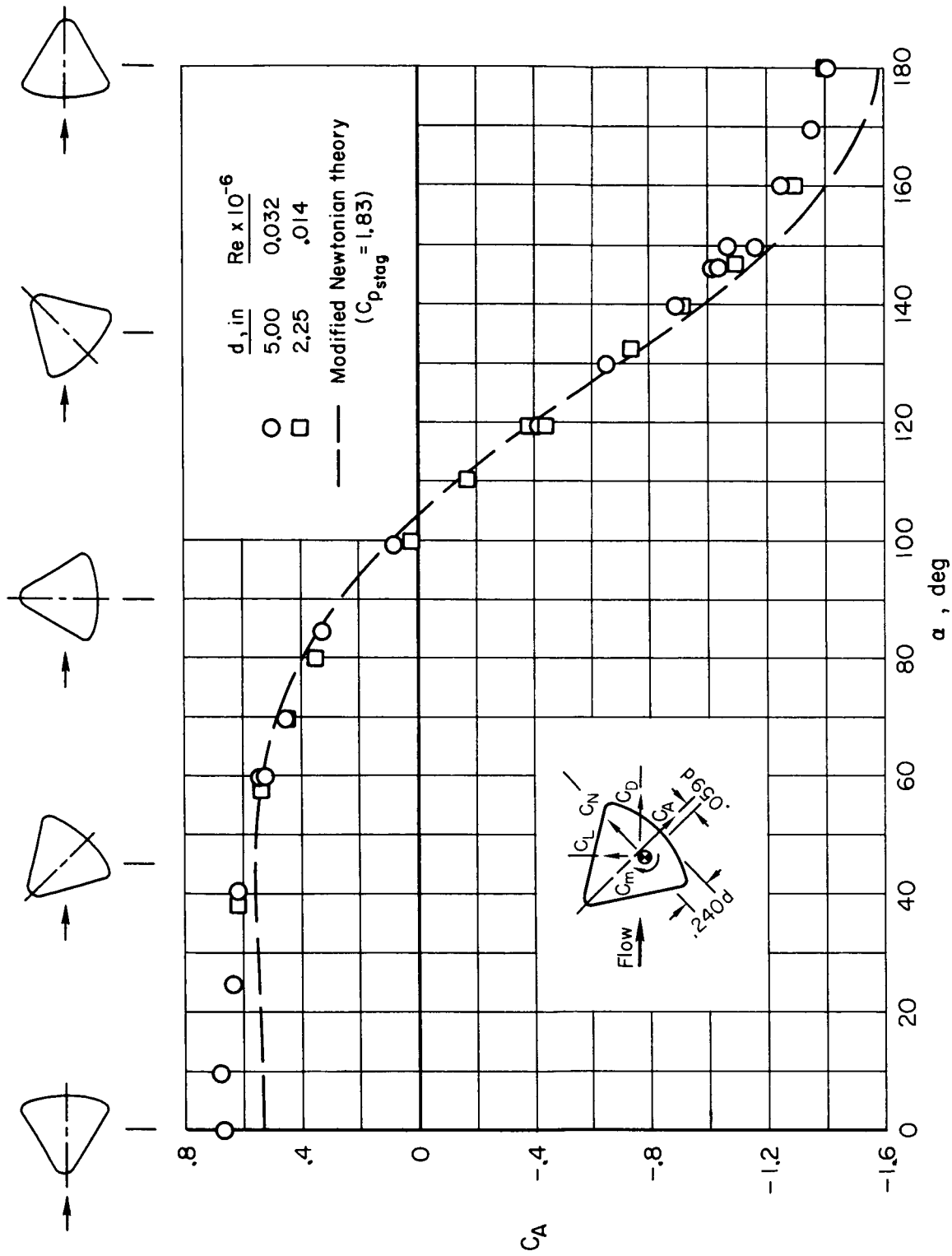


Figure 7.- Axes systems for forces and moments with positive directions indicated. (Apollo-type vehicle shown.)



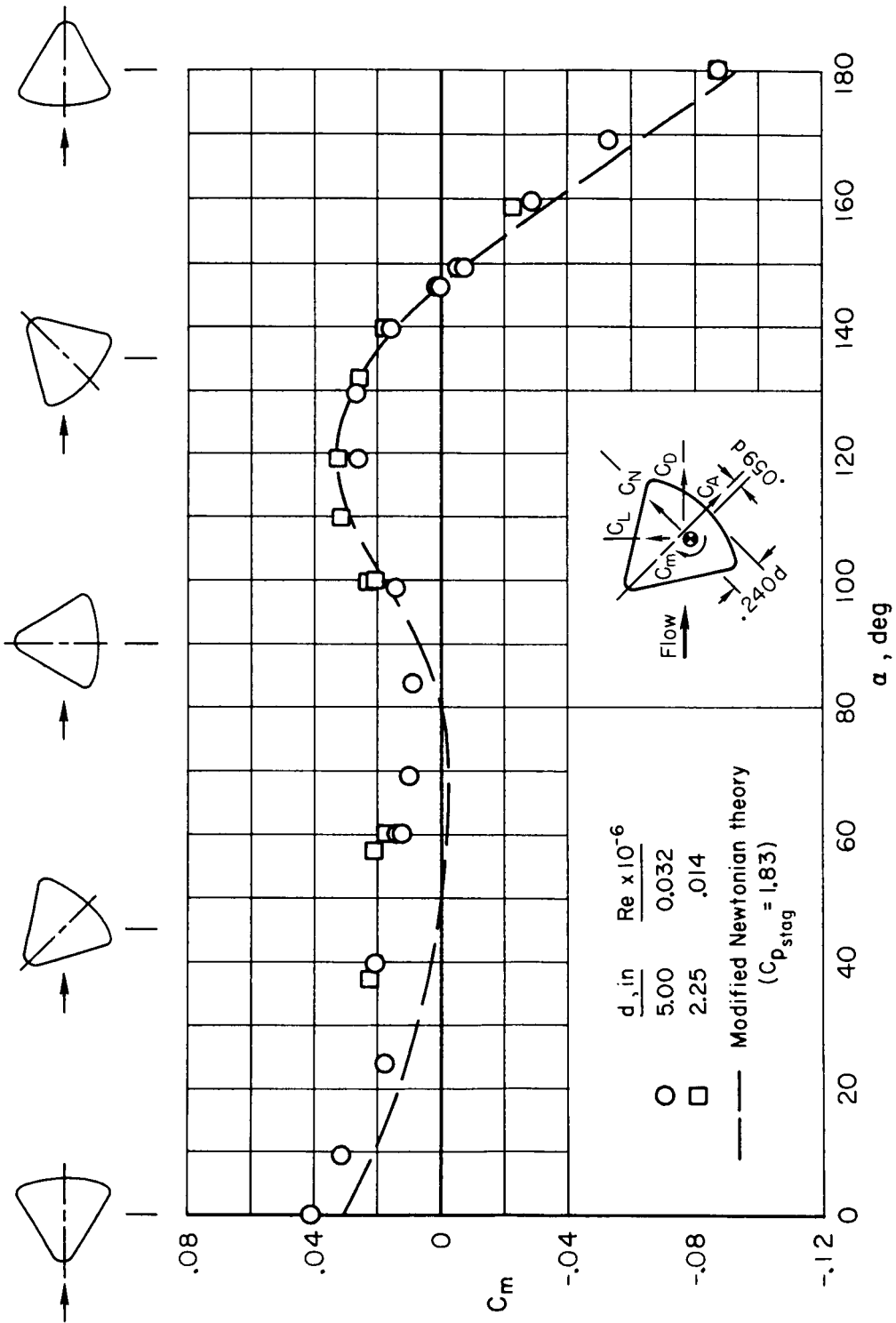
(a) C_N vs α

Figure 8.- Comparisons of theoretical and experimental aerodynamic characteristics for Apollo-type vehicle at $M_\infty = 17.2$.



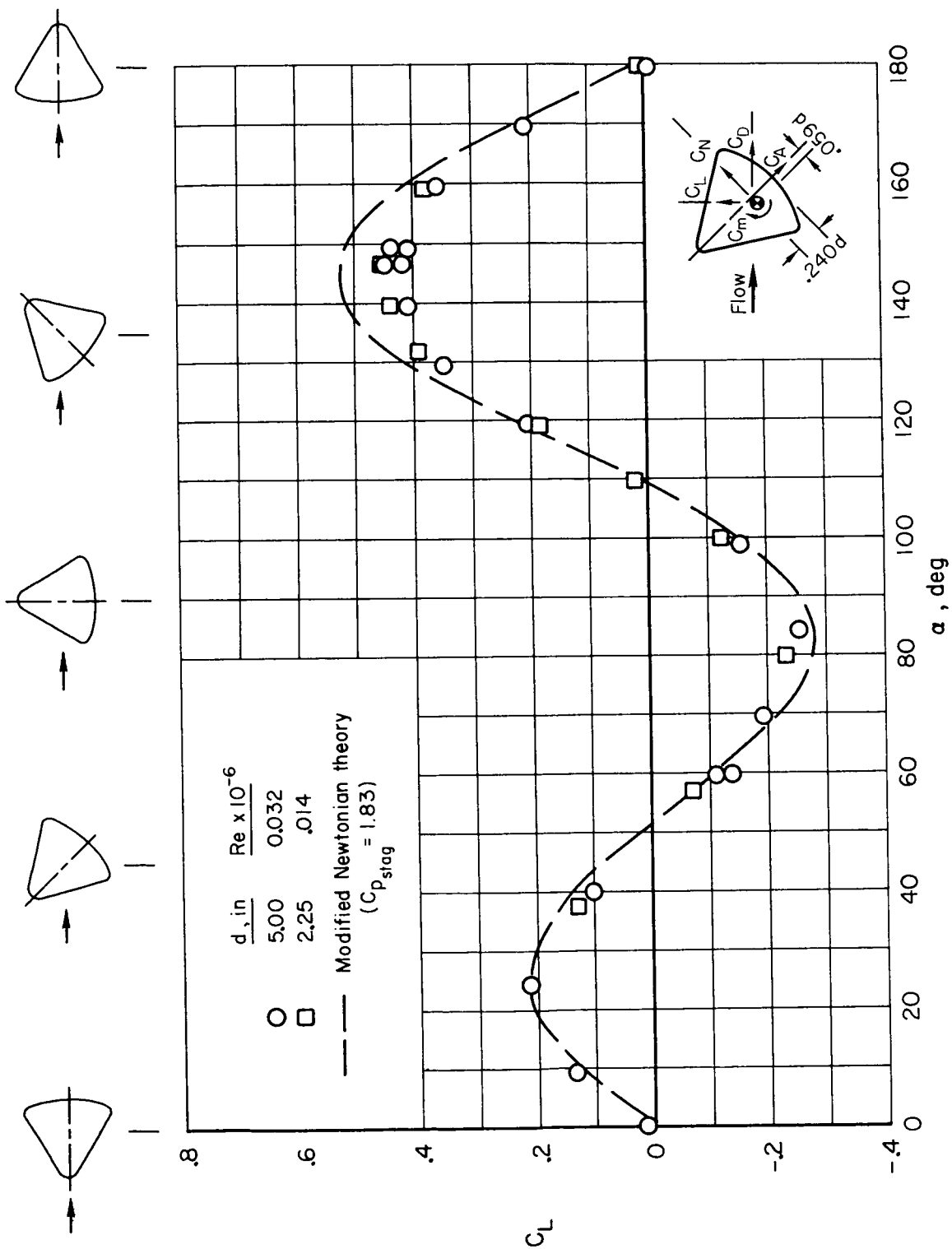
(b) C_A vs α

Figure 8.- Continued.



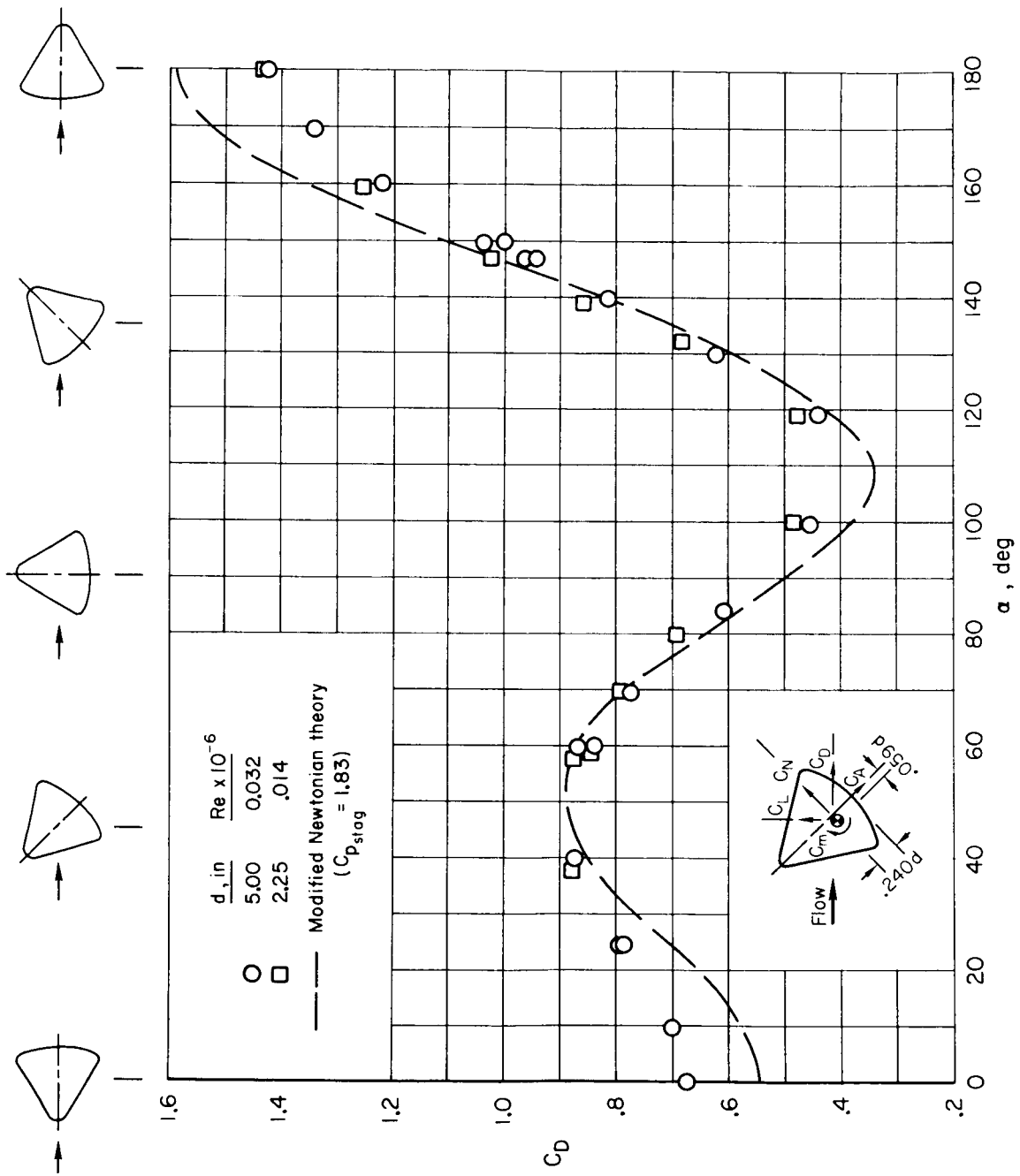
(c) C_m vs α

Figure 8.- Continued.



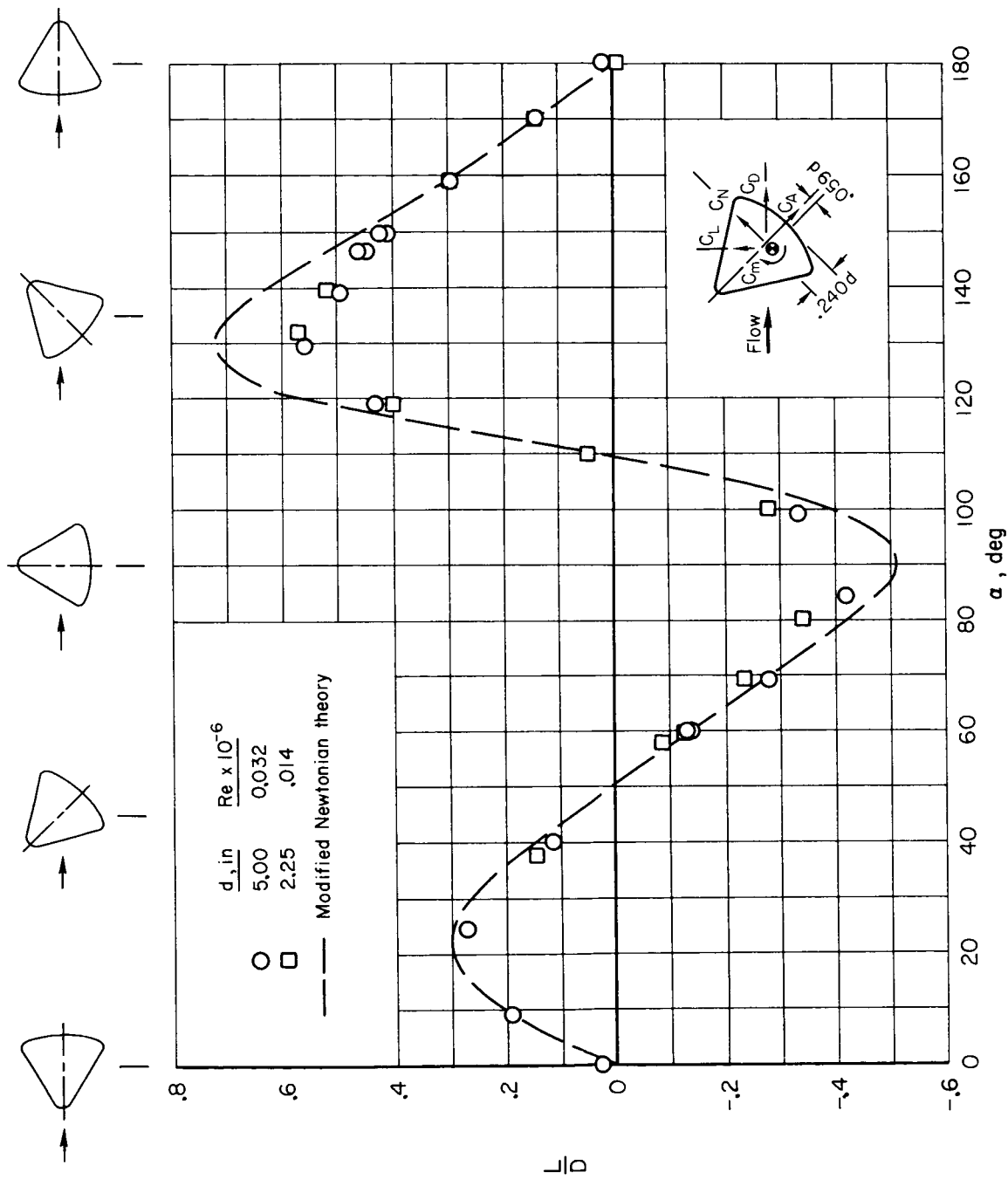
(d) C_L vs α

Figure 8.- Continued.



(e) C_D vs α

Figure 8.- Continued.



(f) L/D vs α

Figure 8.- Continued.

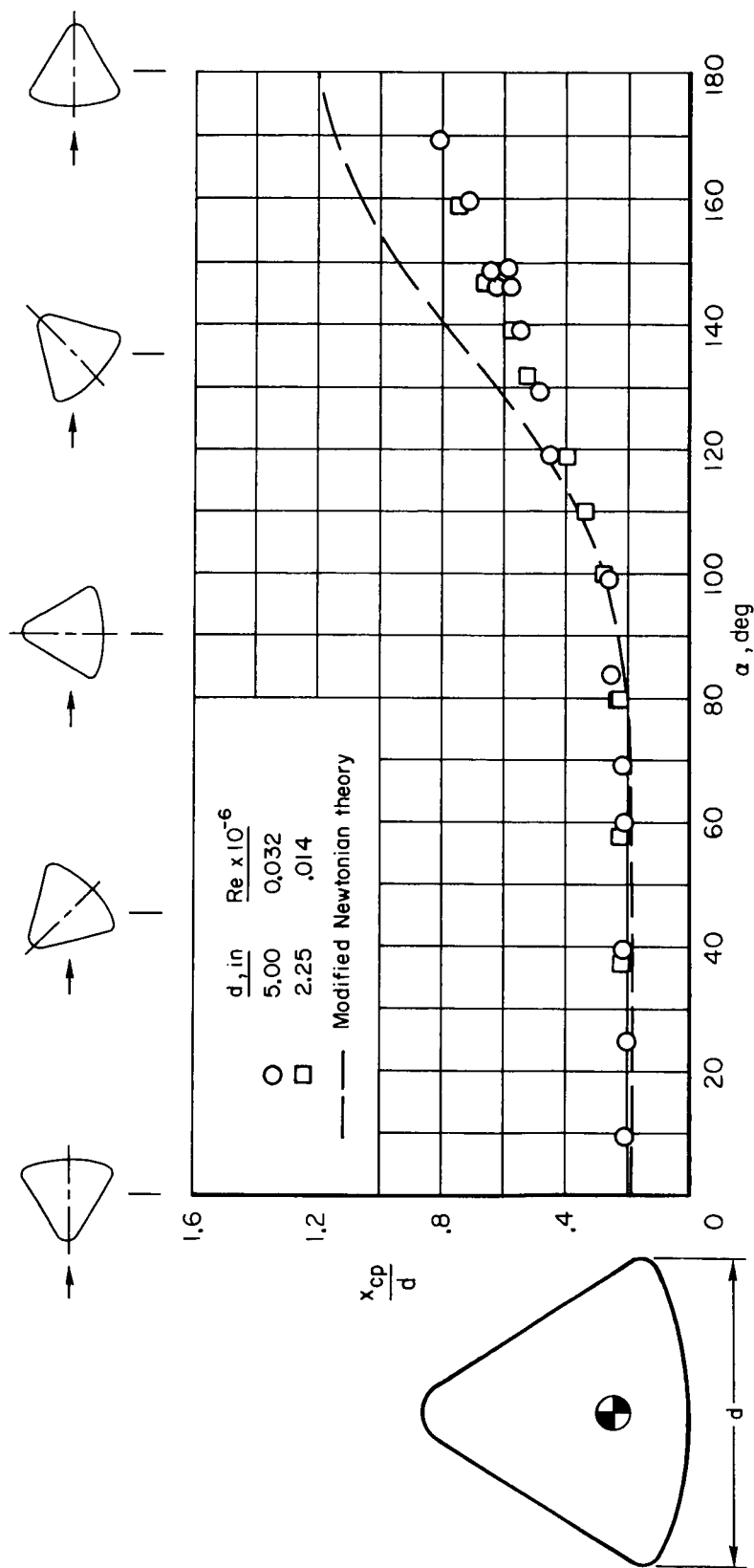
(g) x_{cp}/d vs α

Figure 8.- Concluded.

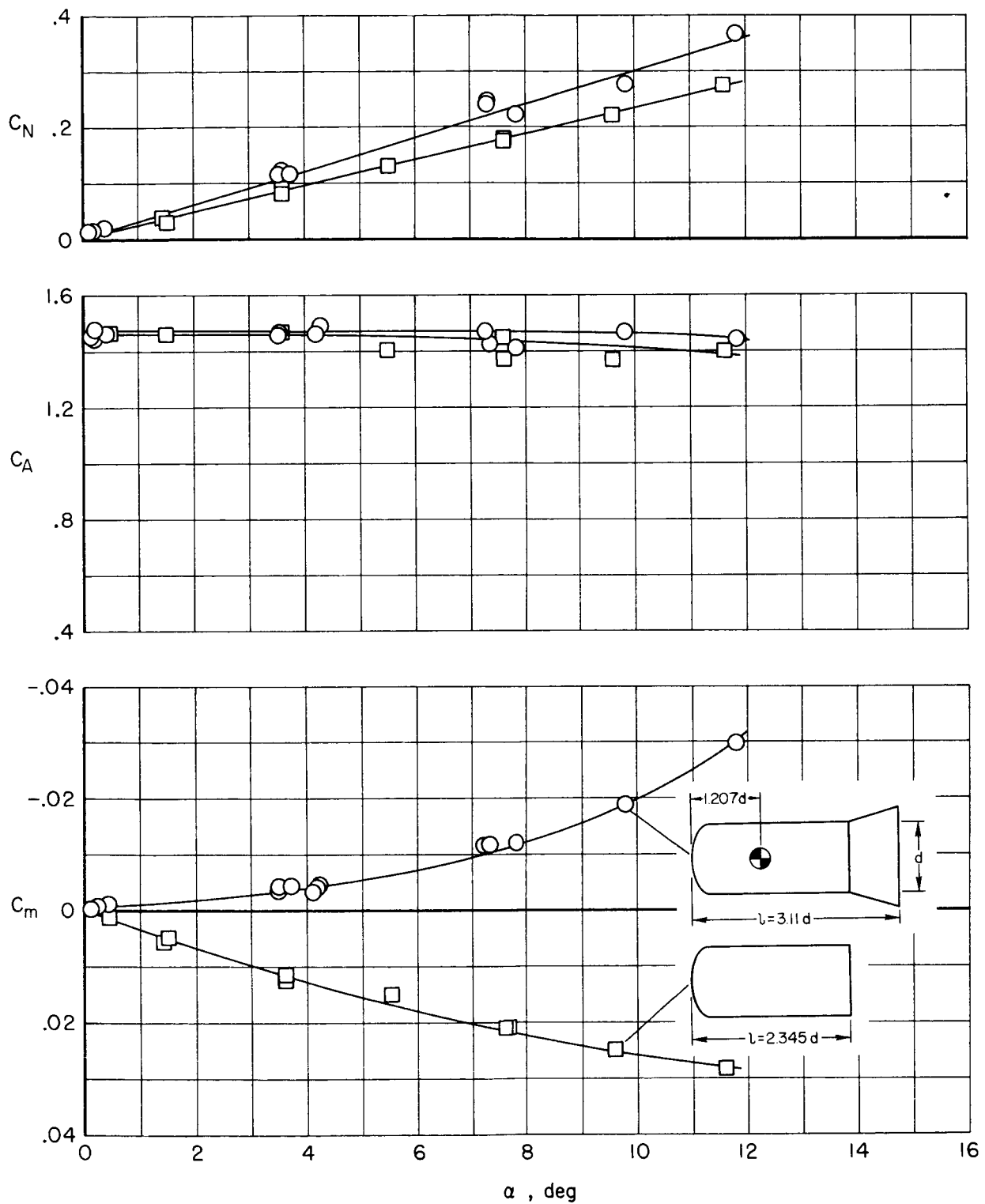
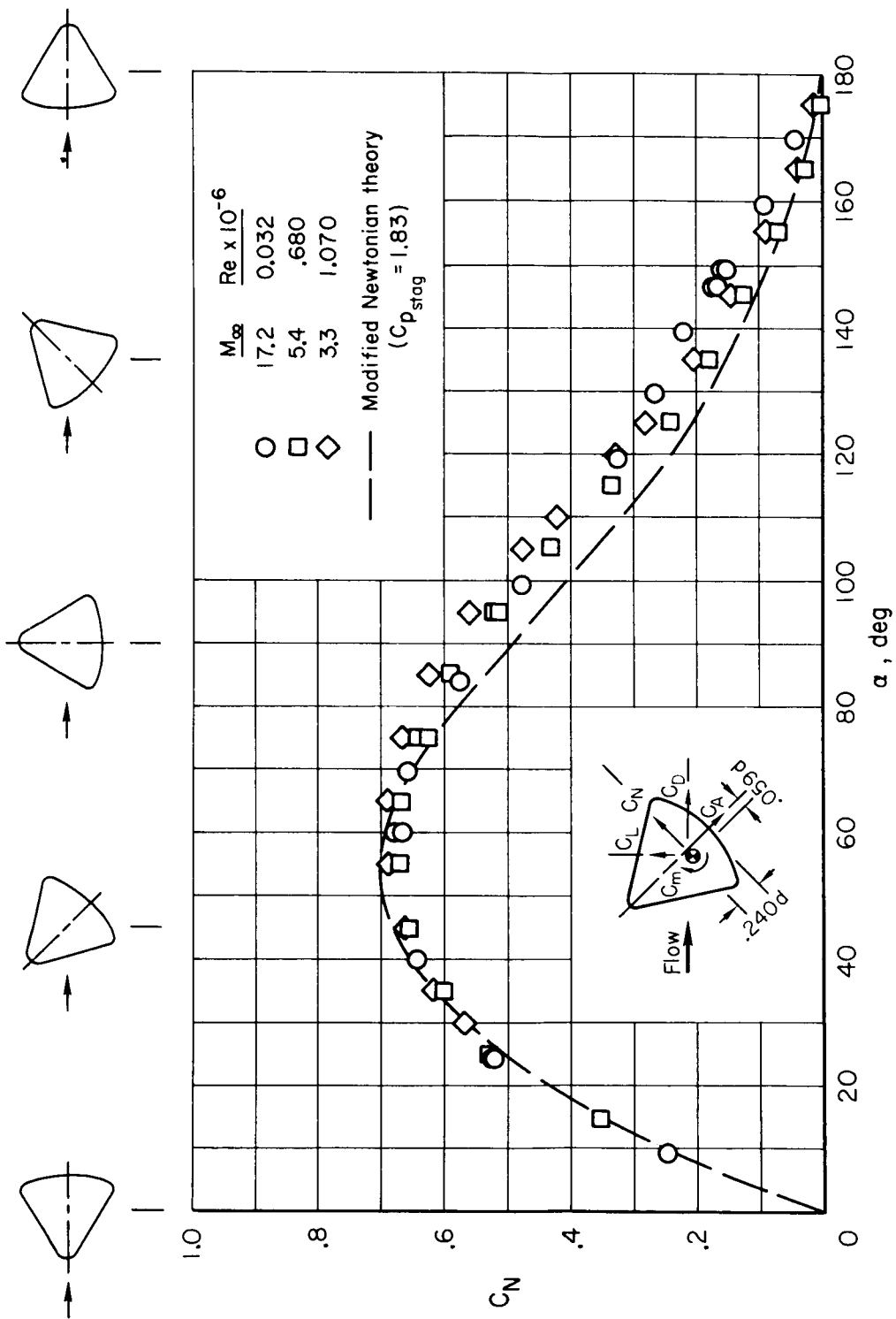
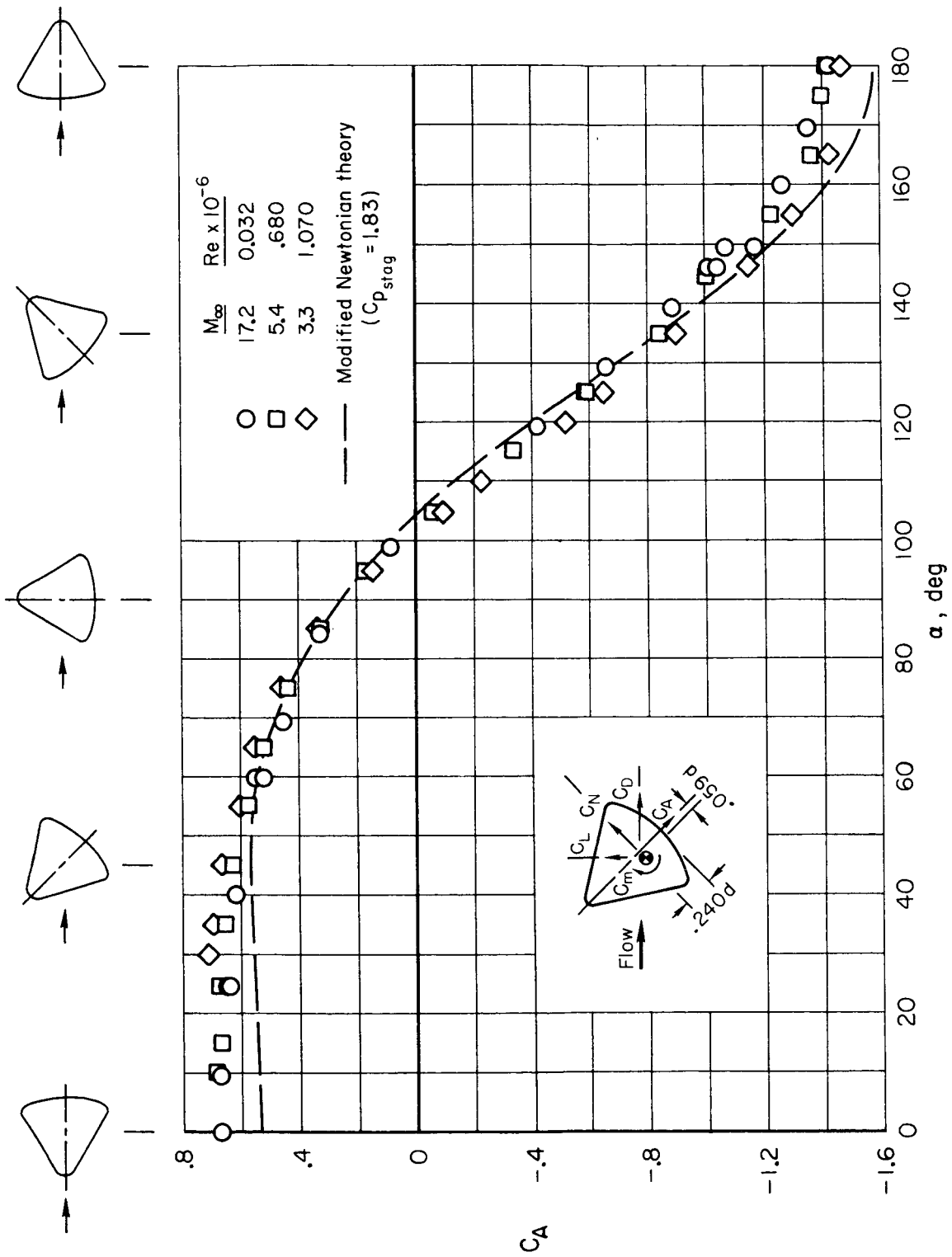


Figure 9.- Experimental aerodynamic coefficients for the Polaris-type vehicle with and without an afterbody flare at $M_\infty = 17.2$.



(a) C_N vs α

Figure 10.- Comparisons of aerodynamic characteristics for Apollo-type vehicle at supersonic and hypersonic Mach numbers.



(b) C_A vs α

Figure 10.- Continued.

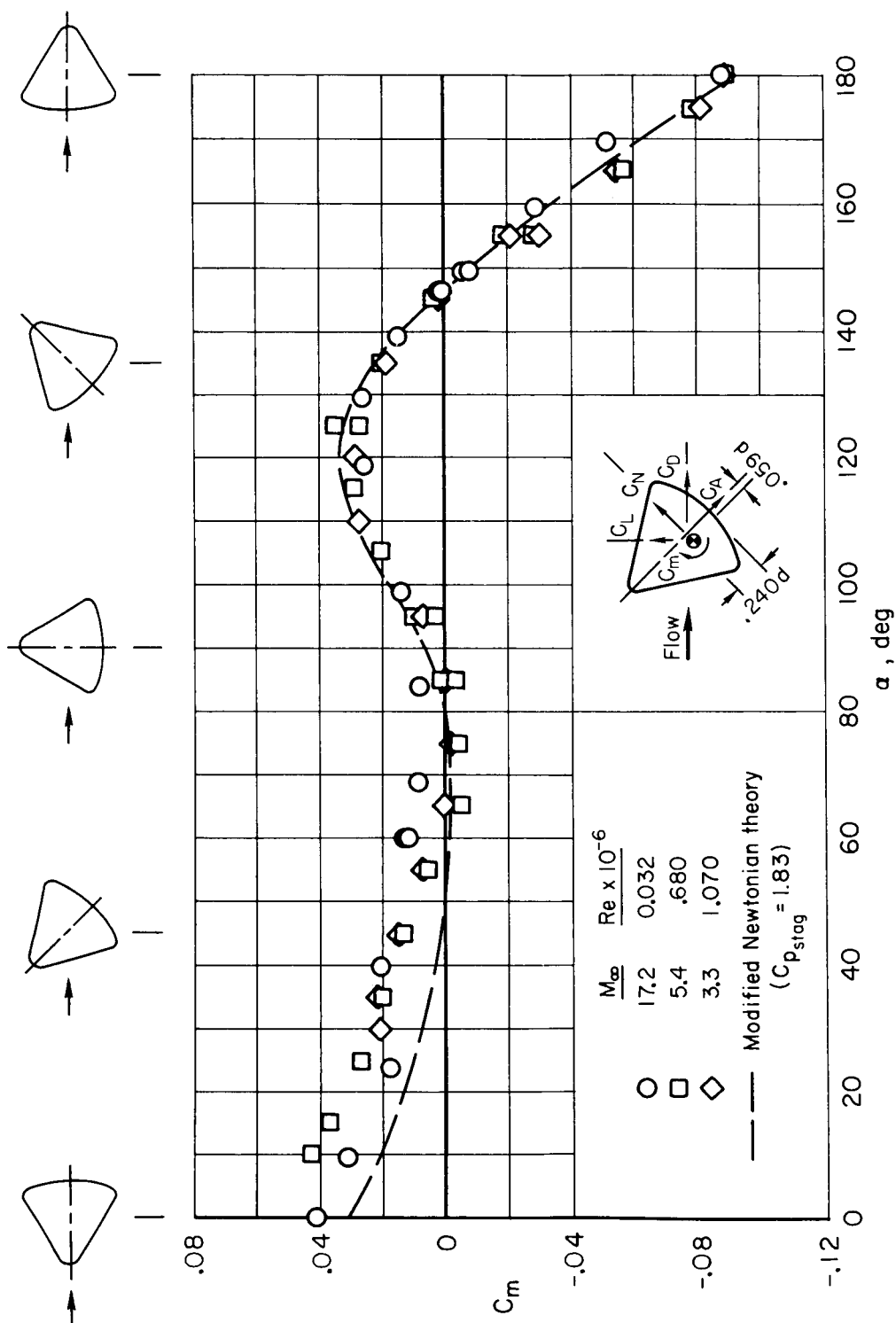
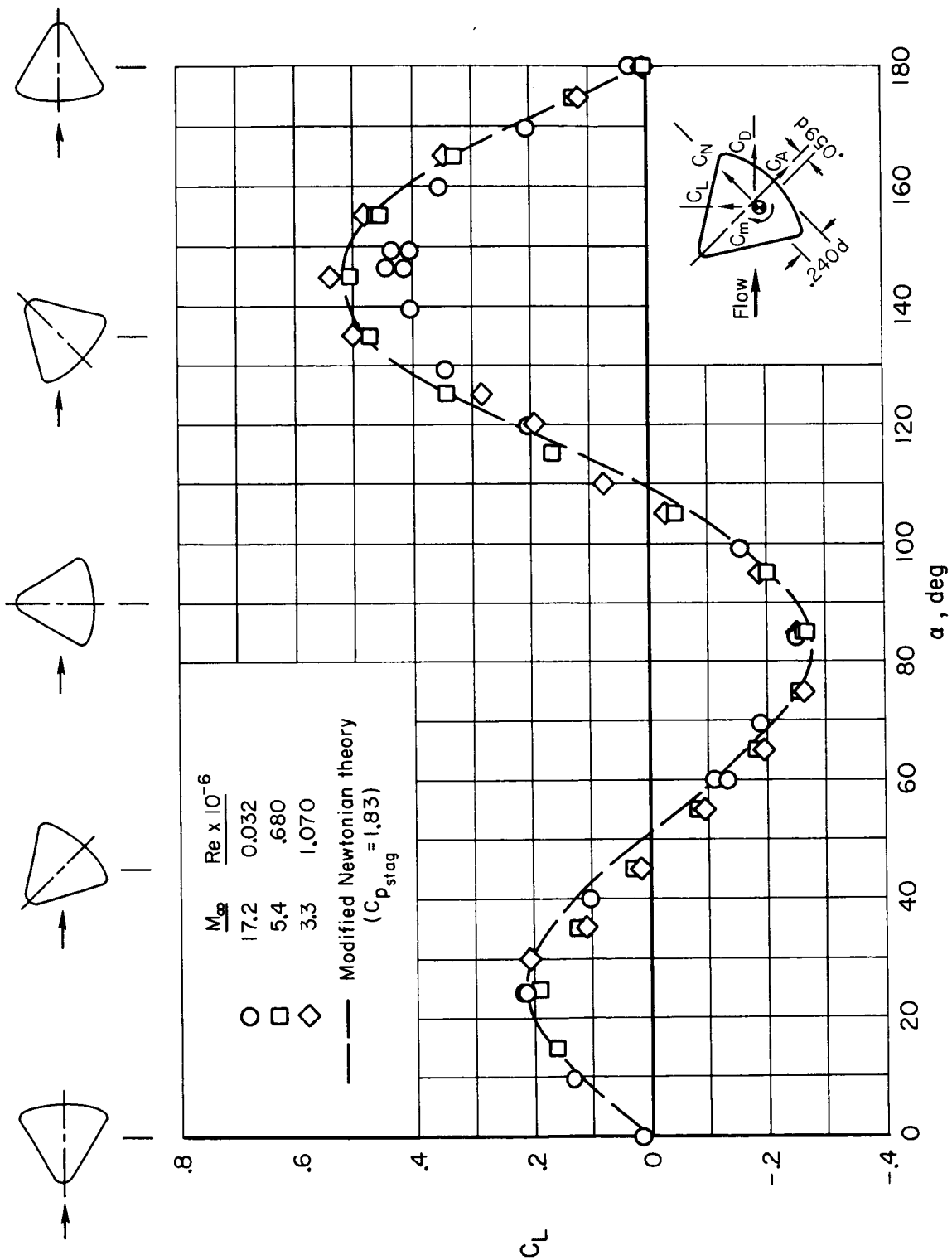
(c) C_m vs α

Figure 10.- Continued.



(d) C_L vs α

Figure 10.- Continued.

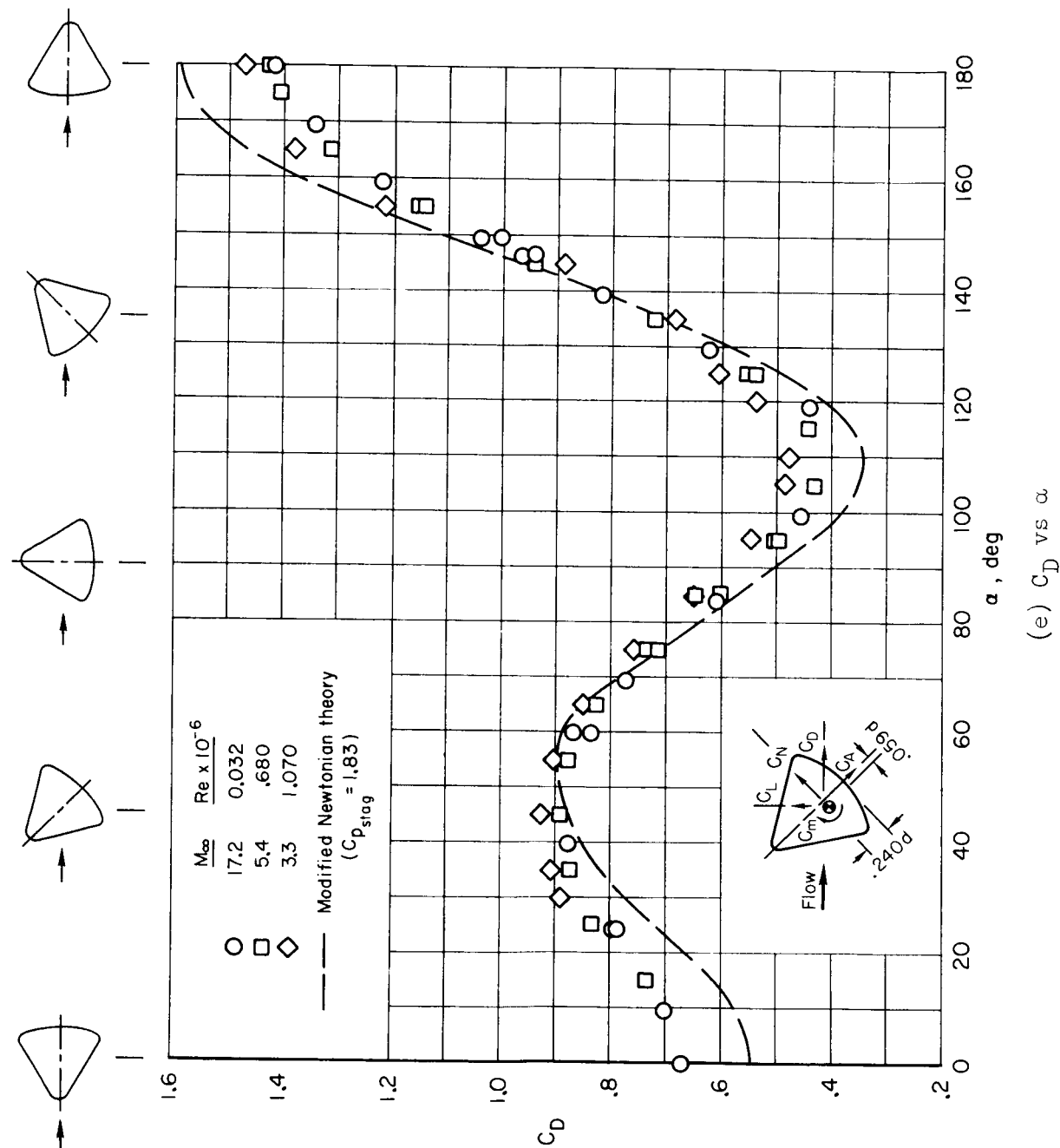
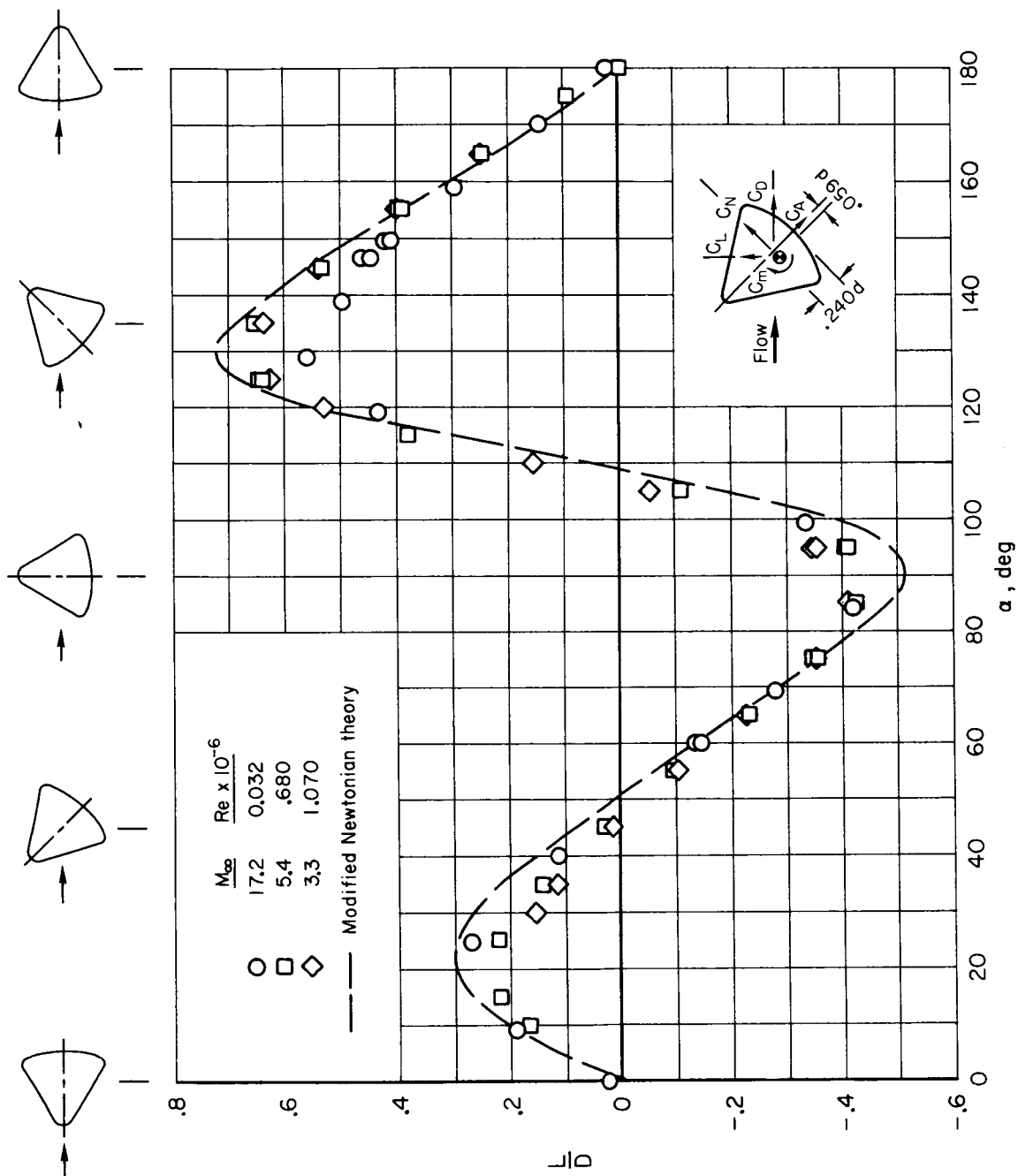


Figure 10.- Continued.



(f) L/D vs α

Figure 10.- Continued.

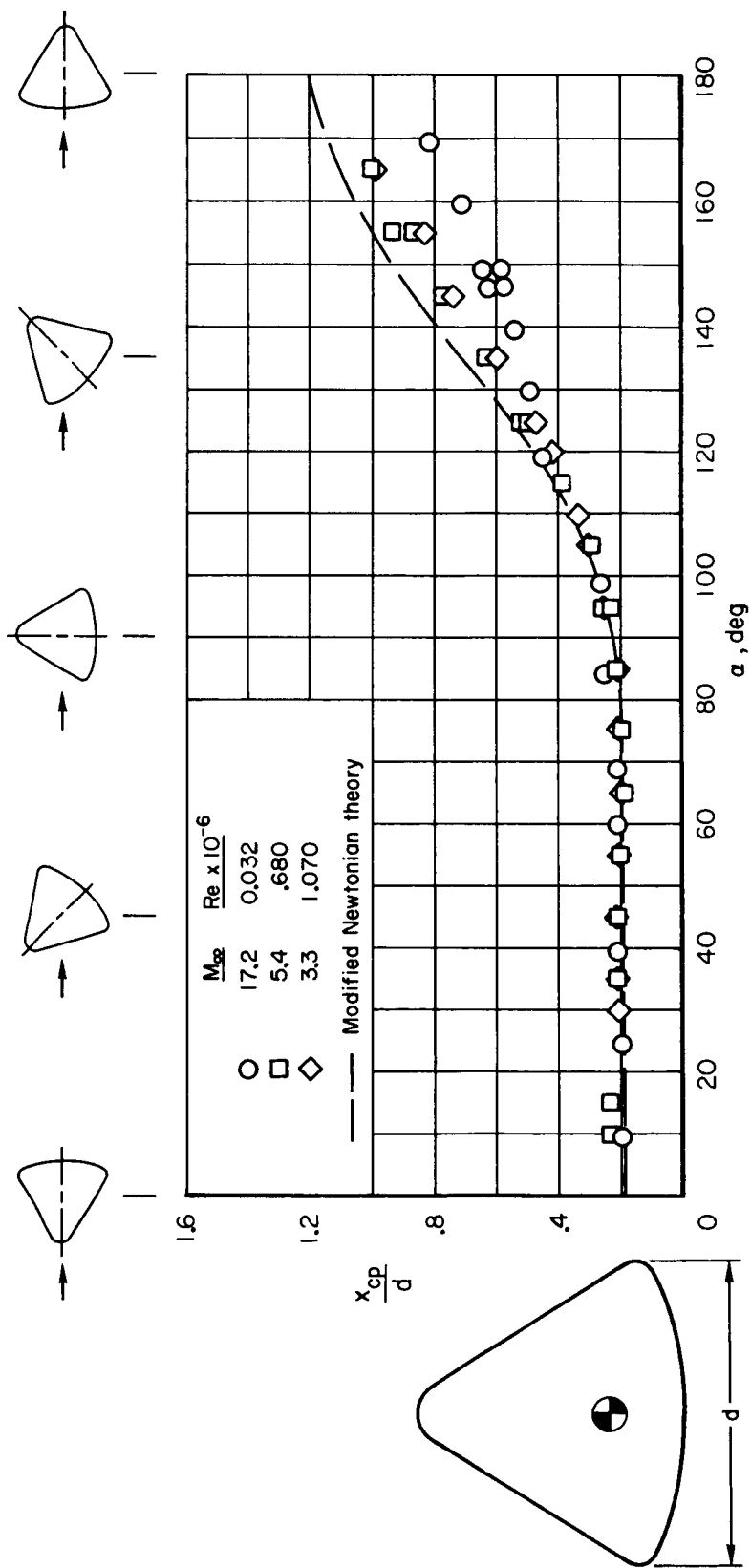
(g) x_{cp}/d vs α

Figure 10.- Concluded.

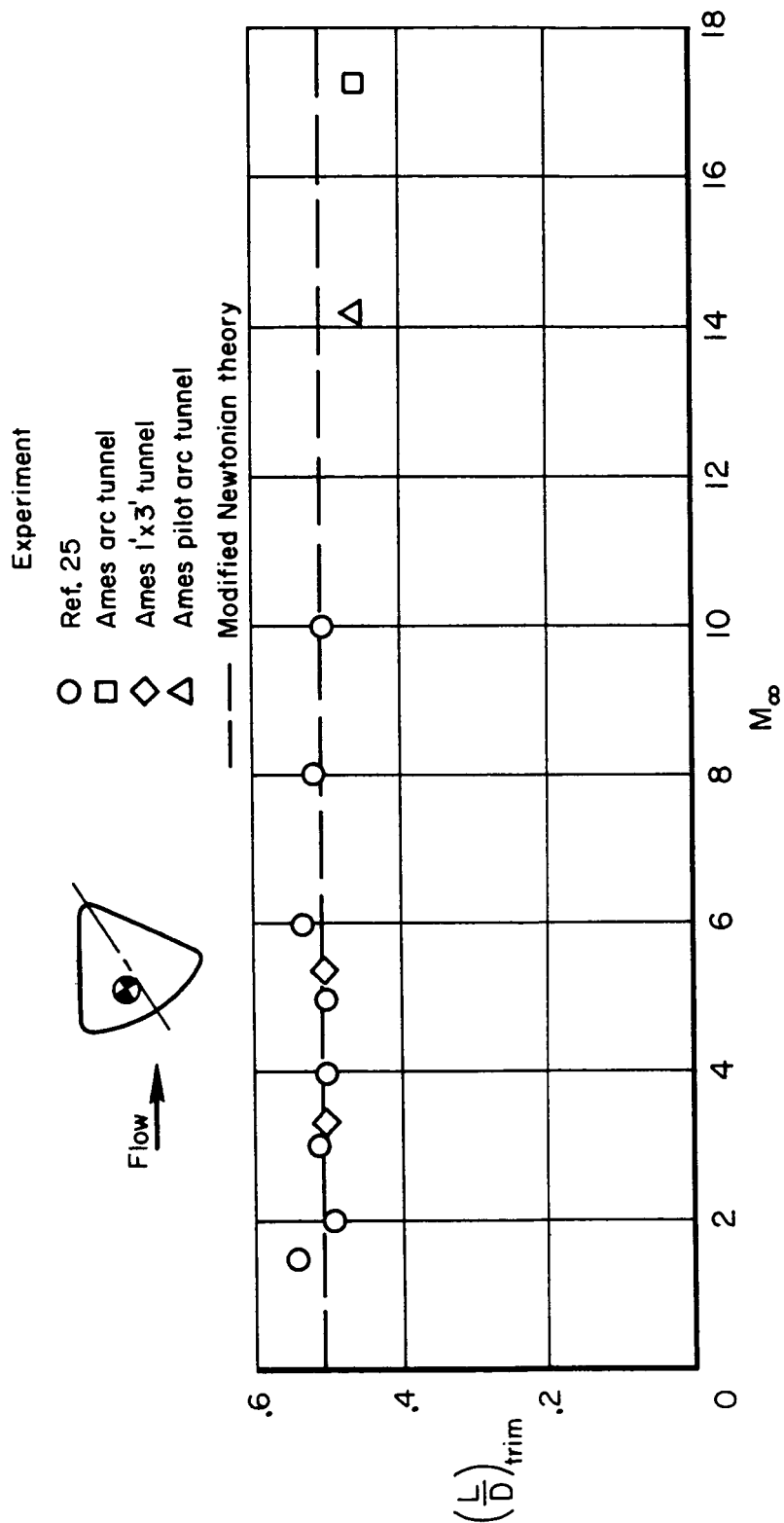


Figure 11.- Effect of Mach number on lift-drag ratio for the Apollo-type vehicle at $\alpha = 14.7^\circ$ (trim condition).

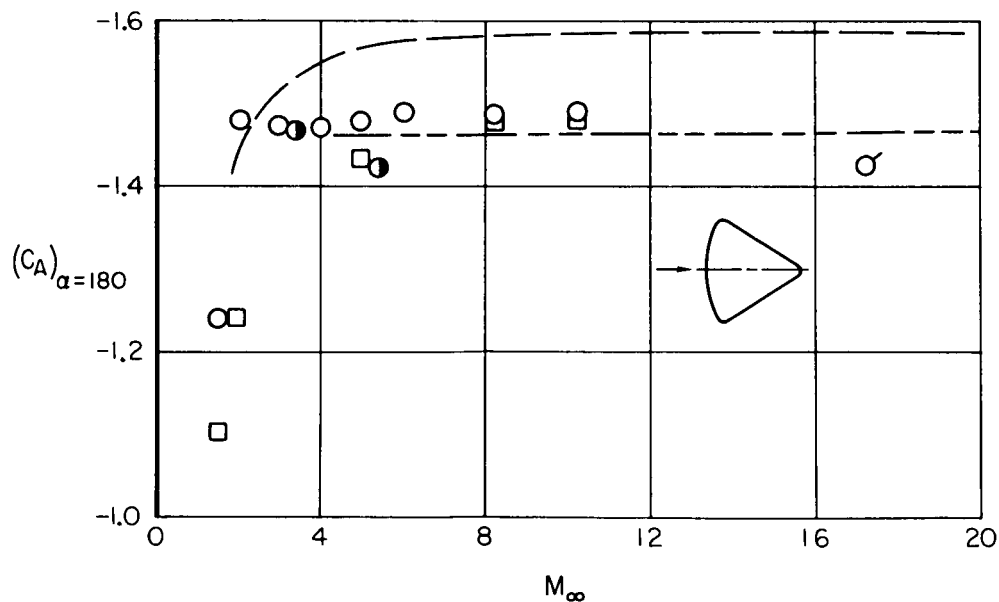
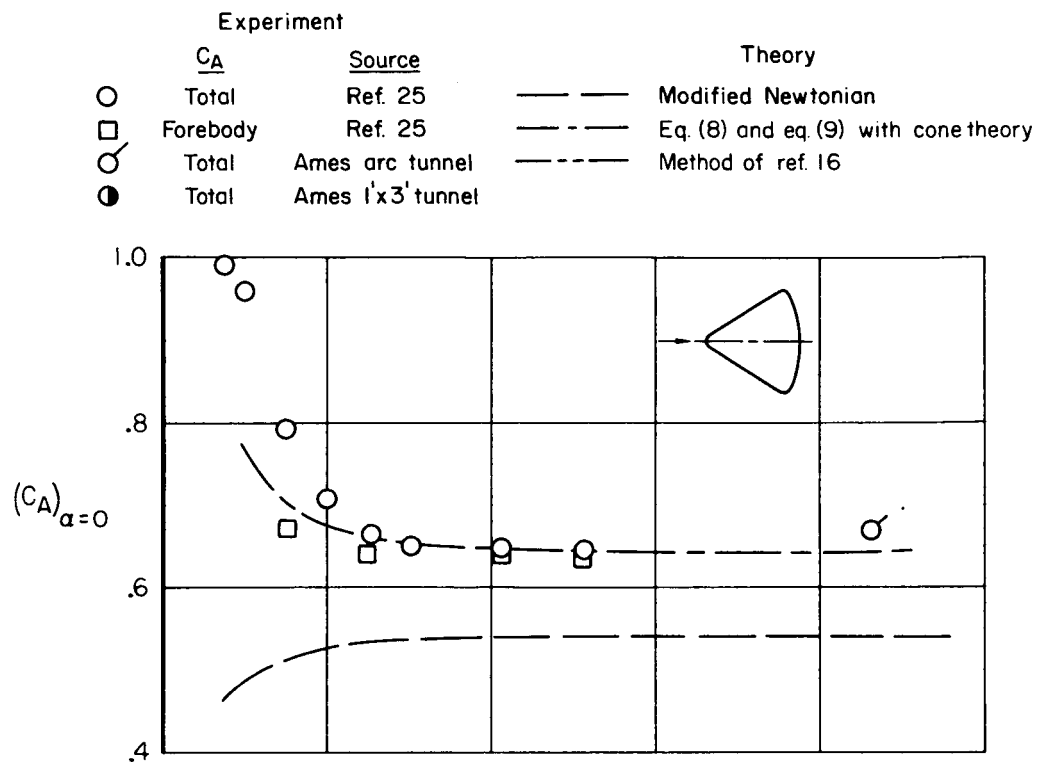


Figure 12.- Variation of axial-force coefficients with Mach number for Apollo-type vehicle at $\alpha = 0^\circ$ and 180° .

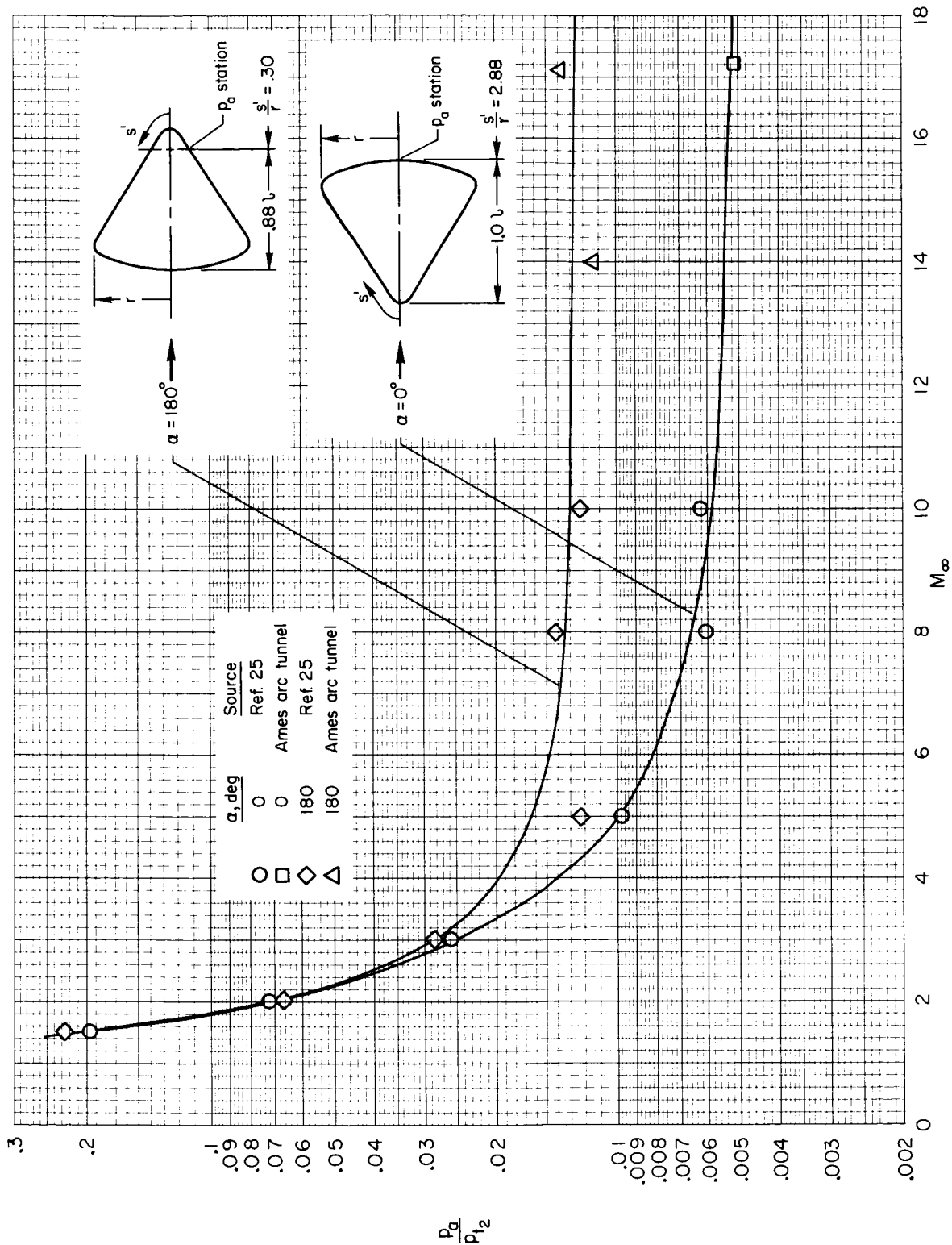


Figure 13.- Variation of afterbody pressures with Mach number for Apollo-type vehicle at $\alpha = 0^\circ$ and 180° .

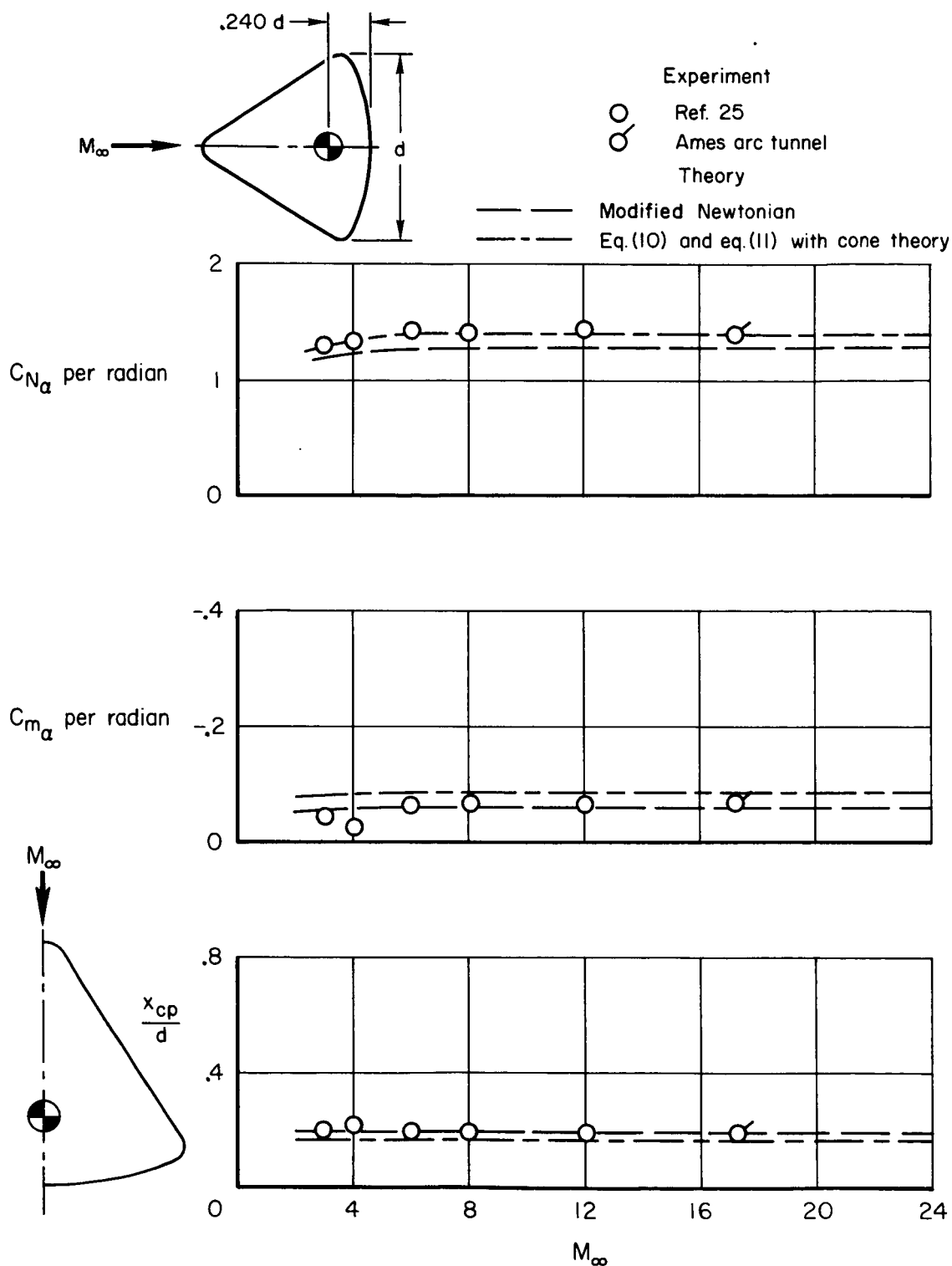


Figure 14.- Variation of C_{N_α} , C_{m_α} , and x_{cp}/d with Mach number for Apollo-type vehicle at $\alpha = 0^\circ$.

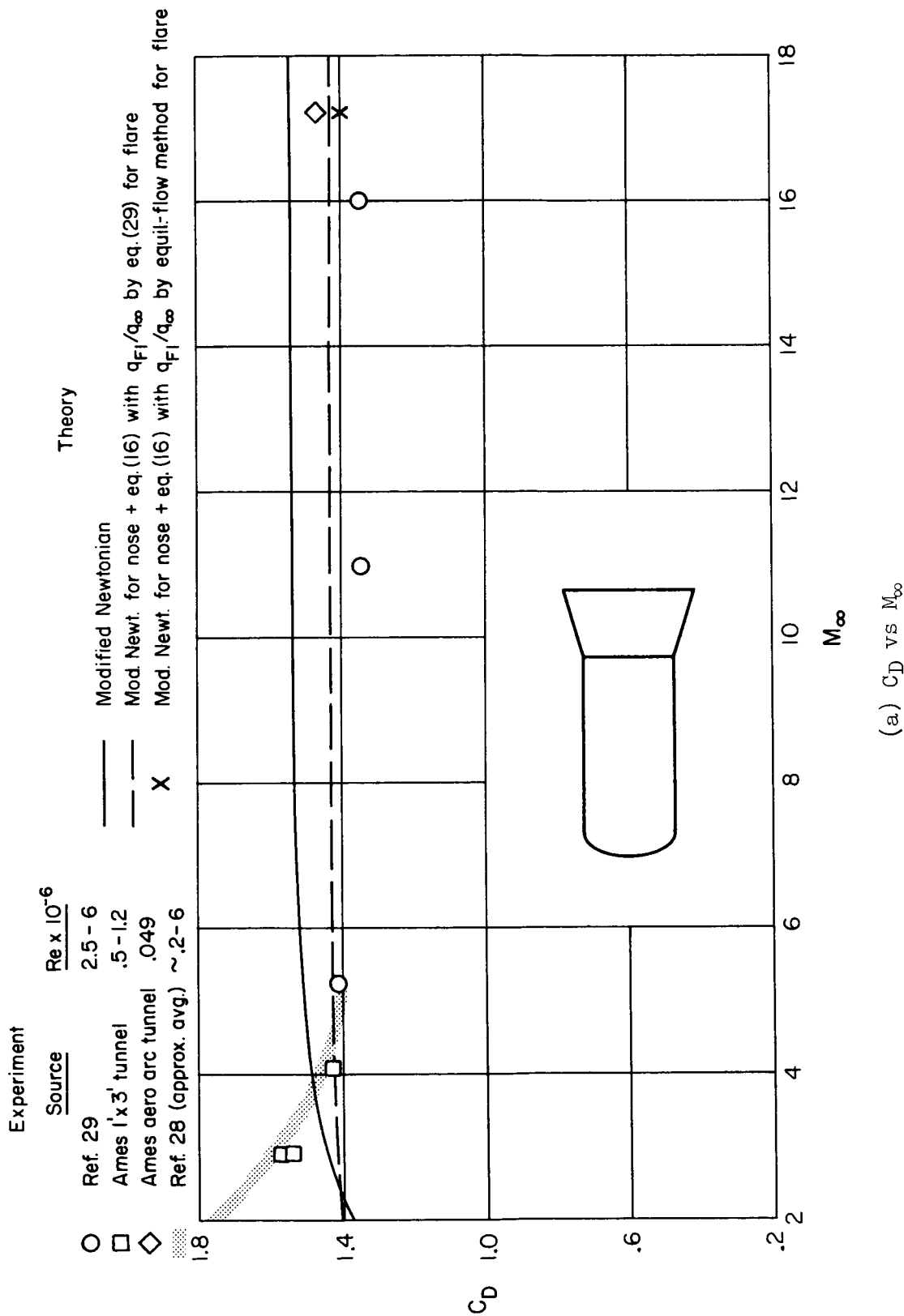
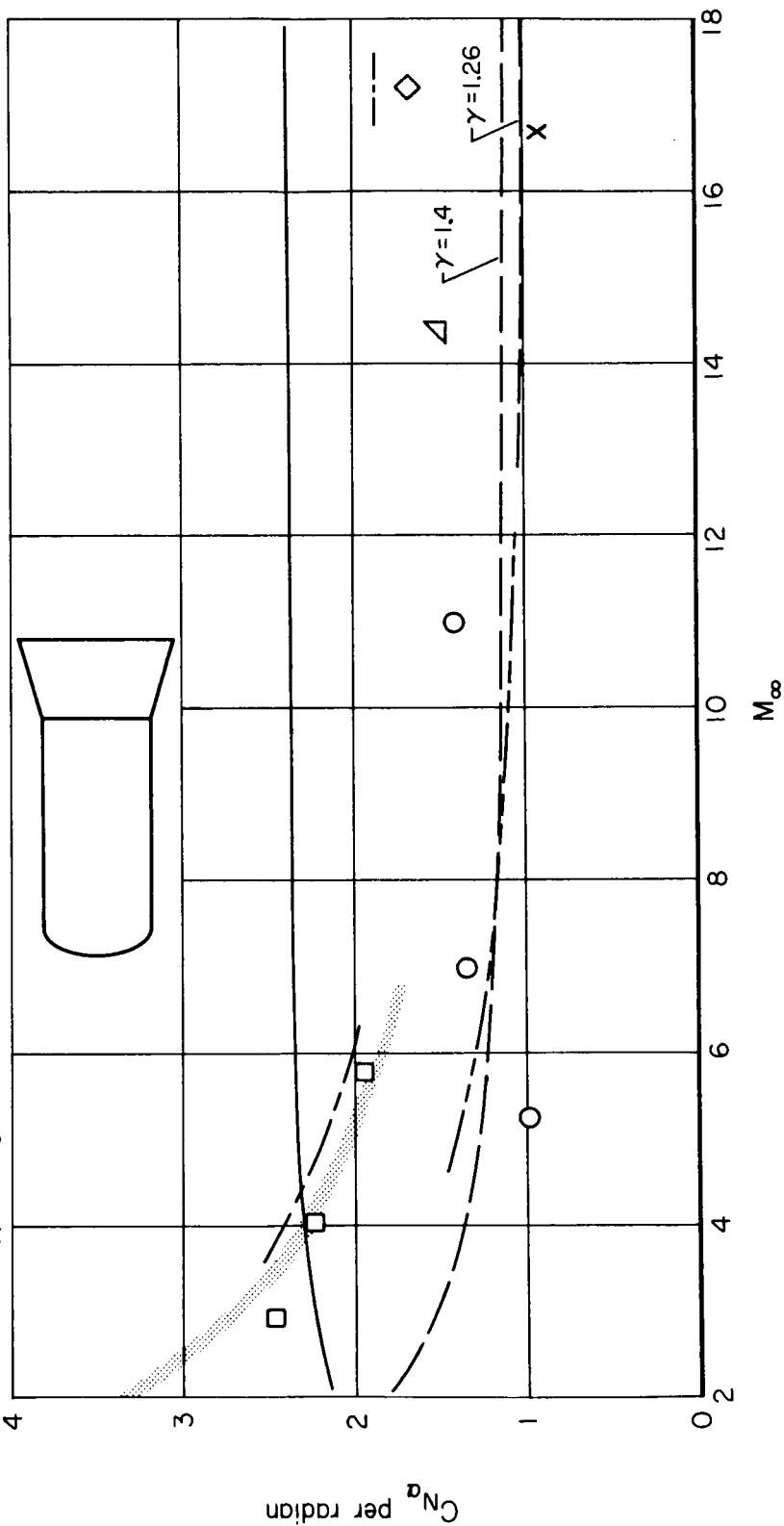


Figure 15.- Comparisons of calculated with experimental aerodynamic characteristics for Polaris-type vehicle at $\alpha = 0^\circ$. (Theory includes only nose and flare contributions.)

Experiment		Re x 10 ⁻⁶
Source		
Ref. 29	2.5 - 6	
Ames 1' x 3' tunnel	.5 - 1.2	
Ames pilot arc tunnel	.058	
Ames aero arc tunnel	.049	
Ref. 28 (approx. avg.)	~2-6	

Theory

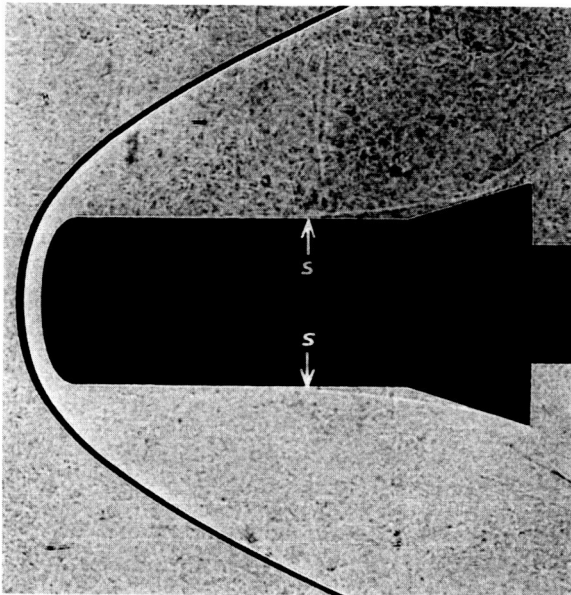
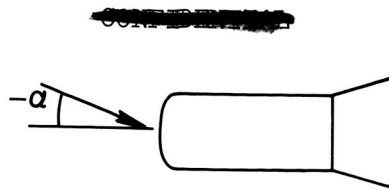
	Modified Newtonian
—	Mod. Newt. for nose + eq. (15) with q_{F1}/q_{∞} by eq. (29) for flare
---	Mod. Newt. for nose + eq. (15) with q_{F1}/q_{∞} by equil-flow method for flare
X	Experiment for body + eq. (15) with q_{F1}/q_{∞} by eq. (29) for flare
---	Mod. Newt. for nose + method of refs. 17 and 19 for flare



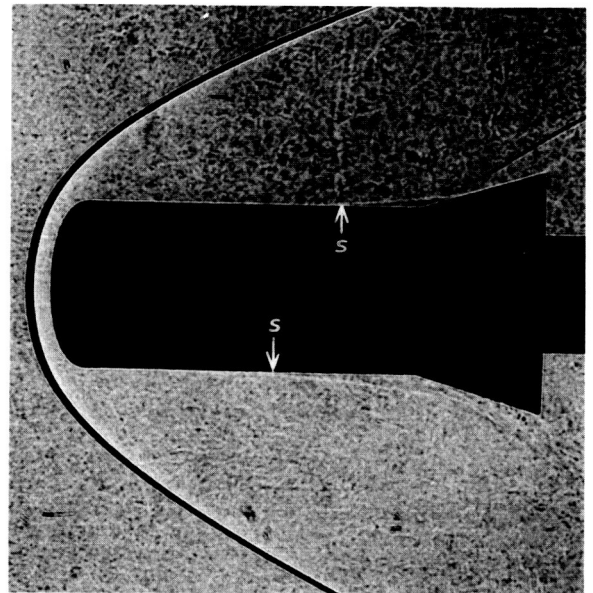
(b) C_{Na} vs M_{∞}
Figure 15.- Continued.



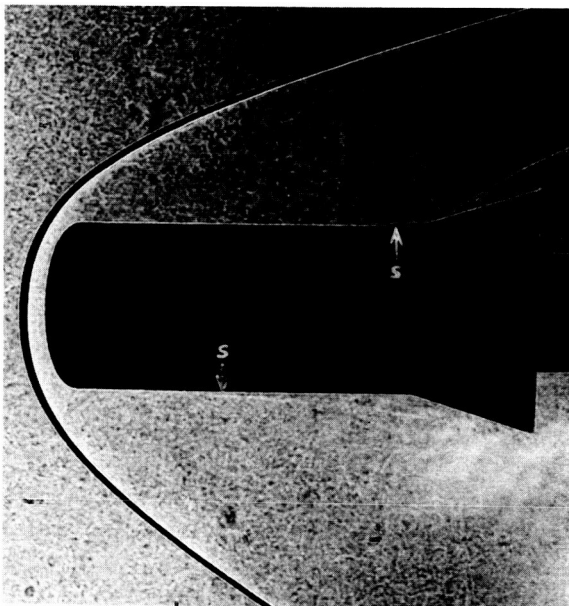
Figure 15.- Concluded.



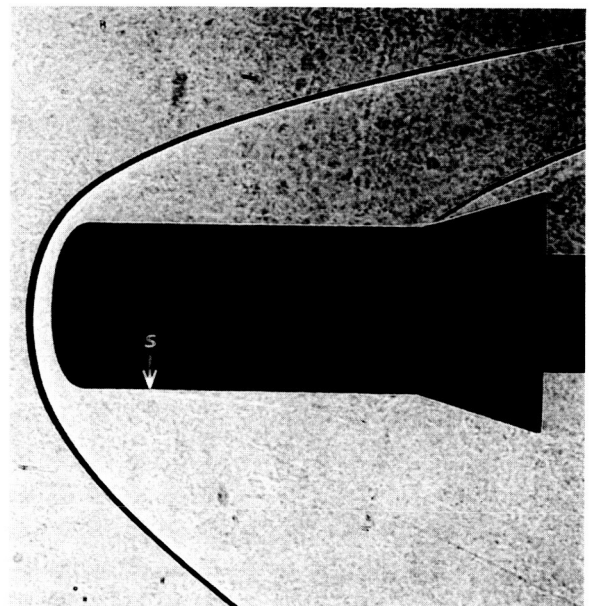
$\alpha = 0^\circ$



$\alpha = -2^\circ$

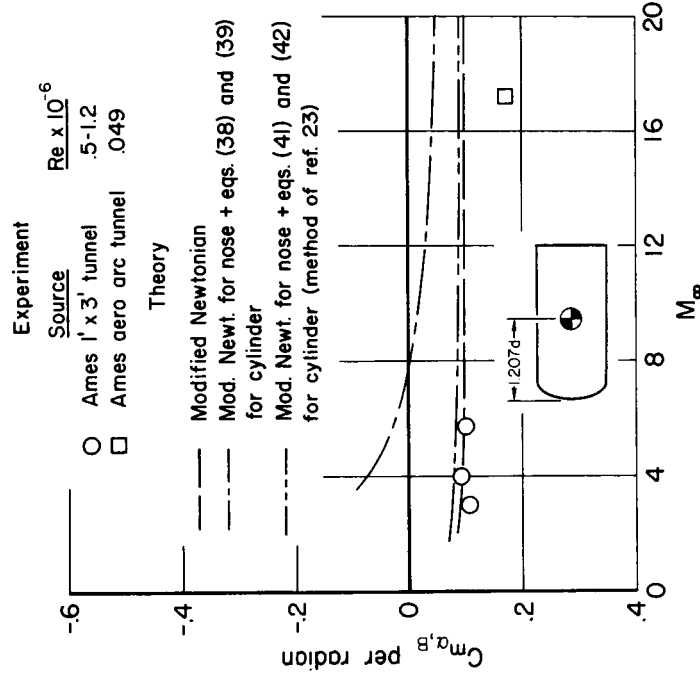
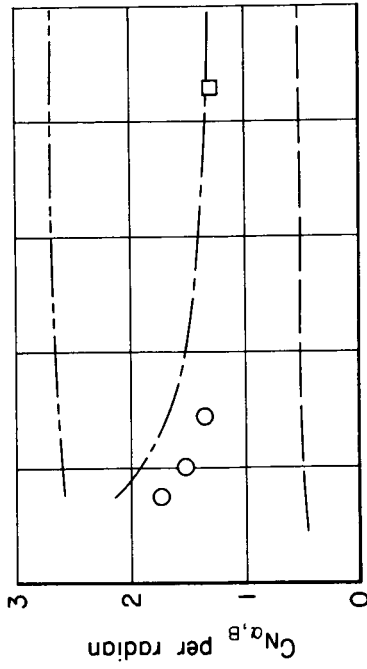


$\alpha = -6^\circ$

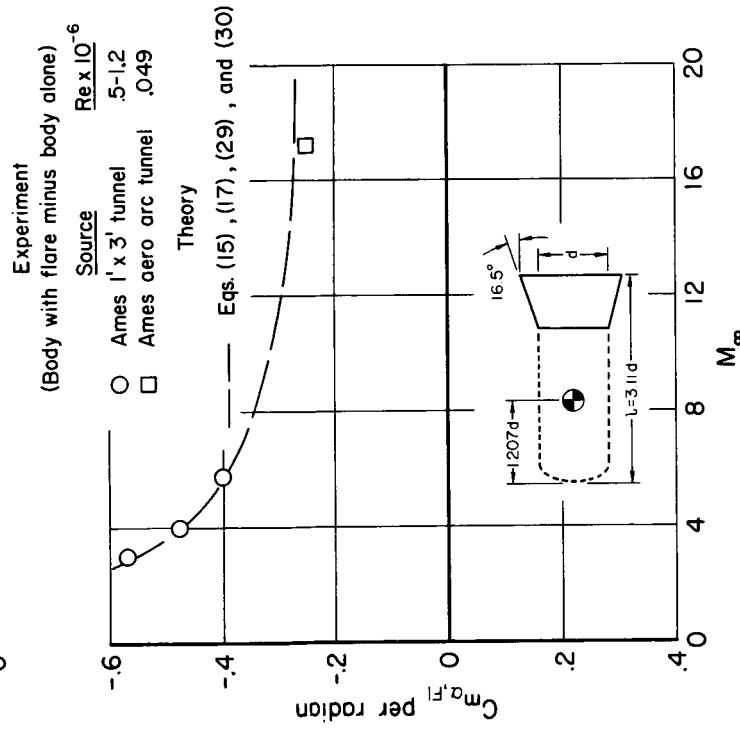
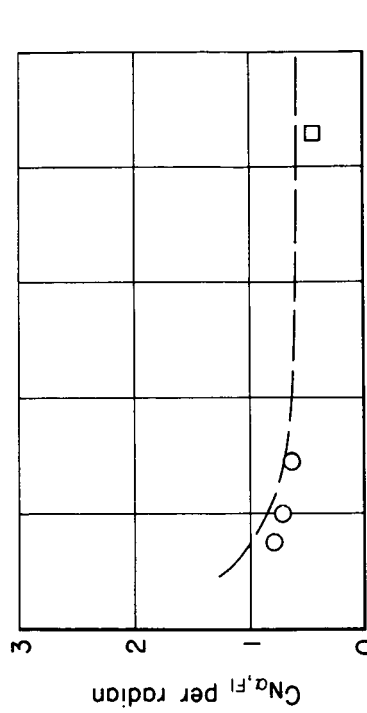


$\alpha = -10^\circ$

Figure 16.- Typical shadowgraph pictures of the flow over the Polaris configuration at $M_\infty \simeq 4.1$ and $Re \simeq 1 \times 10^6$.

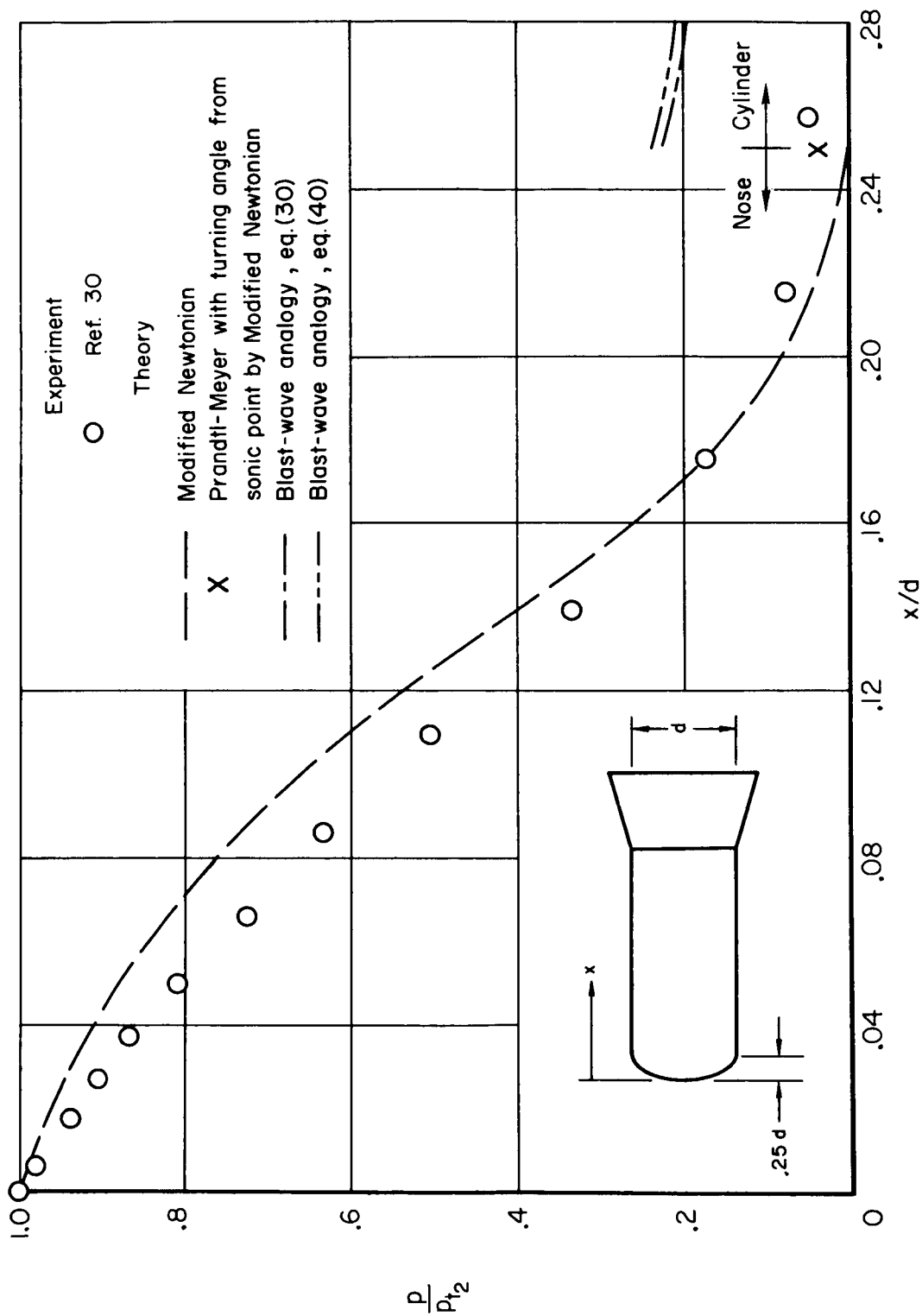


(b) Body alone.



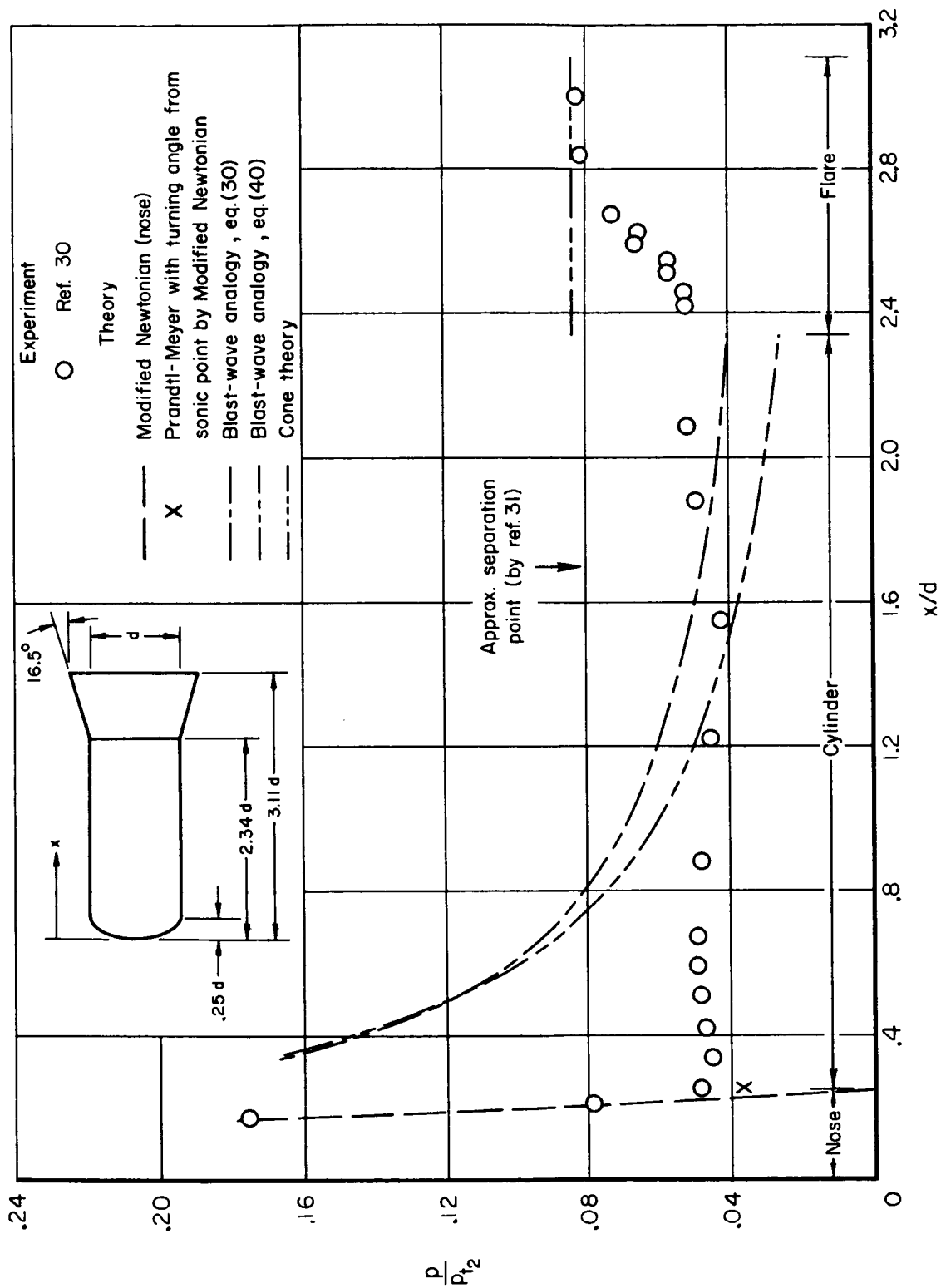
(a) Flare alone.

Figure 17.- Comparisons of calculated with experimental C_{Na} and C_{Ma} results for flare alone and body alone at $\alpha = 0^\circ$. (All C_{Ma} values are referenced to $l = 3.11 d$.)



(a) Pressure distributions over nose.

Figure 18.- Theoretical and experimental pressure distributions over Polaris configuration at $\alpha = 0^\circ$ and $M_\infty = 4.86$.



(b) Pressure distributions over cylinder and flare.

Figure 18.- Concluded.

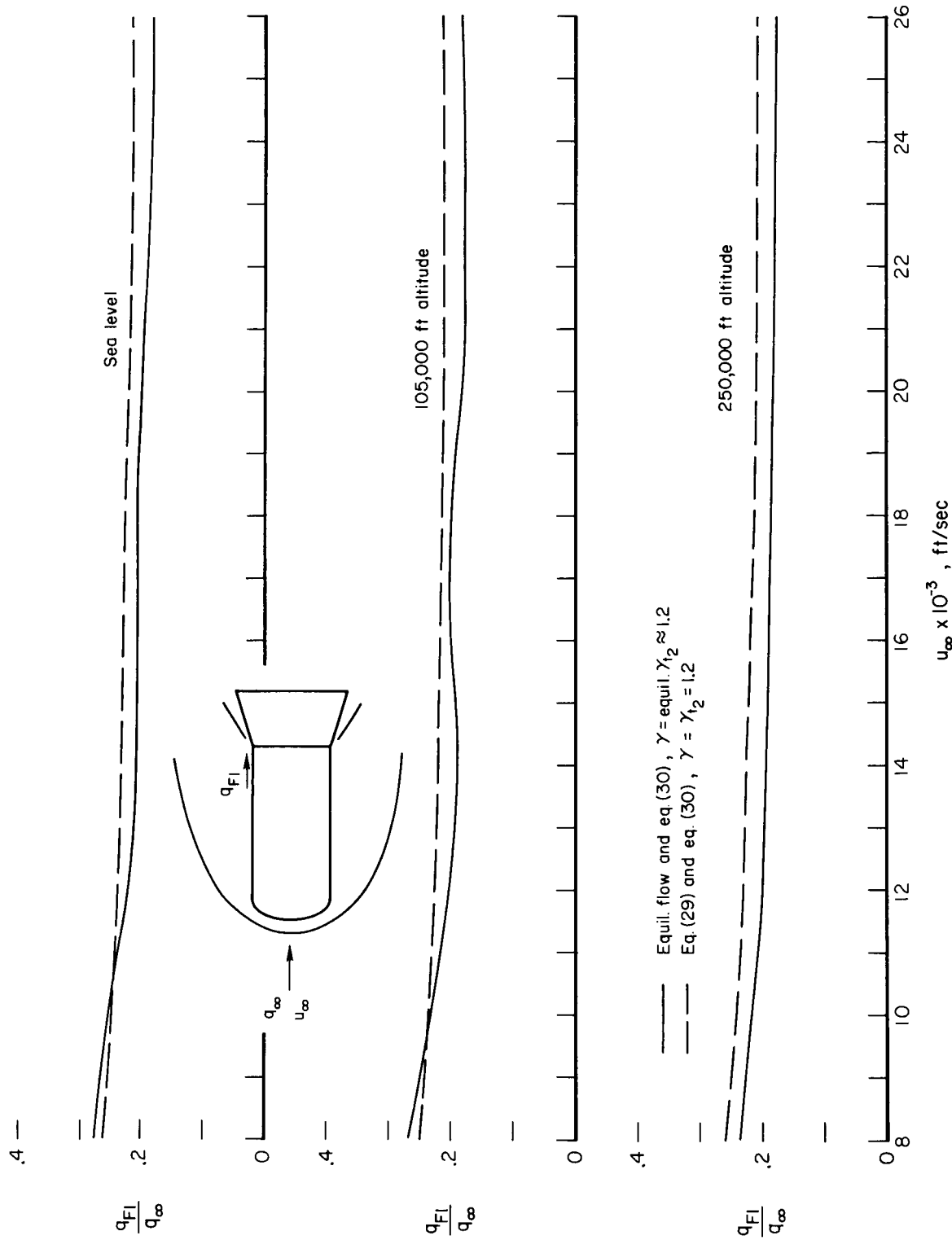


Figure 19.- Comparison of equation (29) with equilibrium flow method for determining dynamic pressure at flare of Polaris-type vehicle for high-speed flight.

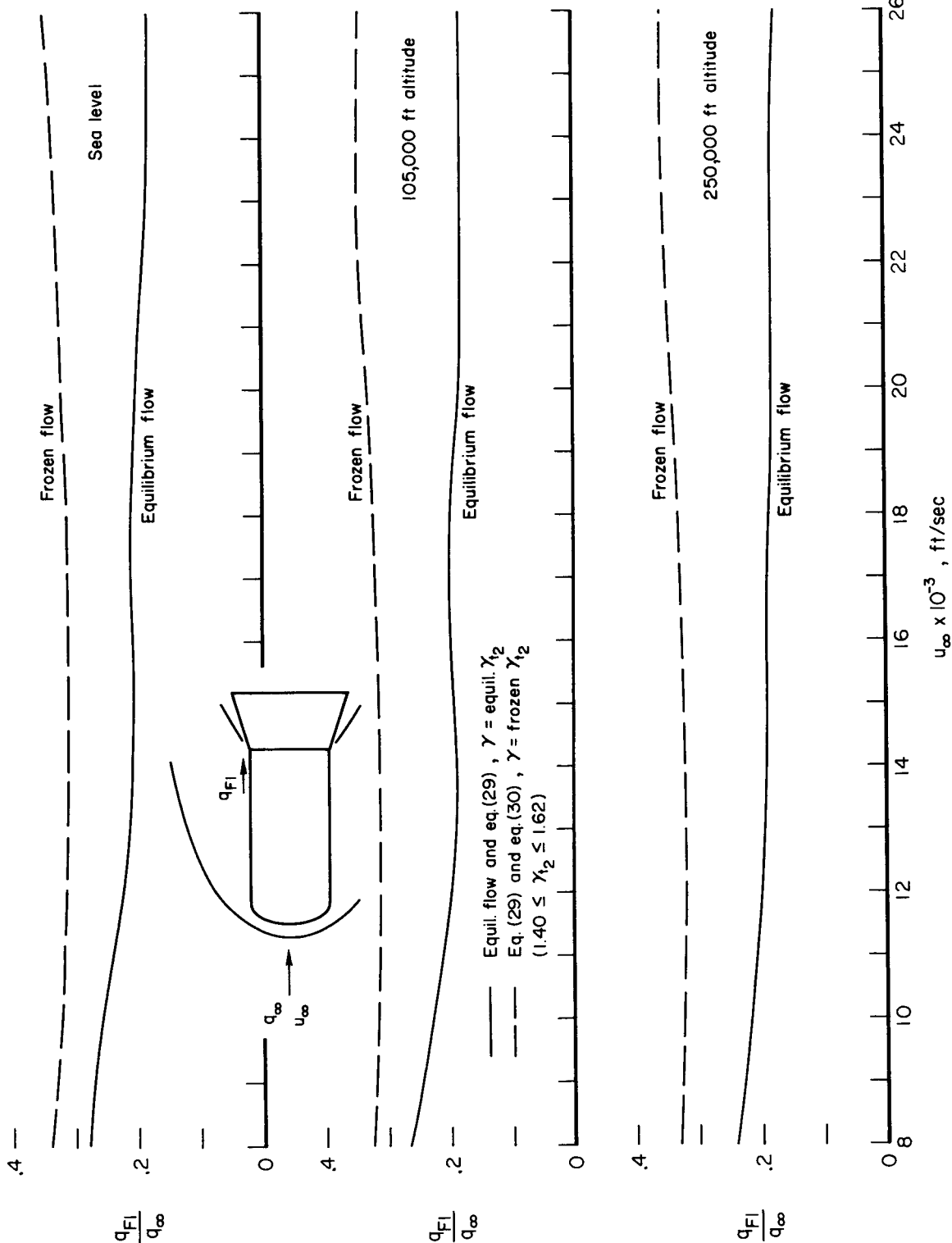


Figure 20.- Comparison of computed dynamic pressure at flare of Polaris-type vehicle for the cases of equilibrium flow and flow which is assumed frozen at the body stagnation condition.

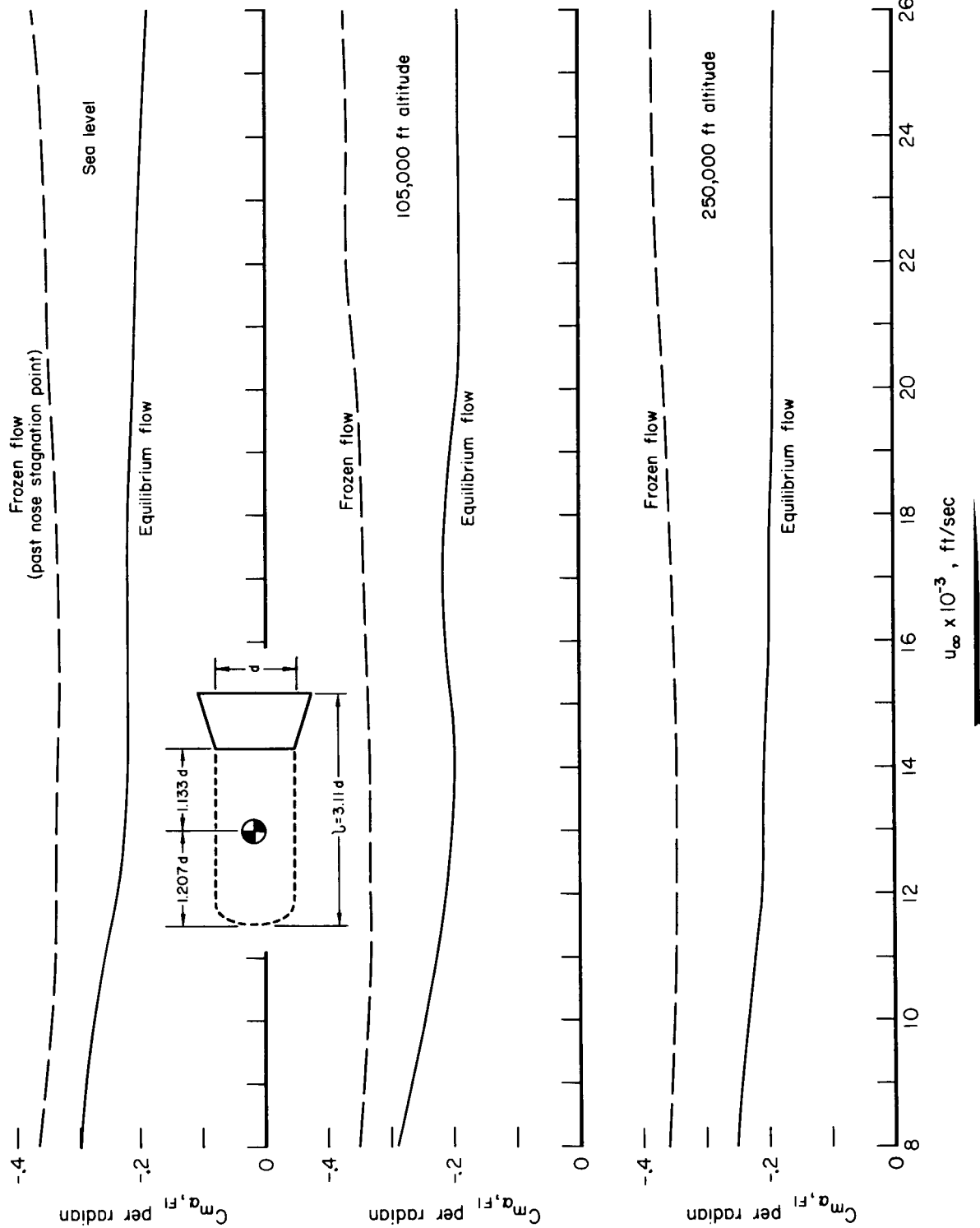


Figure 21.- Effect of flow state on the computed rare-stability contribution for a Polaris-type vehicle.